Title
MicroRNAs with Therapeutic Potential Regulate Ovarian Cancer Cell Physical Properties and Invasive Behavior

Author
Chan, Clara

Publication Date
2017

Peer reviewed|Thesis/dissertation

UNIVERSITY OF CALIFORNIA

Los Angeles

MicroRNAs with Therapeutic Potential Regulate Ovarian Cancer Cell Physical Properties and Invasive Behavior

A dissertation submitted in partial satisfaction of the
requirements for the degree of Doctor of Philosophy
in Biomedical Engineering

by

Clara Chan

2017

ABSTRACT OF THE DISSERTATION

MicroRNAs with Therapeutic Potential Regulate Ovarian Cancer Cell Physical Properties and Invasive Behavior

by

Clara Chan

Doctor of Philosophy in Biomedical Engineering

University of California, Los Angeles, 2017

Professor Amy Catherine Rowat, Chair

The activities of pathways that regulate malignant transformation can be influenced by microRNAs (miRs). Increased expression of tumor-suppressor miRs are associated with improved clinical outcomes in patients and reduced invasion of human cancer cell lines. In this thesis we investigate the mechanism underlying the reduced invasive potential of human ovarian cancer cells that are transfected with miR mimics representing five tumor-suppressor miRs (miR-508-3p, miR-508-5p, miR-509-3p, miR-509-5p, miR-130b-3p). Cells with elevated levels of tumor-suppressor miRs exhibit decreased invasion through collagen matrices, increased cell size, and reduced deformability as measured by microfiltration and microfluidic assays. To understand the molecular basis of altered invasion and deformability induced by these miRs, we use predicted and validated mRNA targets that encode structural and signaling proteins that regulate cell mechanical properties. Combined with image analysis of F-actin in single cells, our results suggest that these tumor-suppressor miRs may alter cell physical properties by regulating the

actin cytoskeleton. Our findings provide biophysical insights into how tumor-suppressor miRs can regulate the invasive potential of ovarian cancer cells, and identify potential therapeutic targets that may be implicated in ovarian cancer progression.

The dissertation of Clara Chan is approved.

Pei-Yu Chiou

Dino Di Carlo

Sanaz Memarzadeh

Amy Catherine Rowat, Committee Chair

University of California, Los Angeles

2017

Table of Contents

List of Figures

List of Tables

List of Acronyms

AFM = Atomic Force Microscopy

BSA = Bovine Serum Albumin

DRIE = Deep Reactive Ion Etching

ECM = Extracellular Matrix

EMT = Epithelial-to-Mesenchymal Transition

FBS = Fetal Bovine Serum

HGSC = High-Grade Serous Ovarian Cancer

IF = Intermediate Filament

MEMS = Microelectromechanical Systems

MiRNA = MicroRNA

MMP = Matrix Metalloproteinases

MPA = Micropipette Aspiration

MT = Microtubule

MTC = Magnetic Twisting Cytometry

PBS = Phosphate Buffered Saline

PCR = Polymerase Chain Reaction

PDMS = Polydimethylsiloxane

PECVD = Plasma-Enhanced Chemical Vapor Deposition

PEEK = Polyetheretherketone

PMF = Parallel Microfiltration

RBC = Red Blood Cell

SCR = Scrambled Negative Control

TFM = Traction Force Microscopy

UV = Ultraviolet

List of Supplementary Materials

Acknowledgements

This research has been financially supported by the National Science Foundation CAREER Award (DBI-1254185 to ACR), the NIH/National Center for Advancing Translational Science (NCATS) UCLA California Translational Science Institute (CTSI) Grant Number UL1TR000124, and the University of California Cancer Research Coordinating Committee.

A version of Chapter 2.1 has been published in Hoelzle DJ, Varghese BA, Chan CK, Rowat AC. (2014) A Microfluidic Technique to Probe Cell Deformability. *J. Vis. Exp.* **91**, e51474. (doi:10.3791/51474).

A version of Chapter 2.3 and Chapter 3.1- 3.3 and 3.5 has been published as Chan CK, Pan Y, Nyberg K, Marra MA, Lim E, Jones SJM, Maar D, Gibb EA, Gunaratne PH, Robertson AG, Rowat AC. (2016) Tumour-suppressor microRNAs regulate ovarian cancer cell physical properties and invasive behaviour. *Open Biology*. **6**: 160275 (doi: 10.1098/rsob.160275).

Biographical Sketch

University of California Los Angeles, Los Angeles, CA, USA 2011 - 2014
M.S., Biomedical Engineering

Simon Fraser University, Burnaby, BC, Canada 2005 - 2010
B.Sc., Physics (Biophysics Honors Program)

University of Western Australia, Perth, WA, Australia 2007
International Study Abroad Program

PUBLICATIONS

Chan CK, Pan Y, Nyberg K, Marra MA, Lim E, Jones SJM, Maar D, Gibb EA, Gunaratne PH, Robertson AG, Amy C Rowat. (2016) Tumour-suppressor microRNAs regulate ovarian cancer cell physical properties and invasive behavior. *Open Biology*. **6**: 160275.

Gunaratne PH, Rao AK, Hernandez-Herrera A, Pan Y, Rait AS, Benham AL, Rubab F, Venkatanarayan A, Robertson AG, Lim E, Marra MA, Jones SJM, Chan CK, Rowat AC, Coarfa C, Kim SS, Pirollo KF, Flores ER, Chang EH. (2016) Tumor-targeted delivery of microRNA-130b, a novel therapeutic strategy for circumventing mutations in p53 by inducing family member TAp63 (submitted).

Pan Y, Robertson AG, Pedersen L, Lim E, Hernandez-Herrera A, Rowat AC, Chan CK, Chu A, Wen Y, Zhang X, Patil SL, Basu-Roy U, Mansukhani A, Sipahimalani P, Bowlby R, Brooks D, Thiessen N, Ma Y, Moore RA, Schein JE, Mungall AJ, Pecot CV, Sood AK, Jones SJM, Marra MA, Gunaratne PH. (2016) miR-509-3p is clinically significant and strongly attenuates cellular migration and multi-cellular spheroids in ovarian cancer. *Oncotarget* **7**, 25930–25948.

Wieczorek A, Rezaei N, Chan CK, Xu C, Panwar P, Brömme D, Merschrod EF, Forde NR. (2015) Development and characterization of a eukaryotic expression system for human type II procollagen. *BMC Biotechnology* **15**, 112.

Hoelzle DJ, Chan CK, Scott M, Rowat AC (2015) A large displacement, high frequency, underwater MEMS actuator. *J. Applied Phys.* **117**, 014503.

Hoelzle DJ, Chan CK, Varghese BA, Rowat AC (2014) A microfluidic technique to probe cell deformability, *J. Vis. Expt*. **91**, e51474.

Qi D, Chan CK, Rowat AC (2012) Parallel fabrication of an array of holes in PDMS. *Lab on a Chip - Chips & Tips*.

Rezaei N, Downing BPB, Wieczorek A, Chan CK, Welch R.L., Forde NR. (2011) Using optical tweezers to study mechanical properties of collagen. *Proceedings of SPIE.* **8007**, 80070K.

1 Cancer Cell Physical Properties

1.1 Introduction

Cancer metastasis is the highly regulated process where primary tumor cells invade adjacent tissue, infiltrate the circulatory system and vasculature, and spread to a new secondary site [1]. The initiation of metastasis is accompanied by a loss of intercellular adhesion, degradation of the extracellular matrix (ECM), and conversion of tumor cells to a motile phenotype [2,3]. It is believed that a key developmental program activated during cancer invasion and metastasis is the epithelial-to-mesenchymal transition (EMT) in which cancer cells repress many of their epithelial-associated markers and upregulate mesenchymal-associated markers [4–6]. Changes in the biophysical properties of cancer cells, such as loss of adhesion and stiffness, are thought to be hallmarks of EMT [7]; loss of E-cadherin and cytokeratins result in altered physical and mechanical properties of cells [8]. The ability of metastatic tumor cells to mechanically soften and modify their adhesion to ECM is thought to enhance their capacity to escape the primary tumor and survive in the circulation. Understanding the physical forces that metastatic cells experience and overcome in their microenvironment, and the complex regulatory networks controlling EMT can provide insight into tumor progression and metastasis, and may improve our ability to target this key step in tumor progression.

1.2 Cell migration: A complex physiochemical process

Mechanical forces play a crucial role in regulation of cell shape [9] and generation of protrusive and contractile forces during cell spreading and motility [10,11]. One of the distinguishing features of metastatic cells is their ability to migrate through a variety of ECM tissues that have different architecture, pore sizes, and fiber crosslinking [12]. Crucial mediators of the tumor microenvironment include ECM remodeling proteinases, such as matrix metalloproteinases (MMPs) [2,13], whose proteolytic activity

alters cell–cell and cell–ECM interactions, and degrade physical barriers during invasion. Such changes in the mechanical and structural environment of the tumor have been shown to contribute to dissemination and enhanced migration of cancer cells. For example, cells migrating through loosely crosslinked collagen networks can adopt an amoeboid phenotype and generate actomyosin forces to squeeze through pores of the ECM network without the use of matrix metalloproteinases (MMPs) [14]. In dense three-dimensional (3D) matrix, cell invasion is believed to depend on the ability of cells to generate sufficient traction forces to overcome the steric hindrance of the surroundings. Together with the actin cytoskeleton, integrins facilitate cell–substrate adhesion, contractility, and traction force generation to pull the cell and nucleus through the matrix network [15]. Traction forces are concentrated at the periphery of the cell front; this is consistent with a propulsive role during cell migration [16,17]. Moreover, the magnitude of traction forces depend on specific aspects of cell geometry, such as distance from the cell center to the periphery [18] and the size of focal adhesions for spread cells [19]. This suggests an important function of traction forces in detecting and controlling cell shape. Indeed, a strong correlation between traction forces, cell polarization and orientation, and cell migration has been reported for tumor cells in a 3D matrix [20]. The directionality of force generation is believed to be important for cancer cell invasion by coordinating cell protrusion, attachment, and traction generation [21]. Consistent with this view, the strain energy and its density distribution are highly anisotropic in invasive cells, but nearly isotropic in non-invasive cells [20].

Although a less deformable cell and increased matrix stiffness can provide a barrier for cell movement through narrow pores, matrix stiffness can also alter cellular contractility to promote migration. Fibroblast cells migrate toward substrates of increasing stiffness, a response termed durotaxis [22]. Indeed, increasing traction force generation has been observed on substrates of increasing stiffness [23,24]. This suggests that substrate stiffness provides a feedback mechanism that modulates cytoskeletal organization and traction force generation responsible for cell migration. The sensitivity of cell migration to stiffness

gradients could have important implications for tumorigenesis, which is accompanied by increases in ECM stiffness.

1.3 Molecules that regulate cellular mechanical properties

Aberrant regulation of cell migration drives cancer invasion and metastasis [25–27]. The driving force for cell migration is the formation of membrane protrusions which requires spatial and temporal reorganization of the cell cytoskeleton. The cytoskeleton is a meshwork of entangled, transiently crosslinked biopolymers that provides a mechanical scaffold which stabilizes the cell and determines cell shape. Remodeling of cytoskeletal proteins lead to changes in cell contraction and the viscoelastic properties of cells [28]. The three major classes of cytoskeletal filaments are actin filaments (F-actin), intermediate filaments (IFs), and microtubules (MTs) [29]. Collectively, these proteins help maintain cell shape and structure, and are crucial to cell division, movement and intracellular transport.

Actin filaments

Actin filaments are comprised of two intertwined chains of globular actin monomers (G-actin). Bundles of actin filaments are held together by α-actinin and other actin-crosslinking proteins, such as fascin and filamin, which form actin stress fibers that attach to focal adhesion points and span throughout the cytoplasm [11,30]. Contraction is generated by a class of actin-associated motor proteins called myosins which use ATP hydrolysis to exert forces on actin filaments [31,32]. This process of contraction is complex because actin filaments are dynamically organized structures that undergo continuous assembly, disassembly, and overall reorganization. The spatial organization of actin filaments within the network, and their connectivity can impact the behavior of actomyosin contractility [33–35]. For example, it has been reported that high F-actin crosslink density impedes contractility [36], and branched networks are less contractile than bundles of anti-parallel filaments [37]. However, crosslinking proteins vary in their size and affinity, and can therefore have differential effects on the organization of actin networks [35]. A dense network of cortical actin is found underneath the plasma membrane and provides the framework

that supports the membrane and determines the shape of the cell. Traction forces may also be important for enabling adherent cells to maintain a spread shape. Supporting this idea, studies have shown that cells treated with a myosin II inhibitor such as blebbistatin take on highly irregular shapes [38].

Various techniques have been used to determine the contribution of actin to cell mechanical properties [39]. For some measurements looking at cortical actin, disruption with cytochalasin D leads to cell softening and to stronger frequency dependence as measured by magnetic twisting cytometry (MTC) [40] and atomic force microscopy (AFM) [41]. Myosin inhibitors show variable effects in the cortical region. For example, MTC measurements on epithelial cells treated with blebbistatin showed that the cortical response was independent of myosin motor activity [42]. However, smooth muscle cells showed treated with the myosin light-chain kinase inhibitor ML-7 showed a small decrease in rigidity compared with untreated cells [43].

Microtubules

In addition to F-actin, the cytoskeleton is also composed of a network of highly dynamic microtubule filaments that play an important role in mitosis and transport of intracellular organelles and vesicles [44]. Structurally, these filaments are hollow tubes consisting of two different protein subunits, alpha-tubulin and beta-tubulin, which associate end-to-end to form protofilaments. All alpha and beta-tubulin heterodimers are arranged in the same direction giving microtubules a polar structure. Due to the structural importance and high rigidity of microtubules, their mechanical properties have been extensively studied [45,46]. Observations of microtubule bending or buckling [47,48] and of microtubule thermal fluctuations have proven to be a reliable method to extract mechanical properties [45,49,50]. Microtubule disrupting agents such as colchicine increase contractile forces while microtubule stabilizing agents are observed to decrease contractile forces [51]. Individual microtubules are easily buckled under compressive loads [52,53], although their ability to support compression can be increased through

stabilizing agents [54]. This suggests that microtubules could play an important role in altering the deformation of cytoskeletal networks.

Intermediate filaments

A large family of proteins, collectively referred to as intermediate filaments (IFs), are another principal structural determinant within cells. Unlike F-actin and MTs, which are composed of highly conserved globular proteins, IFs can be formed from 40 different subunit proteins which are subdivided into five classes: keratins, neurofilaments, desmin, lamins, and vimentin. Each IF protein has a distinct chemical structure and function within the cell. For example, vimentin plays a key role in adhesion by regulating integrin functions and cell–cell contacts [55]. Lamins maintain nuclear shape and mechanical stability [56,57]. The mechanical properties of IF proteins are believed to be essential for the normal function of many tissues. Mutations in IFs can lead to diseases such as cardiomyopathies and skin-blistering disorders, which are characterized by a failure of tissues to withstand mechanical stress [58,59]. The unique mechanical properties of IFs have motivated recent studies to determine their role in the mechanical properties of cells. It is believed that IFs fulfill primarily structural functions and provide stability to the cell: *in vitro* IF networks undergo strain-stiffening and can withstand large deformations that would rupture F-actin or microtubules [60]. Understanding the physical principles that regulate the dynamics and the mechanical response of IF networks can provide new clues about the complex mechanical response of live cells.

1.4 Changes in cellular mechanical properties

Although the importance of understanding mechanical properties of biopolymer networks has been appreciated for some time, recent advances in biochemical and biophysical techniques now enable precise measurements of mechanical response of live cells over a range of length and time scales. A wide variety of tools have been adapted from the physical sciences to study the mechanical properties of cells and the responses that cells have to external forces. In general, these techniques fall into two classes: force-

application techniques or force-sensing techniques. Force-application techniques measure a cell's response to an applied deformation or force and have been used to determine the material properties of a cell, while force sensing techniques measure the forces produced by cells during development, contraction, migration, and other commonly occurring cell processes. Advances in technology have allowed for the development of a number of different specialized approaches. Here we discuss some of the most commonly used techniques.

Force application techniques

The classic method for studying cell deformability at the level of single cells is micropipette aspiration (MPA). During MPA, the viscoelastic properties of individual cells are determined by using a small negative pressure to induce deformation of the cell into a micropipette. The intrinsic mechanical properties of aspirated cells can be derived using various models based on the relationship between the suction pressure, the diameter of the pipette orifice, cell size, and the protrusion length of the cell in the pipette [61]. This technique has been used to characterize a wide variety of cell types, including endothelial cells [62], erythrocytes [63], and leukocytes [64], as well as to study the deformability of malaria parasite infected RBCs [65].

Another powerful technique to study the properties of single adhered cells is atomic force microscopy (AFM). In AFM, a flexible cantilever equipped with a sharp AFM tip is used to probe the cell surface. The tip deflection is monitored during scanning over the sample surface and can be used to measure interaction forces and generate a three-dimensional image of the surface. AFM can also be used to detect real-time cell mechanical properties, including the mechanical response of cells after exposure to shear stress [66], cell adhesion [67], and cell differentiation [68]. Advances in AFM have broadened its use as a force sensing technique to measure interfacial forces. This has made it possible to directly study intermolecular interactions, rupture forces, and the strength of single bonds [69,70].

Methods for studying single cells in suspension include optical tweezers and optical stretching techniques. In both techniques, a focused laser beam is used to generate forces without direct contact of the cell. For optical tweezers, a pair of dielectric microbeads may be attached to the cell by ligand or antibody binding and controlled by a laser beam that exerts a restoring force on the bead. Forces applied to the beads are up to a few hundred pN [71], which is sufficient to induce deformation of single cells. For an optical stretcher, instead of using beads attached to the cell surface, two diametrically opposed lasers are directed towards the cell to generate forces that deform single cells [72]. The force on the cell surface is proportional to the laser intensity. The technology of laser trapping can be combined with microfluidics to achieve high-throughput detection of cell mechanical properties. The optical stretch technique has been applied to study the deformability of red blood cells [73], differentiation of myeloid cells [74], oral cancer diagnosis [75], and for detecting changes during the progression of mouse fibroblasts and human breast epithelial cells from normal to cancerous state [76].

Microfluidic technologies are attractive for studying cells due to advantages of small sample volume, integration capability, biocompatibility, and higher throughput. Flowing cells through microchannels that have a cross sectional dimension smaller than the diameter of the cell is a common way to deform cells in microfluidic devices. To mimic the environment of human capillaries or narrow gaps encountered during cancer metastasis, structures such as tapered microchannels [77,78], funnel filters [79], and gap shape constrictions [80,81] have been used to probe cell deformability. The output measurement produced using these microfluidic device include parameters such as cell transit time through the constrictions [82,83], entry time for the cell to squeeze through the microchannel [78], the recovery time for the deformed cell to return to its original shape after leaving the constriction [84], and transit velocity [78].

Another way to deform cells using microfluidics involves hydrodynamic forces. The fluid flow through the microfluidic channels can provide a hydrodynamic force to probe cell deformability without any contact between the cells and the channel wall. The advantage of this approach is that is does not depend on cell-wall interactions. Cells can also be deformed using extensional flow created by converging

streamlines, the ratio of the length of the long axis of a deformed cell to a perpendicular shorter axis characterizes the deformation index (DI) and reflects cell deformability [85,86]. Using this technique, Gossett *et al.* showed that cell deformability could be used as an early biomarker for pluripotent stem cell differentiation.

The biophysical characteristics of cells are attractive potential label-free diagnostic markers for cancer and disease progression. Measureable changes in cellular architecture and nuclear structural changes are associated with early carcinogenesis: metastatic breast cancer cells are more deformable than the non-tumorigenic cells as measured by AFM [87]. Cellular deformability has also been applied to diagnose malignant pleural effusions where disseminated tumor cells can be difficult to identify by traditional cytology [88]. These studies lay the groundwork for clinical diagnoses of cancer using biophysical markers, which could help to improve clinical decision-making.

Whole cell deformability

The response of cells to mechanical stress is complex, depending on the experimental method, frequency, magnitude, and location of applied force [89,90]. A popular tool to study the mechanical response of whole cells and their subcellular components is AFM. By altering the geometry of the cantilever tip, both local and whole cell studies can be performed on living cells. For example, modified AFM probes with polystyrene microsphere tips have been used to better approximate the rheological properties of whole cells [91]. Such studies have shown that a cell's mechanical response is determined to a large extend by the underlying cytoskeleton, provided that the cell deformation is small and in the range of a few micrometers [92]. When sub-micrometer deformations are analyzed at the same magnitude of force, both AFM and optical laser trapping yield similar values for the Young's modulus of cells. At these low forces, the Young's modulus is largely determined by the actin cortex [93]. The nucleus does not appear to provide significant resistance or be a major contributor to cell shape recovery in response to local deformations [90]. By contrast, larger deformations are more sensitive to the mechanical properties of the

cell nucleus and the cell interior. For example, in a micropipette aspiration study, melanoma cells overexpressing lamin A showed reduced nuclear deformability and reduced cell invasion [94]. This is consistent with enhanced transit efficiency of cells with reduced levels of lamins A/C during passive perfusion through microfluidic channels smaller than the size of the nucleus [95]. Such studies of cell and nuclear deformation at large strains are critical to better understanding the role of whole cell deformability in cancer cell invasion and metastasis.

Force sensing techniques

In traction force microscopy (TFM), cells are seeded on a polymeric gel substrate of known elastic modulus that has been embedded with micron-sized beads [96]. These beads serve as fiducial markers so that traction forces can be estimated by tracking the displacement of the beads [97]. TFM has been used to determine traction forces during migration [16,96] and development [98], to measure forces at focal adhesions [99], and to elucidate the effect of cell shape [18,100]. A variation of this method uses arrays of vertical cantilevers to monitor the traction forces produced by cells. Here, the tips of the microposts, or micropillars, are coated with an extracellular matrix protein. Studies employing micropost arrays have found that the total contractile forces produced is proportional to the focal adhesion area and the amount of cell spreading [101]. In a study on MDCK epithelial cells, the maximum traction forces were concentrated at the edge of the cell, and the epithelial cells within monolayers created higher traction forces than individual cells alone [102].

2 Measuring Cell Deformability

While a significant amount of cancer research has focused on genetic and metabolic changes underlying malignant transformation, cancer cells also exhibit striking alterations in cell mechanical properties compared to benign cells. The mechanical differences observed in invasive cancer cells are thought to reflect underlying cytoskeletal or nuclear changes. Various anti-cancer drugs, including taxanes and cytochalasins, affect the integrity of the cytoskeleton [103,104], disrupt the cell cycle [105] and alter cell mechanics [106]. Single cell mechanical measurements could therefore be used to aid high-throughput approaches to personalized medicine by providing a label-free biomarker to screen potential new cancer treatments. To fully exploit single cell mechanical phenotyping, or mechanotyping, for improved patient outcome requires high-throughput studies to understand how a heterogeneous population of cells found in most tumors will respond to anti-cancer drugs. The majority of high-grade serous ovarian (HGSC) tumors develop chemoresistance to taxol and cisplatin drugs, resulting in poor patient outcome. If we could classify subpopulations of cells from patient tumor samples that are drug resistant, we could identify treatments to target the chemoresistant cells.

2.1 Deformability cytometry

To probe the physical behavior of individual cells, microfluidic devices present an ideal platform that can be customized to study a range of cell behaviors including their ability to migrate through narrow gaps [107] and to passively deform through micron-scale constrictions [78,107–110]. Polydimethylsiloxane (PDMS) microfluidic devices are optically transparent, enabling cell deformations to be visualized using light microscopy and analyzed using basic image processing tools. Moreover, arrays of constrictions can be precisely defined, enabling analysis of multiple cells simultaneously with a throughput that exceeds many existing techniques [61,111].

Here we present a detailed experimental protocol for probing cell deformability using the 'Cell Deformer' PDMS microfluidic device. The device is designed so that cells passage through sequential constrictions; this geometry is common in physiological contexts, such as the pulmonary capillary bed [112]. To gauge cell deformability, transit time provides a convenient metric that is easily measured as the time required for an individual cell to transit through a single constriction [78,109]. We use pressure-driven flow to maintain a constant pressure drop across the constricted channels during cell transit. Our protocol includes detailed instructions on device design and fabrication, device operation by pressure-driven flow, preparation and imaging of cells, as well as image processing to measure the time for cells to deform through a series of constrictions. As a representative sample of data, we show cell transit time through a series of constrictions as a function of the number of constrictions passaged. Analysis of the timescale for cells to transit though narrow constrictions of a microfluidic device can reveal differences in the deformability of a variety of cell types [78,79,113]. The device demonstrated here uniquely surveys cell transit through a series of micron-scale constrictions; this design emulates the tortuous path that cells experience in circulation and also enables probing additional physical characteristics of the cells such as relaxation time.

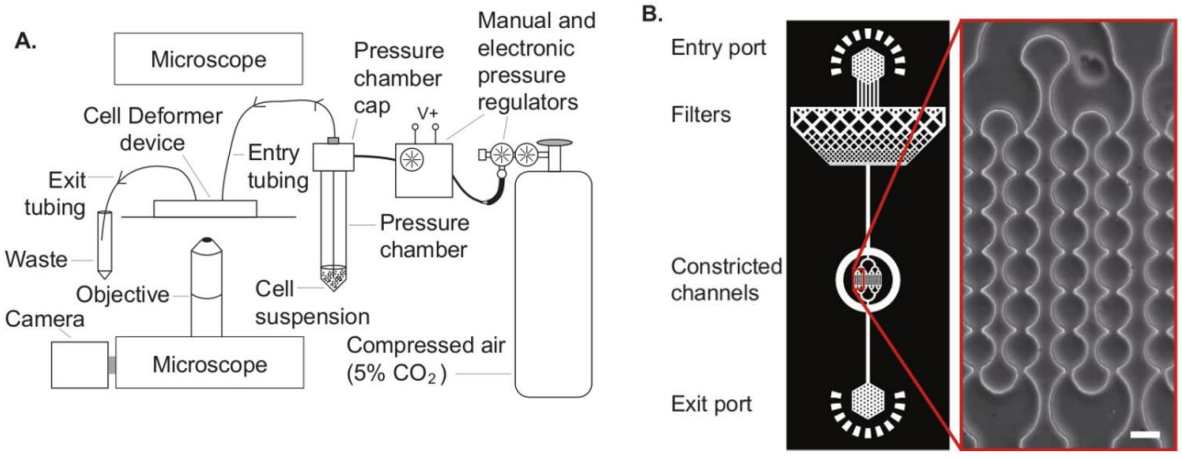

Figure 1. Schematic illustration of the microfluidic setup.

(a) ‘Cell Deformer’ device in the experimental setup showing the peripheral connections. (b) The device design has 4 functional regions: entry port, cell filter, constriction array, and exit port. Architecture of the microfluidic device showing its main features, inset shows a transmitted light image of the constricted channels. Scale, 10 µm.

The device design has four basic functional regions: entry port, cell filter, constriction array, and exit port (Figure 1). The overall design can be applied to a wide array of cell types, with minor adjustments to dimensions. Provided here are a few basic design recommendations along with device parameters that are effective for a selection of both primary and immortalized cells.

1. Select the width of constriction array channels (Figure 1) to be approximately 30-50% of the average cell diameter; this constriction-to-cell size ratio results in significant cell deformation but minimal clogging. Given a cell type that has not previously been tested, it is prudent to design a range of constriction widths from ~30-50% the cell diameter to find the optimum width. As with many types of microfluidic devices, over 120 device master molds can be patterned on a single 4 inch silicon wafer, enabling an array of different device designs to be fabricated in a single fabrication process.
2. Select the channel height to be at least 50% of the cell diameter; this ensures the cell is confined in 2 dimensions. To prevent channel collapse during bonding, ensure that the channel aspect ratio is no less than 1:10 (height:width) throughout the device. For channels that must exceed this aspect ratio, add support posts to prevent collapse. Space support posts at a distance that is at least twice the cell diameter as to not impede cell flow.
3. Include a filter at the entry ports to remove debris and disaggregate cell clusters (Figure 1). Adjust the size and spacing of the filter posts so that the distance separating the posts is approximately equal to one cell diameter.

Supplies and preparation

A schematic of the entire setup is given in Figure 1. Before commencing any experiment, the following items must be prepared.

1. Fabricate the device master using standard techniques for lithographic micromachining [114,115]. Verify the height of the patterned features using a profilometer.
2. Prepare the air source for pressure-driven flow, using a tank of compressed air and sequence of air regulators and fittings (Figure 1).
    a. Set up an air supply tank and manual regulator. A composition of 5% CO_2 in air maintains a similar environment as a typical cell culture incubator, but other gas mixtures can also be used.
    b. Set up an electronically controlled pressure regulator in-line with the manual regulator. Use an electro-pneumatic converter to regulate and maintain a stable pressure drop across the channels, with pressure fluctuations of less than 2 kPa.
    c. Set up a pressurized chamber to drive flow of the cell suspension. Assemble a cell suspension chamber out of a standard flow cytometer tube and a machined cap that creates a pressure-tight seal on the tube.
3. Set up an inverted microscope fitted with a camera that has an acquisition rate of at least 100 frames per second to capture images of the cells flowing through the constriction array. Interface the camera with a video capture card and a computer.
4. Prepare a stock surfactant solution of 10% w/w Pluronic F-127 in phosphate buffered saline (PBS) as adding a small amount of F127 to the cell media solution will help to minimize cell adhesion to the PDMS walls. To prepare the F127 solution, vortex and heat gently at 37 °C to dissolve the F127. Prior to use, pass the solution through a 0.2 µm syringe filter and store at room temperature. Prepare the surfactant solution in advance as vortexing and filtering will generate bubbles that will persist for more than 24 hr.

Microfluidic device fabrication

1. Fabricate PDMS block with microfluidic channels.
    a. Mix PDMS thoroughly at a ratio of 1:10 (w/w) curing agent to base.
    b. Pour the mixture over the device master. Degas in a bell jar with applied vacuum until the entrapped bubbles disappear, or for about 10-20 min.
    c. Bake the degassed device at 65 °C for 4 hr. To prevent channels from collapsing, bake the device overnight to further crosslink the PDMS for a device with a higher elastic modulus that is more resistant to channel collapse. However, note that extended baking also embrittles the PDMS and may lead to cracking when punching holes.
2. Remove microfluidic devices from the master mold. Cut individual microfluidic devices out of the PDMS block with a razor blade and remove the device from the master. Start by gently lifting off one corner of the device; slow and gentle peeling, as opposed to lifting the PDMS block straight up, reduces the stress on both the PDMS and the master.
3. Punch holes in the PDMS device to create connection ports for access between tubing and microchannels. Create holes using a biopsy punch, and punch from the channel side through to the exterior side of the device. A biopsy punch with a 0.75 mm bore size creates holes that interface perfectly with polyetheretherketone (PEEK) tubing (outer diameter = 1/32” or 0.79 mm) or polyethylene tubing (PE-20, outer diameter = 0.043” or 1.09 mm).
4. Rinse the PDMS device with isopropanol (HPLC grade) to remove dust and lodged chunks of PDMS. Make sure the punched holes are clear of debris by directing a steady stream of pure isopropanol from a squeeze bottle through the holes. Blow dry with filtered air. After cleaning, place PDMS blocks with channels face up in a clean Petri dish to maintain device cleanliness. If required, store devices in this form until bonding.

5. Clean the glass substrate by rinsing with methanol (HPLC grade), blow dry with filtered air, and place on a 200 °C hotplate for 5-10 min to ensure the glass is completely clean and dry before plasma treatment.
6. Bond the PDMS device to the glass substrate.
    a. Oxygen plasma treat the channel side of the PDMS block and 1 side of a glass slide.
    b. Place the channel side of the PDMS on top of the treated side of the glass immediately after treatment.
    c. Hold together with light pressure for ~10 sec to promote bonding. Bake the entire device at an elevated temperature (60-80 °C) for at least 15 min to improve bond strength.

Deforming cells through constricted channels

1. Inspect the microfluidic device under a microscope. Ensure that the channels are not collapsed or broken and that both inlet and outlet holes connect directly into the device channels by using a low-power objective (10X). Designate defective devices by scoring the surface of the PDMS with a razor blade and do not use them for experiments.
2. Prepare the cell culture samples to be assayed. Culture cells using standard conditions.
    a. For example, culture HEYA8 cells in RPMI-1640 medium supplemented with 1% penicillin-streptomycin solution and 10% fetal bovine serum in 5% CO_2 incubator at 37 °C.
    b. For adherent cells, harvest them by trypsinization and resuspend in fresh growth medium. Use a standard trypsinization protocol; for example, add ~0.5 ml trypsin to a flask with 25 cm^2 culture area, and resuspend in ~30 ml fresh medium.
    c. Centrifuge the cells at 300 x g for 3 min, carefully aspirate the supernatant and resuspend cells to the appropriate final density in fresh culture medium with 0.1% v/v F-127.
3. Count the cells using a Coulter counter, hemacytometer, or flow cytometer. Adjust the cell suspension to a density of 1 x 10^6 to 5 x 10^6 cells/ ml. Once the suspension density is set,

supplement with approximately 0.1% v/v F-127. NOTE: The cell density and surfactant concentration may need to be modified depending on the particular cell systems; Table 1 provides a record of previously used concentrations of cells and F-127 for different cell types.

4. Place cell suspension in a flow cytometer tube and connect to the pressure cap. Before connecting the tubing to the microfluidic device, adjust the pressure to about 14-21 kPa and flush until the cell suspension emerges from the tip of the tubing. This will help to minimize air bubbles in the tubing and device.
5. Insert the tip of the tubing containing the cell suspension into the device inlet. If the device is bonded to a coverslip, place the device on a flat, solid surface such as the microscope stage before connecting the tubing; the coverslip is fragile and may otherwise break.
6. Insert a piece of tubing into the exit port and route it into an empty tube for waste collection such as an empty Falcon tube taped to the side of the microscope stage. For consistency in the overall fluidic resistance of the device between experiments, ensure that the inlet and outlet tubing is of the same diameter and approximately the same length for each experiment.
7. Gently ramp up the pressure to about 28 kPa or until cells flow through the channels. Position the device so that multiple channels are in the field of view and are perpendicular to the bottom of the screen. If the camera is limited by data size, acquire multiple videos to generate a sufficient number of independent data points. Adjust the frame rate as necessary for the desired data output. To capture changes in cell shape, use high speed imaging at 300 frames per sec (fps); to measure transit times of cells, use frame rates of approximately 100 fps.

Cell Type	Channel Height (μm)	Channel constriction (μm)	Mean Cell Diameter (μm)	Cell Concentration (cells/ml)	Surfactant Concentration (vol%)
HL-60	10.2	5, 7, 9	14	~1 x 10^6	F127: 0.1
Neutrophil-type HL-60	10.2	5, 7, 9	14	~1 x 10^6	F127: 0.1
OVCAR8	10.2	7, 9	16	~5 x 10^6	F127: 0.1
HEYA8	10.2	7, 9	17	~5 x 10^6	F127: 0.1
Mouse lymphocyte	5.5	3, 5	8	~3 x 10^6	F127: 0.33

Table 1. Previously studied cell systems and their operating conditions.

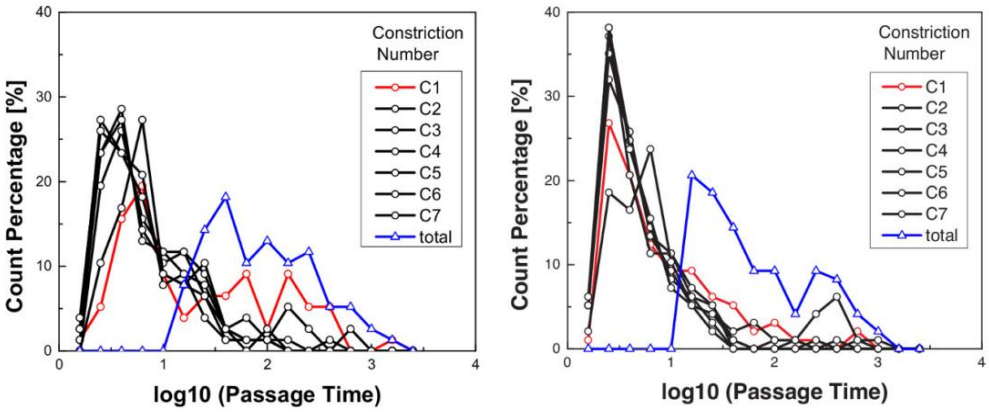

Figure 2. Representative transit time measurements as a function of constriction number.

(Left) HL-60 cells exhibit a longer transit time through the first constriction than (Right) ATRA-treated HL-60 (neutrophil-type) cells. A comparison of the transformed passage time (log10) through the first constriction as evaluated using the nonparametric Mann-Whitney test reveals the difference is significant, p = 1.47E-5. Cells typically transit through the first constriction more slowly than the subsequent constrictions. Data is shown here for cells transiting through 7 μm-wide constrictions at a driving pressure of 28 kPa. HL-60, N = 77, ATRA-treated HL-60, N = 97. Results were replicated in independent experiments over the course of 3 different days.

2.2 Development of a MEMS device for determining cell mechanical properties

Introduction

While microfluidic-based methods exploit fluid flow in microchannels to achieve higher throughput, these methods rely on optical detection to assess the relative deformability of cells. For example, optical stretchers are capable of deforming 10^3-10^4 cells in < 20 min [73], and inertial microfluidic devices operate at ~10^3 cells per second [86]. However, such techniques require intensive image processing, which inhibits the ability to rapidly characterize and sort single cells. By contrast, electronic-based detection methods can be easily scaled up and parallelized, which is a major advance over current technologies measuring cell stiffness.

Microelectromechanical systems (MEMS) based sensors and actuators provide excellent tools for manipulating and studying biological materials, cells, and tissues [116–118]. The density of individual cells can be measured very precisely using cantilever resonators with embedded channels [119]. Similarly, mechanical properties of cells can be measured by using a piezoelectrically actuated MEMS probe for indentation [116], or by adhering them to a MEMS platform and then stretching the cell [120]. Such devices are generally fabricated from single crystal silicon, but other materials can be used to take advantage of their distinct electrical, thermal, mechanical, optical, and piezoelectric properties. MEMS devices are typically capable of high speed actuation, due to their low mass and construction from stiff materials: a silicon-based physical actuator can attain up to ~10^{-6} m displacements at 1 kHz [121,122].

While MEMS devices enable rapid sensing and actuation, exploiting these advantages for studies of biological specimens is limited by the speed at which cells or molecules can be positioned for probing or measurement. For example, cells can be deposited onto a MEMS device for measuring their mass or adhesive forces, or the cells can be located and the device can be moved to their location for indentation.

We recently invented a capacitance-based probing and detection platform for rapid electronic measurement of cells under flow; this would enable real-time analysis and the ability to sort large numbers of single cells based on cell stiffness.

There are various strategies to manufacture microfluidic circuits for manipulation of conveyed particles or fluid streams. One approach is based on plasma polymerization of the encapsulating material on a photopatterned resist [123]. While this method requires no additional etching or bonding and may be processed onto different materials substrates without an adhesion layer, it does require additional fabrication steps to produce a photopatterned sacrificial layer. Alternatively, channels can be etched into a separate substrate, such as glass, which is then aligned and bonded to form a closed network [124]. This method requires that both device and channel pieces are very flat for bonding or requires an intermediate layer to compensate for the uneven surface [125].

Another method to deliver samples to MEMS devices is to enclose them in polydimethylsiloxane (PDMS) microchannels that have been patterned using soft lithography. This approach simultaneously leverages the strengths of soft lithography and MEMS devices. For example, zero dead-volume valves [126] and three-dimensional channels [127] can easily be made using soft lithographic processes that would be difficult or impossible using MEMS processes and materials. The process of designing and molding PDMS channels allows for rapid fabrication and prototyping. PDMS channels can also be fabricated with minimal equipment, and can be bonded to both glass and silicon reliably without an intermediate layer [128,129]. Other advantages of PDMS for biological applications include its optical transparency [130], chemical stability [131], permeability to gasses [132], and tunable mechanical [133] and surface properties [134].

While MEMS structures can be enclosed within PDMS, alignment tolerances have been large. For example, 300 μm silicon cantilever beams are incorporated into 600 μm PDMS channels to detect biomolecules in fluid flows [135]. MEMS pressure sensors are integrated into a ~3000 μm wide channel

to measure the pressure drop across a constriction. Similar PDMS-MEMS unions could be advantageous for a variety of sensors, including mechanical, optical, and thermal sensors. Additionally, actuators could be used to manipulate flow or objects. If we could integrate sophisticated microchannel geometries with high speed sensors and actuators, we could efficiently deliver biological samples for high-throughput measurements. Hybrid MEMS-PDMS devices are positioned to take advantage of the high speed and electronic control of MEMS devices while simultaneously leveraging the lower cost, simplicity, and ability to manufacture valves from soft lithography.

Device design

Here we describe a comprehensive protocol for fabricating a PDMS-MEMS hybrid electrostatic actuator that can attain micron-scale displacements at frequencies in the range of kilohertz. Our device design uses microfluidic channels fabricated from PDMS to direct fluid streams to a MEMS fabricated probe for mechanical measurements of cells by indentation. The oscillator and sensor probes are connected to parallel arrays of comb drives and are positioned on opposing sides of a microfluidic channel.

The complete oscillator, sensor, and cell system can be modeled by assuming that the oscillator and sensor act as a mass, spring, and damper system. Here we have also assumed that the cell response depends on contact velocity using the kelvin-voigt model (Figure 3). The effective spring constant of the oscillator and sensor is a function of the geometry of the beam structures and Young's modulus of silicon (E):

$$k = \frac{4Ehw^3}{{L_1}^3 + {L_2}^3}$$

where E = 130 GPa along the <1 0 0> crystalline plane in silicon [136] and spring height (h), width (w), and segment lengths (L_1 and L_2), are given in the Figure 4.

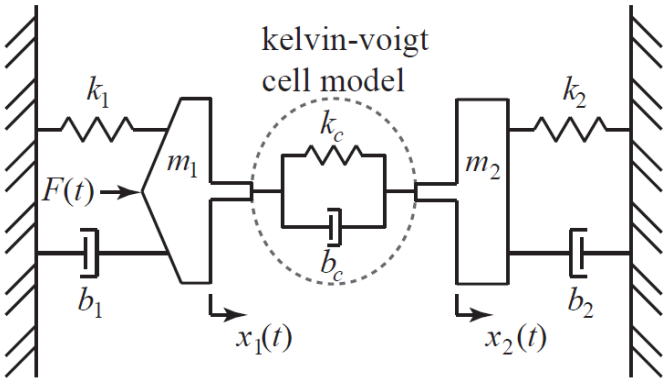

Figure 3. Simplified model of MEMS oscillator and sensor.

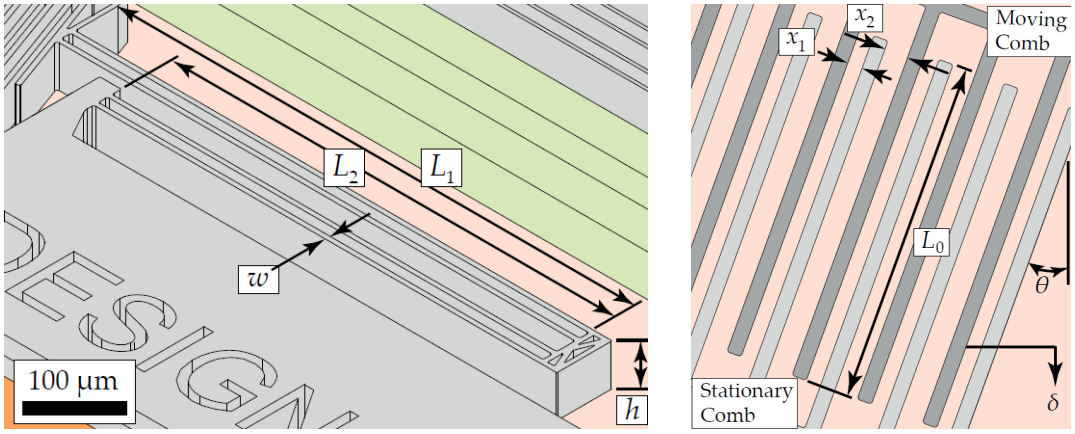

Figure 4. Geometry of the beam spring system (left) oscillator comb drive (right).

Comb drive actuators consist of interdigitated finger structures, where one comb is fixed and the other is connected to a compliant suspension. Deflection of these movable comb structures is driven by applying a voltage potential across the comb pair to generate an attractive electrostatic force; displacement is sensed by measuring a change in capacitance. The capacitance (C) is a function of displacement (δ), where N is

the number of comb pairs, x is the perpendicular distance of the gap spacing, κ is the dielectric constant of the medium, and ϵ is the permittivity of free space.

$$C(\delta) = \frac{N\kappa\epsilon h\delta}{x}$$

The electrostatic force (F) increases with decreasing gap spacing and an increasing number of comb fingers. The force as a function of the applied voltage (V) and displacement is described by:

$$F_{parallel}(x, V) = \frac{N\kappa\epsilon h V^2}{x}$$

$$F_{perpendicular}(x, V) = \frac{1}{2} N\kappa\epsilon A \left[\frac{(x_1+x_2)(x_2-x_1+2x)}{(x_1-x)^2(x_2+x)^2}\right] V^2$$

where A is the overlapping comb area.

The total force in the δ direction is given by:

$$F_\delta(\theta) = F_{parallel}\cos\theta + F_{perpendicular}\sin\theta$$

$$F_\delta(V) = \left(\left(\frac{1}{x_1 - \delta\sin\theta} + \frac{1}{x_2 + \delta\sin\theta}\right)\cos\theta + \frac{1}{2}\frac{(L_0 + \delta\cos\theta)(x_1+x_2)(x_2 - x_1 + 2\delta\sin\theta}{(x_1 - \delta\sin\theta)^2(x_2+\delta\sin\theta)^2}\sin\theta\right) N\kappa\epsilon h V^2$$

where θ is the array angle and L_0 is the neutral position comb overlap distance.

Device fabrication

We design our fabrication process so that our hybrid MEMS-microfluidic device will be optically transparent for visual observation of device performance (Figure 5). We thus fabricate our MEMS device on glass; the PDMS microfluidic device is thereafter aligned and bonded to the MEMS-glass substrate. Devices are fabricated from a Pyrex 7740 borosilicate glass wafer of thickness 500 μm, and a low

resistance (0.005-0.030 Ω-cm p-type silicon wafer of <1 0 0> orientation that has been thinned after anodic bonding until the silicon thickness is 50 μm (Plan Optik). To define the electrical contact layer, 8.5 nm of chromium and 392 nm of gold are deposited on the silicon side by electron beam evaporation (CHA Solution Electron Beam Evaporation System). Onto this substrate, we spin-coat a 1.2 μm-thick layer of SPR 700-1.2 photoresist (Megaposit Shipley); patterning is achieved by UV exposure using a Karl Suss MA6 optical aligner. The metal layers are selectively etched in gold etchant (Gold Etchant TFA) for 3 minutes and in chrome etchant (CR-7S, Cyantek) for 45 seconds. Next, 1.2 μm of SiO_2 is deposited by plasma-enhanced chemical vapor deposition (PECVD) (Georgia Institute for Electronics and Nanotechnology) for use as a hard mask during deep reactive ion etching (DRIE). A 1.2 μm of SPR 700-1.2 photoresist is spin coated over the oxide mask and patterned by contact photolithography. We use conventional reactive ion etching (RIE) performed in an Oxford 80 RIE to etch the SiO_2 hard mask (Figure 6). Individual dies are separated by wafer dicing and mounted to carrier wafers using Crystalbond 509 (Electron Microscopy Sciences). Finally, the silicon layer is etched to the underlying glass substrate by DRIE in a Unaxis Versaline Fast DRIE. After etching, the devices are removed from the carrier wafer with acetone, and the devices are released using 49% hydrofluoric acid (KMG Chemicals), which also removes any remaining SiO_2 hard mask. After release, the device is rinsed in water and in methanol, and then dried using a critical point drier (Tousimis 915B).

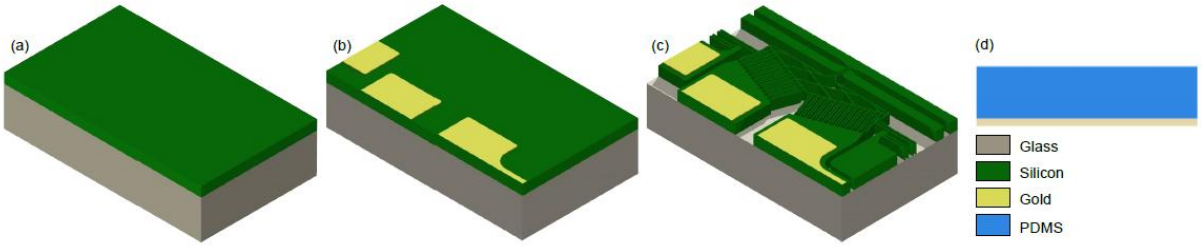

Figure 5. Schematic overview of MEMS fabrication procedure.

(a) A <1 0 0> silicon wafer is bonded to a glass wafer and polished to 50μm, (b) Cr/Au electrical contacts are deposited, (c) DRIE is used to etch the device, followed by an HF bath to release the hanging structures. (d) A PDMS cap is aligned and bonded to the glass to encapsulate the MEMS device in the microfluidic channels.

To fabricate the master mold for the PDMS device channels, we spin coat SU-8 photoresist (Microchem Corp) onto a silicon wafer per the manufacturer's instructions. To accommodate the features of our MEMS device, we fabricate a two level SU-8 master. The first layer of SU-8 2050, thickness ~50 μm, forms the bulk of the channels, with additional clearance around the oscillating portions of the device provided by an additional ~10 μm thick layer of SU-8 2010. Channel heights are confirmed using a profilometer. Prior to molding with PDMS, the master is run on a descum cycle in the plasma asher (Matrix 105 Downstream Asher) in order to remove small amounts of residual photoresist. To mold the PDMS device, we use Sylgard 184 (DOW corning) mixed with crosslinker at a 10:1 ratio and poured over the master. After degassing under vacuum, the PDMS is baked for two hours at 65°C. After baking, the PDMS is carefully peeled from the master. Channel inlets and outlets are excised using a biopsy punch (Harris Uni-core). For channels that serve as electrical vias, we use a 1.5 mm punch, for fluidic channels, we use a 0.75 mm punch, which interfaces with standard PE-20 tubing.

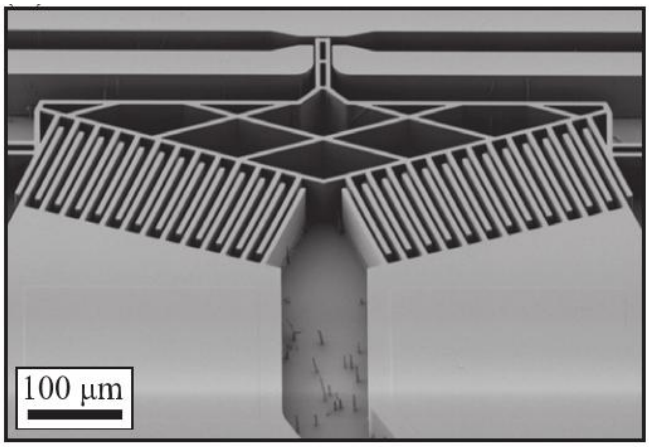

Figure 6. Scanning electron micrograph of the MEMS actuator fabricated by micromachining low-resistivity silicon bonded to glass.

To activate surfaces for bonding, we place the MEMS device and PDMS cap in a UV-ozone cleaner (Jelight Model 42) for 5 minutes. Immediately thereafter, we quickly align both surfaces using a custom-made alignment jig (Figure 7), and place the hybrid device into an oven for 30 minutes at 80°C. We dip copper wires in molten 52In48Sn to coat the ends, and place them into the holes punched for electrical vias after the device is placed on a hot plate at 150°C. After removing the device from the hot plate, UV-curable epoxy (Loctite 352) is used to secure the wires in place.

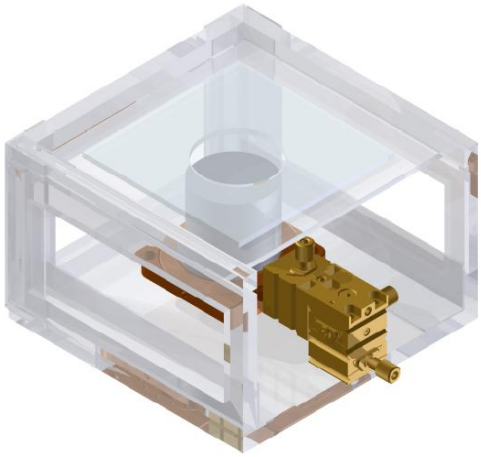

Figure 7. Setup to align the PDMS channels to the MEMS portion of the device.

The MEMS device is placed on the micromanipulator, and the PDMS is reversibly adhered to a glass plate (not shown), which is inverted through the hole in the top plate. After alignment is performed and contact is made, the glass plate is lifted and the device is baked.

Challenges associated with assembling the MEMS device

The presence of a MEMS device on the glass substrate complicated the bonding of the PDMS cap. Attempts with using corona discharge to bond PDMS to glass [128] damaged the silicon features, making the device useless. Different recipes were tried on an RIE machine (Oxford Plasmalab 80+ RIE system), in which the device is pumped down in vacuum and plasma treated with Oxygen plasma. Bonding with the RIE system was poor; we speculate this could be due to charging effects from the large exposed gold pads on insulating substrate. We found that a UV-ozone cleaning system (Jelight Model 42) provided good bonding without damaging the silicon structures or requiring a vacuum. Though we are usually able to align and bond the devices in about five minutes, we find that the bonding is strong even when alignment takes upwards of ten minutes after UV-ozone treatment [129].

Another challenge was the alignment of the PDMS channels and the MEMS device during bonding, especially since it needs to be carried out within a few minutes of treatment for bonding to occur. Since

the tolerances are tight, on the order of 10 μm, and do not allow for alignment by hand, we fabricated an alignment jig to facilitate rapid alignment after bonding treatment. This jig features a micromanipulator (Newport RSP-1T and M-MT-AB2) that allows for alignment in all three axis and rotationally. Alignment is carried out under a stereo microscope. After bonding, the PDMS cap is placed channel-side-up on a glass plate and reversibly adheres, while the MEMS device is placed on the micromanipulator. The pieces are aligned and brought into contact, then the glass plate is lifted and the device is baked. We verified the bonding strength by punching only a single fluidic via in the PDMS cap and bonding it to a glass slide or silicon wafer, then pressurizing the device. We were unable to delaminate the device, even when the pressure reached 13 psi, the highest our setup can supply.

2.3 Materials and methods

Cell culture and transfection

Ovarian cancer cells (HEYA8, OVCAR8) are cultured in RPMI 1640 medium supplemented with 10% heat-inactivated fetal bovine serum (FBS) and 1% of penicillin/streptomycin. Cells are grown under standard conditions at 37°C and 5% CO_2. MiR mimics and scrambled (SCR) negative controls are transiently transfected at 24 nM using Lipofectamine 2000 in serum-free OptiMEM medium, followed by the addition of 10% FBS after 4 hours in serum-free conditions. All assays are performed 72 hours post transfection.

Scratch wound invasion assay

To measure cell invasive potential, cells are seeded on 30 μg/mL collagen-coated 96-well microplates at a density of 27,000 cells per well. After overnight culture at 37°C with 5% CO_2, scratch wounds are generated on the confluent cell monolayer using sterile P1000 pipette tips and washed with PBS to remove debris and to prevent dislodged cells from settling and reattaching. We prepare collagen gels on ice immediately prior to use by diluting collagen type I (rat tail collagen I, Corning) in RPMI 1640

medium with 50 μM of the MMP-inhibitor, GM6001 (Santa Cruz Biotechnology), to a final concentration of 1 mg/mL collagen, 0.1 M NaOH is added to bring the pH to 7.4. Thereafter, 50 μL of collagen solution is added to each well and incubated at 37°C for 1 hour, followed by the addition of 200 μL of culture medium with 50 μM GM6001. To confirm reduced MMP activity, we measure total protease activity using 25 μL of 20 μM fluorogenic peptide substrate in 75 μL of conditioned media after 72 hours of cell culture (ES010, R&D Systems), followed by a 30 min incubation. Levels of fluorescence associated with hydrolysis of quenched fluorogenic peptide substrates are measured at 320 nm excitation and 405 nm emission. Images of the scratch wounded cells are acquired every 2 hours using an ORCA-R2 Digital CCD camera (C10600, Hamamatsu) mounted on an automated Zeiss Axio Imager Z1 microscope equipped with a 5x objective (N-Achroplan 5x/0.13, Zeiss) and temperature controlled environmental chamber set to 37°C. We analyze images using ImageJ software to determine the percentage of wound closure, or relative invasion, where *w(t)* is the area covered by cells at time *t*,

$$\%\ Relative\ Invasion = 100 \cdot \frac{w(t) - w(0)}{Total\ Image\ Area - w(0)}.$$

Scanning electron microscopy imaging

Collagen gels are fixed in 2.5% glutaraldehyde solution (0.1 M sodium phosphate buffer, pH 7.2) for 2 hours at room temperature, followed by post-fixation in 1% osmium tetroxide (0.1 M sodium phosphate buffer, pH 7.2) for 1 h at room temperature. Samples are then dehydrated using a graded ethanol series (30%, 60%, 80%, 100% ethanol, for 10 min each), critical-point dried (Tousimis), sputter-coated with 1–2 nm of gold (Denton), and imaged by scanning electron microscopy (JEOL).

mRNA/miR isolation and quantitative polymerase chain reaction

Relative gene expression levels are measured using the Applied Biosystems 7300 Real-Time PCR System. Briefly, total RNA is extracted from cells using the miRNeasy Mini Kit (Qiagen) following the manufacturer's protocol. RNA purity and concentration are measured using a ND-100 Nanodrop

spectrophotometer (Thermo Scientific). Total RNA is reverse transcribed (High Capacity cDNA Reverse Transcription Kit, Applied Biosystems) using 500 ng of RNA for each 20 μL reaction. We perform real-time polymerase chain reaction (qRT-PCR) using TaqMan Gene Expression Assays (Applied Biosystems) in a final volume of 20 μL containing 4 ng of template. Expression levels are normalized to levels of 18S and calculated as fold change ($2^{-\Delta\Delta CT}$) with respect to the scrambled negative control samples. To obtain absolute quantification of miR levels, we use droplet digital PCR (Bio-Rad). Purified RNA is polyadenylated using poly-A polymerase (New England Biolabs) following the manufacturer's protocol and reverse transcribed using the iScript Select cDNA Synthesis Kit (Bio-Rad). We measure the number of miRs detected in 2 μg of RNA for samples with low levels of miRs and 50 ng of total RNA for the samples with miR overexpression. Each 20 μL reaction containing 1x EvaGreenSupermix (Bio-Rad), 1x gene specific primers, and 4 μL of cDNA is partitioned into droplets using the QX200 droplet generator and then transferred to a 96-well plate for PCR amplification using a thermal cycler. After PCR, droplets are analyzed on a QX200 droplet reader to measure the target miR concentrations. We calculate the average miR copy number per cell based on the quantity of RNA extracted from ~10^5 cells from three independent experiments.

Predicted miR targeting

To clarify the molecular basis of the mechanotype changes observed with miR overexpression, we identify predicted tumor-suppressor miR targets that are implicated in regulating the mechanical properties of cells, including genes that encode for both structural and signaling proteins that regulate cytoskeletal structure and dynamics. We score genes as potential miR targets using three sets of binding site predictions: TargetScan (v7.1) [27], miRmap (201301e) [28], and miRanda-mirSVR [29], for mirSVR, we use target site predictions with 'good' scores for conserved miRs (miR-130b-3p) and for non-conserved miRs (miR-508-5p, miR-508-3p, miR-509-5p, miR-509-3p). We consider predicted targets that are in the top 50th percentile of scores for each method. Because a 3' UTR can have more than one predicted binding site for a mature strand of a given miR, we use a percentile based on the sum

of scores of all predicted sites for a mature strand on a 3' UTR. The total percentile scores reflect the expected effect of a miR in reducing a transcript's abundance, reporting percentiles facilitates comparing scores among methods.

Parallel microfiltration

To measure the ability of cells to deform through micron-scale pores, we use a parallel microfiltration (PMF) device [137] with polycarbonate membrane filters of 10 μm pore size (Millipore). To minimize cell-surface interactions, membranes and loading wells are treated with 1% bovine serum albumin (BSA) in deionized water for 1 hour at 37°C. Transfected cells are trypsinized at 72 hours post transfection, filtered through 35 μm filters to minimize cell clusters, and resuspended to a final concentration of 9×10^5 cells/mL in culture medium prior to loading. We determine the density of the cell suspension using an automated cell counter (TC20, Bio-Rad), these measurements also confirm that the majority of cells are single cells >88% (N=2) (Supplementary Material Figure 3a,b). To measure cell deformability using PMF, we apply a uniform air pressure of 7 kPa or 14 kPa for 45 seconds, collect the samples retained in the top wells, and calculate $Percentage\ Retention = (m_f / m_i) \times 100\%$, where m_i is the mass of cell suspension loaded and m_f is the mass remaining in the top well after filtration. Percentage retention depends on the driving pressure, the cell size relative to the pore size, and the intrinsic cell mechanical properties [78,113,137].

Microfluidic device fabrication and operation

For microfluidic deformation experiments, we use standard soft lithography techniques to fabricate polydimethylsiloxane (PDMS) (Sylgard 184 Silicone Elastomer, Dow Corning) devices. To probe cell deformability, we use a device design as previously described [138]. In brief, a master mold of the device is patterned from photoresist onto a silicon wafer. PDMS is molded onto the wafer and cured at 65°C for 4 hours, then removed, cleaned, and covalently bonded to glass coverslips after exposure to oxygen plasma. To minimize surface adhesion, we add 0.1% v/v F-127 surfactant (Invitrogen) to cell suspensions.

We use an applied pressure of 28 kPa to drive cells in suspension through the device constrictions. The resulting cell deformations are imaged using a high-speed camera (Phantom Miro EX1, Vision Research) mounted on an inverted light microscope (Zeiss) equipped with a 20x objective (20x/0.40 Ph2 Corr, LD Achroplan, Zeiss). Images are analyzed using a custom algorithm in Matlab (Mathworks) to extract cell size, which is determined before each cell enters the constriction, and transit time, stiffer cells tend to have longer transit times [82,83,109,113].

Imaging cells and subcellular structures

To visualize F-actin and determine cell/nuclear size, we image cells in suspension using the ImageStream multispectral imaging flow cytometer (Amnis Corporation). Cells are fixed in 4% paraformaldehyde and permeabilized with 0.2% Triton X-100. After blocking, cells are incubated with Alexa Fluor 488-phalloidin (Thermo Scientific), followed by DRAQ5 nuclear stain (Thermo Scientific). We measure morphological features such as cell size, nuclear size, and cortical-to-intracellular F-actin levels using the ImageStream Data Analysis and Exploration Software (IDEAS) (Amnis Corporation). To assess the distribution of F-actin, we determine the ratio of cortical-to-intracellular F-actin levels, where the cortical F-actin is measured by the average pixel intensity within $0 < 7$ pixels ($0 < 3.5$ μm) from the boundary of the cell, and intracellular F-actin is measured by the average pixel intensity within the internal region that is >3.5 μm from the boundary of the cell. Cell and nuclear sizes are determined by measuring the projected area and extracting the diameter assuming a perfect circle. To visualize F-actin in adhered cells, cells are seeded on collagen-coated glass slides, fixed with 4% paraformaldehyde, and labeled with Alexa Fluor 488-phalloidin. We perform confocal imaging using the Zeiss Laser Scanning Microscope (LSM 5 Exciter) equipped with a 63x objective (63x/1.2 W Korr UV-VIS-IR, C-APOCHROMAT, Zeiss), and argon ion (488 nm) and helium-neon lasers (633 nm) for excitation. We measure the total integrated fluorescence intensity of F-actin for individual cells using ImageJ and determine the fold-change fluorescence relative to the SCR treatment.

3 Tumor-suppressor MicroRNAs Regulate Ovarian Cancer Cell Physical Properties and Invasive Behavior

3.1 Introduction

High-grade serous ovarian cancer (HGSC) is the most lethal gynecologic cancer in the United States [139]. Most patients initially respond to platinum and taxane-based treatments, but subsequently develop chemoresistance, the five-year survival rate is only 44% [139]. The critical need for successful treatment strategies motivated the Cancer Genome Atlas (TCGA) Network to catalog the genetic alterations in ~500 HGSC samples [140]. Through computational analysis of TCGA data, we identified a panel of differentially expressed microRNA mature strands ('miRs': miR-508-3p, miR-508-5p, miR-509-3p, miR-509-5p, miR-130b-3p), for which higher levels of expression are associated with longer survival in HGSC patients [141]. Improved survival can be associated with reduced metastasis and decreased invasion of cancer cells. Our previous work shows that overexpression of tumor-suppressor miR-509-3p in human ovarian cancer cell lines impedes invasion through Matrigel matrices [141]. Furthermore, downregulation of miR-130b-3p is associated with cancer progression and multidrug resistance in ovarian cancer [142]. While miRs such as miR-509-3p impact proliferation and cell signaling behavior [143,144], which could influence metastatic dissemination and growth of cancer cells, the invasion and migration of cancer cells from a primary tumor involves physical and mechanical processes. Detailed biophysical investigations at the single cell level could thus deepen our understanding of how elevated levels of tumor-suppressor miRs may result in clinical benefits.

During cancer progression, tumor cells undergo changes in their physical properties, including their deformability and adhesion, which can contribute to their altered motility and invasive behavior [3,87,145]. Such physical properties are relevant for understanding how cells deform through narrow gaps in the circulatory system, which is required for metastasis [146], they are also essential for invasion through the extracellular matrix (ECM), connective tissue, and endothelial linings of blood or lymph vessels [147]. The ECM is composed of glycoproteins, proteoglycans, and fibrous proteins such as collagens [148], which form a network with gaps or pores that range in diameter from 10 nm to 5 μm [149–151], increased cell and nuclear volume is correlated with reduced invasion of breast cancer cells through *in vitro* collagen gels [152]. To overcome the physical constraints imposed by ECM barriers, cells secrete proteases, such as matrix metalloproteases (MMPs), which can increase the size of gaps between neighbouring fibers [153–155]. Many types of tumor cells are also more deformable compared to benign cells [29,76,156], and cell mechanical properties are associated with invasion efficiency [152,157,158]. Compared to less deformable ovarian tumor cells that have a higher Young's modulus or decreased compliance, cancer cells that are more deformable tend to move more quickly through the gaps of *in vitro* transwell migration and invasion assays [157,158]. Considering the large deformations required during extra- and intravasation as well as invasion into surrounding tissues, changes in the size and deformability of single tumor cells could play a functional role in disease progression. We hypothesize that altered cell physical properties may reduce cell invasion, and thereby contribute to the improved prognosis, which is associated with higher levels of tumor-suppressor miRs.

To determine the effect of tumor-suppressor miRs on cancer cell physical properties, we overexpress a panel of five miRs (miR-508-3p, miR-508-5p, miR-509-3p, miR-509-5p, miR-130b-3p) in human ovarian carcinoma cells (HEYA8, OVCAR8) using miR mimics for each. We characterize the ability of cells to invade through collagen matrices in the presence of an MMP-inhibitor, the inhibitor limits matrix degradation and enhances the extent to which cells must deform to move through the steric constraints of collagen gels. To determine cell deformability, we drive cells to passively deform through micron-scale

pores using microfluidic deformation [83,138] and parallel microfiltration (PMF) [137] assays. To gain insight into the molecular basis of the effects of tumor-suppressor miRs on cell physical properties, we identify predicted miR-mRNA targets that encode structural or signaling proteins that regulate cell mechanical properties, we also verify transcript levels of selected predicted targets. Through analysis of miR-mRNA interactions, our results show that these tumor-suppressor miRs are predicted to target genes that are implicated in the structure and remodeling of the actin cytoskeleton. By imaging cells in both suspended and adhered states using imaging flow cytometry and confocal microscopy, we observe increased levels of filamentous actin (F-actin) with miR overexpression, and a strong inverse correlation between invasive potential and F-actin levels in adhered cells. Taken together, our results reveal that these five tumor-suppressor miRs that reduce cell invasive behavior are implicated in the structure and remodeling of the actin cytoskeleton. Our findings also identify novel proteins for future study that may potentially serve as new druggable targets that play a role in ovarian cancer cell invasion and disease progression.

3.2 Results and discussion

In our previous work, we show that higher expression levels of the tumor-suppressor miRs, miR-508-3p, miR-508-5p, miR-509-3p, miR-509-5p, miR-130b-3p, in human ovarian tumors correlate with improved patient prognosis and can discriminate improved survival in HGSC patients [141](Gunaratne et al., submitted). Here, to obtain fold-change increases in miR levels that are similar to the increased levels between cancer patients at early versus advanced stages of disease [159,160], we transiently transfect miRs into HEYA8 and OVCAR8 ovarian cancer cells.

Quantification of miR expression levels

To determine how the fold-change increase in tumor-suppressor miRs with overexpression relates to clinical contexts, we first measure endogenous levels of miRs in HEYA8 and OVCAR8 cells using

droplet digital PCR (Figure 8). Our analysis reveals that these tumor-suppressor miRs have endogenously low copy numbers in the non-treated cells. For example, in HEYA8 cells, miR-130b-3p is present at ~ 1 copy per cell, while miR-508-3p, miR-508-5p, miR-509-3p, and miR-509-5p are even less abundant, ranging from 10^{-4} to 10^{-3} copies per cell (Figure 8a). Overall, the OVCAR8 cells show similar endogenous levels of miRs compared to the HEYA8 cells (Figure 8b). Following transient transfection of these miRs, expression levels in HEYA8 increase by up to 5 orders of magnitude up to 20 to 120 copies per cell 72 hours after transfection. The cells treated with miR-508-3p show the largest fold-increase of ~10^5, while levels of miR-130b-3p increase by ~10^2-fold. For OVCAR8, we observe up to a ~10^4 fold-increase in miR levels, with 50 to 160 copies per cell 72 hours after transfection. Across the panel of tumor-suppressor miRs, we observe on average a 10^4-fold increase in miR levels. These transient transfections generate changes in the levels of tumor-suppressor miRs that are similar to those observed in clinically relevant contexts. For example, miR-508-3p, miR-509-3p, and miR-509-5p are less abundant by ~10 to 10^3-fold in ovarian cancer patients with stage III versus stage I disease [159], and miR-508-3p and miR-508-5p are ~10 to 10^2-fold less abundant in metastatic serous epithelial ovarian tumors than in primary tumors [160].

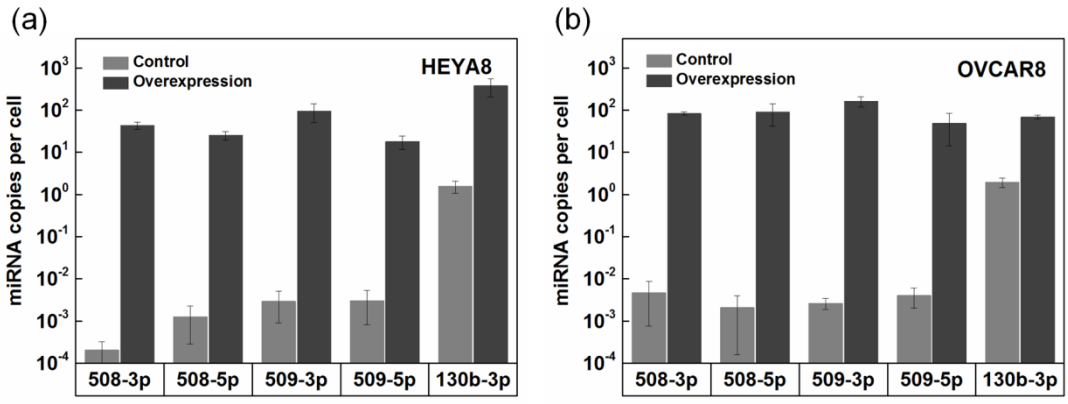

Figure 8. Quantification of miR levels using droplet digital PCR.

MiR copy number in negative control and miR-overexpressing samples 72 hours after transfection with tumor-suppressor miRs. Data is shown for (a) HEYA8 and (b) OVCAR8 cells. The average numbers of miR copies per cell are calculated based on the quantity of RNA extracted from ~10^5 cells. Error bars show the standard deviation of N=2 independent experiments.

MiR overexpression hinders cell invasion through collagen matrices

To deform through gaps of the ECM, invading cells undergo major changes in shape that are associated with cytoskeleton remodeling. The magnitude of cell deformation required to pass through narrow pores depends on the ECM network mesh size and mechanical properties of the fibrous proteins. To determine the extent to which elevated levels of miRs hinder cell invasion through an ECM, we perform invasion assays using a type I collagen matrix (Figure 9a), which is the most abundant structural component of the ovarian ECM [161]. Scanning electron microscopy (SEM) of the 1 mg/mL collagen gels that we use in our invasion assay reveals that the average gap size is 0.5 to 2 μm, this is significantly smaller than the 23 to 25 μm median diameter of cells overexpressing the tumor-suppressor miRs. Invading tumor cells can also increase the matrix gap size by secreting proteases that degrade collagen. Indeed, elevated levels of several MMPs, including MMP-2 and MMP-9, in ovarian cancer cells are associated with increased invasive potential, and with poor survival of ovarian carcinoma patients [162–164]. To reduce the potential role of matrix degradation and thereby enhance the requirement for cells to deform during invasion, we treat cells with the broadband MMP inhibitor, GM6001, which suppresses the invasion of cells through type I collagen matrices [165]. We confirm that GM6001 decreases protease activity in conditioned medium taken from cell culture 24 hours after treatment with GM6001 (Supplementary Material Figure 1).

Over the 24-hour invasion time course, the HEYA8 mock and SCR-treated control cells show progressive closure of the scratch wound. We observe no significant differences between mock and SCR-treated cells (94%, 83% relative invasion respectively, $p = 0.33$). By the endpoint of 24 hours, the wound is nearly

completely healed, with 83 to 94% wound closure (Figure 9b,c). By contrast, HEYA8 cells overexpressing miR-508-3p, miR-509-3p, and miR-130b-3p show a marked reduction in wound closure (41%, 10%, 31% relative invasion respectively, $p < 0.001$). Cells with elevated levels of miR-509-5p also show significantly reduced invasion compared to the mock and SCR cells (63% relative invasion, $p < 0.001$). Across our miR panel, we observe a significant decrease in wound closure rate with overexpression of all miRs except miR-508-5p. Compared to the HEYA8 cells, OVCAR8 cells show reduced invasion of the mock and SCR controls (34 to 36% relative invasion, $p < 0.001$). The more rapid invasion of HEYA8 cells compared to OVCAR8 is consistent with the mesenchymal phenotype of the HEYA8 cells versus the epithelial-like OVCAR8 cells, cell become more motile during epithelial-to-mesenchymal transition (EMT) [166]. Only miR-509-3p shows a significant decrease in wound closure and speed of the wound front in both cell lines (Supplementary Material Figure 2) ($p < 0.001$ in each cell line). The reduced invasion of miR-509-3p-overexpressing cells through collagen matrices is consistent with previous results showing decreased invasion of ovarian cancer cells through Matrigel [141], as well as reduced migration of human epithelial lung cancer and renal cancer cells in scratch wound assays [143,144]. Our results are also in agreement with other studies that show reduced invasion with miR-508-3p in gastric cancer [167] and renal cancer [143], and reduced invasion with overexpression of miR-130b-3p in pancreatic cancer [168].

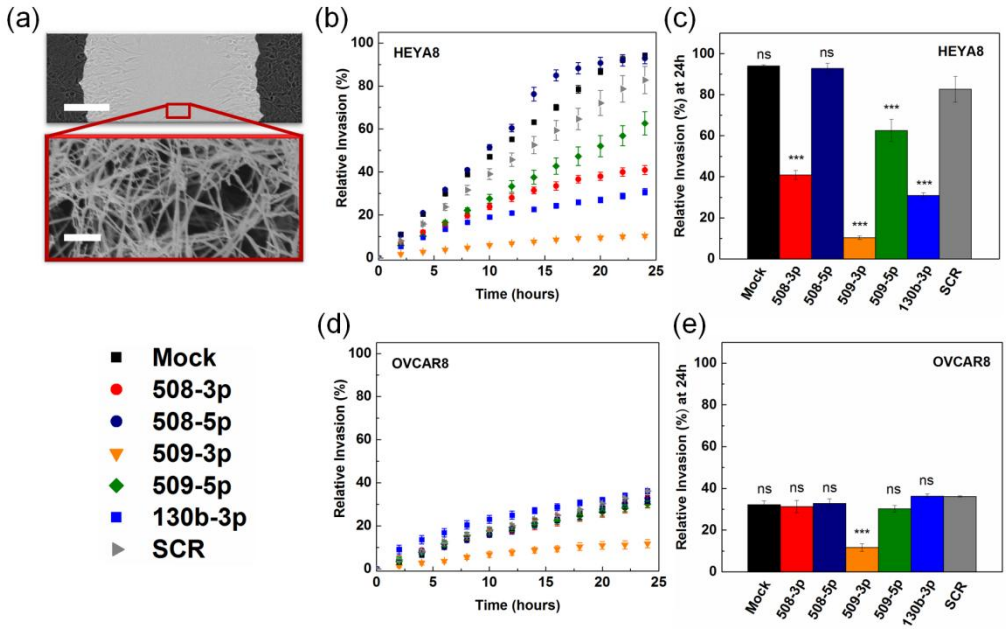

Figure 9. Effect of miR overexpression on cell invasion through a collagen matrix.

(a) Scratch wound assay where cells invade through a collagen gel. The upper panel shows a top view of the scratch, the cells on right and left sides invade into this wounded region, which is overlaid with a collagen gel. Scale, 200 µm. The bottom panel shows a scanning electron micrograph of the fibrous structure of a 1 mg/mL collagen gel. Scale, 1 µm. (b,d) Invasion time course for HEYA8 (N=3) and OVCAR8 (N=3) cells in 1 mg/mL collagen type I in the presence of a protease inhibitor, 50 µM GM6001. (c,e) Relative invasion of HEYA8 and OVCAR8 cells at 24 hours for different miR treatments. One-way ANOVA with a Tukey post hoc test: *** ($p < 0.001$), ns ($p > 0.05$), compared to the scrambled control treatment (SCR). All error bars show the standard error of the mean.

Elevated levels of miRs alter cell physical properties

To determine the effect of elevated levels of tumor-suppressor miRs on cell deformability, we perform a microfluidic deformation assay that enables us to measure both the size and transit time of single cells as they deform and pass through a micron-scale channel. In this assay, the time for transit exhibits a strong dependence on cell deformability, with cells that are more compliant having shorter transit times than stiffer cells [78,82,109,169,170]. Transit time also shows a weak dependence on cell size [109,171],

however, larger cells get filtered out in the upstream filter region of the device and we further size-filter the data to compare the transit times for cells of similar sizes across our miR panel (Figure 10b). Both HEYA8 and OVCAR8 cells that overexpress miR-508-3p, miR-508-5p, and miR-130b-3p have statistically significant longer transit times compared to the mock and SCR controls (Figure 10c,d). For miR-508-3p, we observe the longest median transit time in HEYA8, and also an increased median transit time for OVCAR8 compared to SCR (~8x longer median transit time for HEYA8, 2x for OVCAR8) ($p < 0.001$). For the OVCAR8 cells, we find a ~3x increased median transit time with overexpression of miR-130b-3p compared to the SCR cells ($p < 0.001$). We find a similar 2x increase in median transit time for both cell lines with overexpression of miR-509-3p compared to SCR control cells (OVCAR8, $p = 0.002$, HEYA8, $p = 0.06$). Our results also show a 3x increased median transit time with overexpression of miR-509-5p in HEYA8 cells (compared to SCR, $p < 0.001$), but no significant change for OVCAR8 cells ($p = 0.87$). Overall, our results show that overexpression of tumor-suppressor miRs results in an increase in transit time, indicating that cells overexpressing these miRs are less deformable.

To confirm measurements of cell deformability using an independent assay, we use parallel microfiltration (PMF) [137]. In PMF, a bulk suspension of cells is filtered through a membrane with 10 μm pores in response to applied air pressure (Figure 11a). We measure the percentage retention by determining the fraction of sample volume that is retained in the top loading well after applying pressure for a defined period of time. Cells that are less deformable are more likely to occlude the pores, resulting in higher retention, a larger cell size could also increase retention. Given the potential confounding effects of size on filtration, we display our retention data together with cell size distributions (Figure 11b-e). We observe that cells overexpressing different miRs exhibit similar cell size distributions, with median sizes that are within ± 2 μm (Figure 11b-e, Supplementary Material Table 1, Supplementary Material Figure 5a), suggesting that differences in retention are not strongly influenced by cell size but instead reflect differences in cell deformability among the different miR treatments.

Transfected HEYA8 cells that overexpress tumor-suppressor miRs consistently show a retention that is ~30 to 40% higher than the mock and SCR controls after 45 seconds of filtration through 10 μm pores at 7 kPa ($p < 0.001$) (Figure 11b). To resolve differences in retention between cells with different miR treatments, we increase the applied pressure. At a driving pressure of 14 kPa, we observe that the mock and SCR control samples completely filter through the membrane on the experimental timescale, this is consistent with our PMF results at lower pressure, where mock and SCR exhibit the lowest retention, indicating these cells are the most deformable (Figure 11c). HEYA8 cells that overexpress tumor-suppressor miRs show higher retention at 14 kPa, reflecting that more of these cells occlude the 10 μm pores even at this higher driving pressure. Cells with elevated levels of miR-508-3p and miR-509-3p show the highest retentions (92 ± 5% and 83 ± 5% respectively) compared to the other miR treatments ($p < 0.001$), while retention of miR-508-5p (59 ± 5%), miR-509-5p (39 ± 5%), and miR-130b-3p (56 ± 5%) overexpressing cells is still significantly higher than the control samples at this increased driving pressure (Figure 10c) ($p < 0.001$). By contrast, OVCAR8 cells show higher levels of retention than HEYA8 at the same pressures, this is consistent with the more invasive HEYA8 cells being more deformable. For OVCAR8 cells at 14 kPa driving pressure, we observe higher retention for miR-508-3p (82 ± 11%), miR-509-5p (86 ± 6%), miR-130b-3p (80 ± 8%) compared to the mock and SCR ($p < 0.001$), but no significant change in retention for cells treated with miR-508-5p ($p = 0.9$) and miR-509-3p ($p = 0.9$). Overall, we find that miR-508-3p results in the largest increase in retention in both HEYA8 and OVCAR8 cells. Overexpression of miR-509-5p and miR-130b-3p also result in consistently higher retention relative to the SCR control in both cell types.

The results of these complementary filtration and microfluidic methods to measure cell deformability are in good agreement. Overexpression of miR-508-3p in both HEYA8 and OVCAR8 causes increased retention and transit time, reflecting decreased cell deformability. While both methods probe the ability of cells to transit through micron-scale pores, we do not observe the same trends for all miRs, this could reflect differences in the readouts for the bulk (PMF) versus single cell (transit time) deformability assays

(see supplemental note for further discussion). For example, overexpression of miR-509-3p in HEYA8 cells results a slight shift to increased transit times, but a statistically significant increase in retention compared to SCR cells, this could result from occlusion due to the longer-transiting cells.

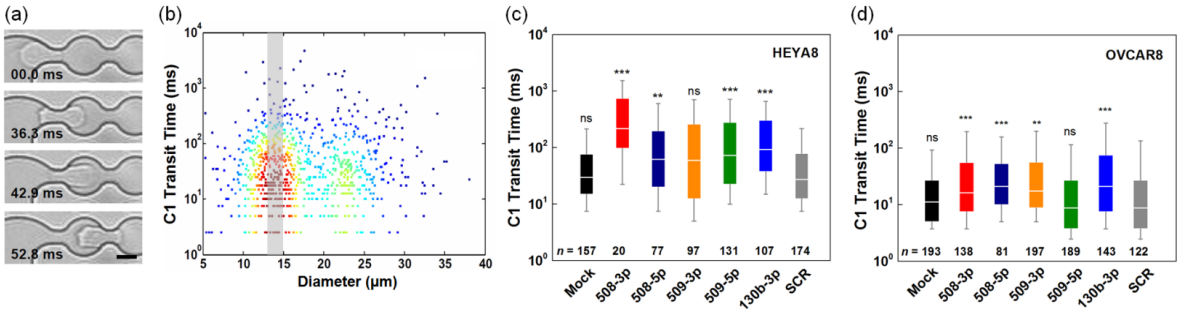

Figure 10. Cells that overexpress tumor-suppressor miRs have longer transit times through microfluidic constrictions.

(a) We apply air pressure of 28 kPa to drive cells through a polydimethylsiloxane (PDMS) microfluidic device with constrictions that have a width of 7 μm and height of 10 μm, the constriction diameter is approximately half the median cell size of 23 to 25 μm. Cell deformations are imaged using a high-speed camera and analyzed using a custom image processing algorithm to extract the time for each cell to transit through the first constriction (C1). Micrographs show a representative HEYA8 cell that has a transit time of 42.9 ms. Scale, 10 μm. (b) Density scatter plot showing relationship between cell size and transit time for n=889 individual SCR-treated HEYA8 cells. The shaded grey region indicates cells with an apparent diameter of 13-15 μm, we apply this size filter to compare cells of similar sizes across the miR panel. An upstream filter minimizes larger cells and cell aggregates from entering the constriction region. (c,d) Distributions of transit times for HEYA8 and OVCAR8 cells treated with tumor-suppressor miRs. Each panel displays the number of cells per sample, which are compiled over N=2 independent experiments. Horizontal lines denote medians, boxes represent the 25th and 75th percentiles, and whiskers show the 10th and 90th percentiles. SCR = scrambled control. Mann-Whitney test: ns (not significant), *** ($p < 0.001$), ** ($p < 0.01$) compared to the SCR treatment.

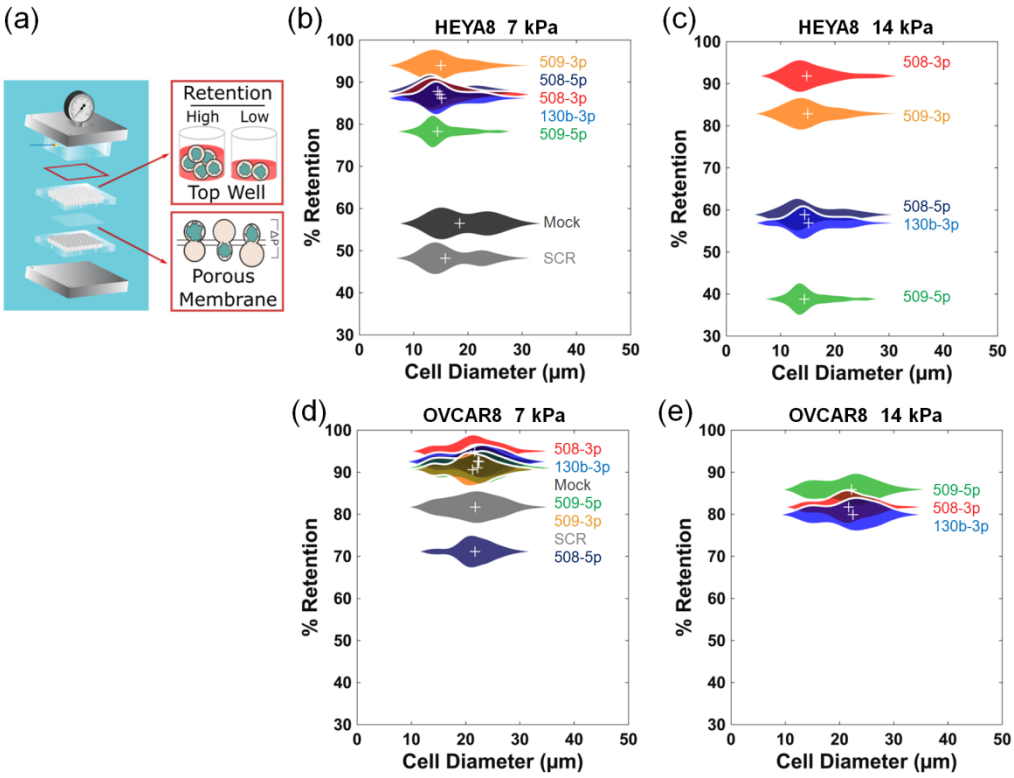

Figure 11. Cells that overexpress tumor-suppressor miRs show decreased filtration through a porous membrane.

(a) Schematic of the parallel microfiltration (PMF) setup. Figure adapted from [137]. A cell suspension is driven to flow through a membrane with 10 µm pores by applying air pressure across the multiwell device, a larger number of occluded pores results in increased retention. Percentage retention as a function of the cell-to-pore size ratio, after 45 seconds of filtration of (b,c) HEYA8 and (d,e) OVCAR8 cells with applied pressures of (left) 7 kPa and (right) 14 kPa. Data is from N=3 independent experiments. Violin plots show cell size distributions, crosses denotes the average retentions and median cell sizes.

Prioritizing genes of the mechanome that are implicated in cytoskeletal structure and dynamics

To determine the mechanisms through which the miRs in our panel could be inducing changes in cell physical properties, and ultimately invasive behavior, we determine predicted targets of miRs that could

be implicated in cell mechanical properties. We prioritize genes that encode major cytoskeletal proteins (such as vimentin), proteins that interact with components of the cytoskeleton (actin crosslinkers like filamin A), as well as proteins that regulate cytoskeletal organization (NF-κB). We assess the probability of miR-gene targeting that influences mRNA transcript levels using three independent and favourably ranked [172] sets of binding site predictions: TargetScan (v7.1) [27], miRmap (201301e) [28], and miRanda-mirSVR [29]. To enable comparisons of the predictions from each resource, we assess the binding site scores as percentiles with values between 0 and 1, and report only genes that are in the top 50th percentile of targets for all three resources, or are validated targets (Figure 12a). Below, we summarize predicted and validated targeting that is relevant for the effects of our tumor-suppressor miRs on cell deformability.

miR-508-3p. NFKB1, which encodes the protein NF-κB, is a predicted target of miR-508-3p (TargetScan = 0.96, mirSVR = 0.90, miRmap = 0.82). This miR is validated as inactivating canonical NF-κB signaling in gastric cancer cell lines and primary tumors [167,173,174]. NF-κB disrupts tissue organization and cellular morphology, it is a regulator of genes involved in actin organization and cell adhesion in breast cancer cells [175]. Another predicted target of miR-508-3p is leupaxin (**LPXN**) (TargetScan = 0.97, mirSVR = 0.73, miRmap = 0.62), which is a member of the paxilin family of focal adhesion proteins. Leupaxin directly affects cytoskeletal organization and dynamics through its interaction with the actin-binding protein caldesmon (**CALD1**) [176,177].

miR-508-5p. ACTR2 is a highly-scoring predicted target of miR-508-3p (TargetScan = 0.99, mirSVR = 0.94, miRmap = 0.89), which encodes a major constituent of the ARP2/3 complex that is essential for lamellipodial actin assembly and protrusion formation, both of which are implicated in cell motility [178].

miR-509-3p. Predicted targets of this miR include **YAP1** (TargetScan = 0.96, mirSVR = 0.95, miRmap = 0.97), which encodes the Yes associated transcription factor Yap1 that is implicated in regulation of tissue tension, cell shape and migration [179]. The effects of Yap1 on the actin cytoskeleton are regulated

via the Rho GTPase, **ARHGAP18**, which suppresses F-actin polymerization by inhibiting RhoC [180] and RhoA [181]. Recently we validated YAP1 as a direct target of miR-509-3p [141]. We also identify **ARHGAP1,** the Rho GTPase-activating protein 1, as a potential target of miR-509-3p (TargetScan = 0.92, mirSVR = 0.76, miRmap = 0.78), this protein also regulates assembly of F-actin [182]. While **RAC1**, which is a member of the Rho family of GTPases, scores highly as a predicted target using only one method (TargetScan = 0.99), it is a validated target of miR-509-3p [144]. Rac1 contributes to the formation of membrane protrusions and cell-matrix adhesions that are essential in cell motility [183], and is also overexpressed in several types of tumors [184–186].

miR-509-5p. The intermediate filament protein, vimentin (**VIM**), is a highly-scoring predicted target of miR-509-5p (TargetScan = 0.97, mirSVR = 1.00, miRmap = 0.95). Vimentin is widely used as a biomarker for mesenchymal-type cells. This protein is also observed to promote cell motility and increase focal adhesion dynamics during epithelial to mesenchymal transition [187]. Depletion of vimentin also results in reduced cell stiffness [188–190]. MiR-508-5p also is predicted to target **RHOC** (TargetScan = 0.99, mirSVR = 0.66, miRmap = 0.77), which encodes a Rho GTPase protein that plays an important role in cell motility [191,192]. RhoC expression positively correlates with cancer metastasis in melanoma and breast cancer [191,193,194].

miR-130b-3p. The tumor-suppressor **PTEN**, encoding phosphatidylinositol-3,4,5-trisphosphate 3-phosphatase, is a validated target of miR-130b-3p [195] that is also highly-scored as a predicted target (TargetScan = 0.94, mirSVR = 0.87, miRmap = 0.95). Downregulation of PTEN promotes the motility of fibroblasts through stimulation of Cdc42 and Rac1 activity [195–197]. Another predicted target of miR-130b-3p is **DIAPH3** (TargetScan = 0.67, mirSVR = 0.81, miRmap = 0.93), which encodes for Diaphanous-related formin-3 (Drf3). Drf3 binds to profilin (**PFN1**) [198,199] and guides its downstream effector, Cdc42, to the cell cortex where it plays a role in remodeling the actin cytoskeleton [200]. This formin is essential in multiple processes that rely on actin polymerization, such as blebbing [201] and

actin nucleation in the formation of cellular protrusions [202], it also localizes to stress fibers and filopodia [203]. MiR-130b-3p is also predicted to target **CALM2**, the calcium-binding protein, calmodulin (TargetScan = 0.99, mirSVR = 0.85, miRmap = 0.83). Complexes of calmodulin and Ca^{2+} bind to the actin-binding domain of filamin A, an actin crosslinking protein, dissociating filamin A from F-actin, thereby dissolving gels of filamin A and F-actin [204]. The Rho GTPase-activating proteins 1 (**ARHGAP1**) and 12 (**ARHGAP12**) are also predicted targets of miR-130b-3p (ARHGAP1: TargetScan = 0.94, mirSVR = 0.76, miRmap = 0.90, ARHGAP12, TargetScan = 0.97, mirSVR = 0.79, miRmap = 0.95). Rho GTPase-activating proteins (GAPs) stimulate Rho GTPase activity and promote the conversion of active GTP-bound proteins to the inactive GDP-bound state. In the activated state, Rho GTPases regulate F-actin assembly and enhance stress fiber formation [205,206].

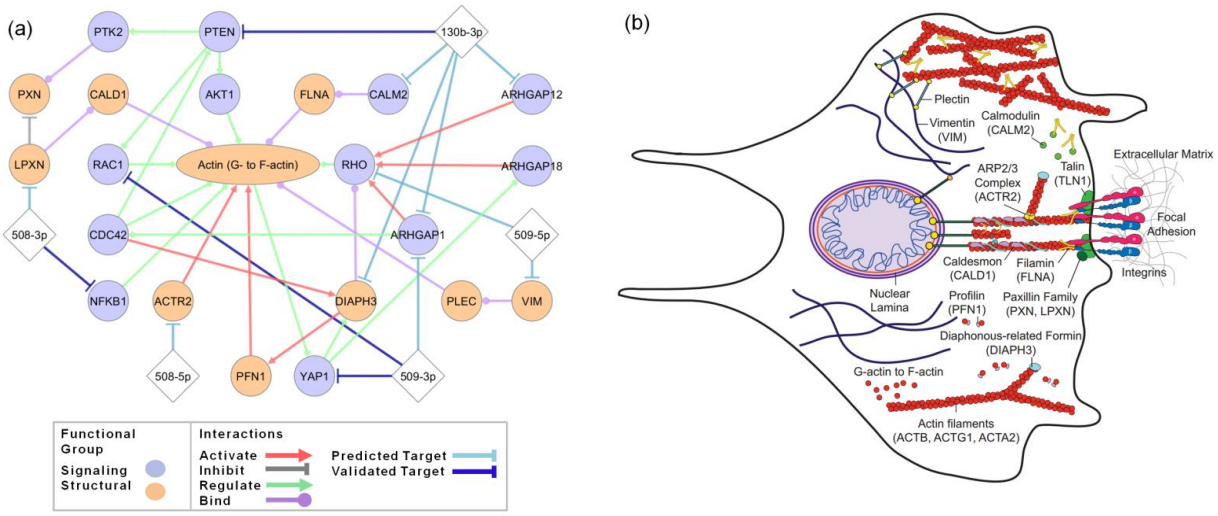

Figure 12. Predicted effects of tumor-suppressor miRs on cytoskeletal structure and dynamics.

(a) Network showing predicted and validated miR targets and functionally-annotated protein-protein interactions for structural and signaling proteins that are known to regulate the mechanical properties of cells. Predicted miR-mRNA targets are determined using TargetScan v7.1, miRanda-mirSVR, and miRmap, all targets displayed have scores in the top 50th percentile of predicted targets for all three methods, except for RAC1, which is a validated target of miR-509-3p.

Experimentally validated direct miR-mRNA targets are denoted by dark blue lines. Diamonds represent miRs, circles represent genes, and the ellipse represents actin, which exists as both monomers (G-actin) and filaments (F-actin). RHO denotes RhoA, RhoB, and RhoC, which have high sequence homology [191,192,207] . While RHOC is a highly-scoring predicted target of miR-509-5p, and RHOA is regulated by ARHGAP18 [181], the preferred substrates for other RhoGTPase activating proteins are not fully understood. (b) Schematic illustrating regulation of the architecture and dynamics of the actin cytoskeleton.

Expression of key mechanoregulating genes is altered by tumor-suppressor miRs

To experimentally confirm the altered expression of select candidate targets following miR overexpression, we measure transcript levels at 72 hours post-transfection using real-time polymerase chain reaction (qRT-PCR). We observe a significant increase in ACTA2 (smooth muscle α-actin) (2 to 6-fold) following treatment with miR-508-3p, miR-508-5p, and miR-130b-3p in HEYA8 cells ($p < 0.01$), but no observable change following miR-509-3p overexpression ($p > 0.05$). Overexpression of miR-130b-3p also reduces invasion and shows a ~2-fold increase of ACTA2 in HEYA8 cells ($p < 0.01$). While miR-508-5p also results in a similar ~2-fold higher expression of ACTA2 in HEYA8 cells ($p < 0.01$), a small increase in transit time and retention ($p < 0.01$), we observe no significant effect on invasion ($p = 0.4$). For OVCAR8 cells, only miR-130b-3p results in a significant change in ACTA2 levels ($p < 0.001$), in contrast to HEYA8 cells, there is a decrease in ACTA2 levels in OVCAR8 cells ($p < 0.001$). Smooth muscle α-actin associates predominantly with stress fibers or microfilament bundles [208], and its expression correlates with impaired motility in fibroblasts [209]. However, increased ACTA2 levels are also associated with invasion in breast and lung cancer [210,211]. The role of β-actin isoforms, which are encoded by ACTB, in cytoskeletal organization and cell migration is less well understood, β-actin is observed to accumulate in cellular protrusions involved in motility [212], while other studies report that β-actin is predominately found in stress fibers and at cell-cell adhesions [213]. ACTB levels are not significantly altered in HEYA8 cells, but we observe a significant decrease with overexpression of miR-508-3p ($p < 0.01$), miR-509-3p ($p < 0.001$), and miR-509-5p ($p < 0.05$) in OVCAR8 cells.

In addition to actin, we identify VIM and YAP1 as predicted miR targets and regulators of cell mechanical properties and mechanotransduction. With overexpression of miR-509-5p, we observe decreased vimentin expression in both HEYA8 ($p = 0.07$) and OVCAR8 cells ($p < 0.001$), these observations are consistent with our target predictions (VIM: TargetScan = 0.97, mirSVR = 1.00, miRmap = 0.95) (Figure 12). We also observe changes in vimentin levels with overexpression of other tumor-suppressor miRs. For example, in HEYA8 cells we observe a ~2-fold ($p = 0.003$) increase in transcripts encoding for vimentin with miR-508-3p, by contrast, OVCAR8 cells exhibit a <2-fold decrease in vimentin with miR-508-3p ($p = 0.04$), miR-509-3p ($p = 0.003$), and miR-130b-3p ($p = 0.03$). Increased expression of vimentin is a marker for EMT, which is associated with disease progression [187], however, the role of vimentin in cancer cell mechanical properties is not fully understood [189,214]. As a cytoskeletal intermediate filament protein, vimentin can contribute to cell stiffness [188–190] and may enable cells to resist large deformations: *in vitro* vimentin networks stiffen when deformed by large stresses that can rupture actin networks [60]. Vimentin also binds to plectin which mediates interactions of intermediate filaments with actin and microtubules [215–217] (Figure 12b).

YAP1 is a predicted target of miR-509-3p (TargetScan = 0.96, mirSVR = 0.95, miRmap = 0.97), and a transcriptional co-activator and oncogene that senses mechanical cues, intracellular tension [218,219], as well as cell structure, shape, and polarity [218,220–222]. With miR-509-3p overexpression we observe a significant ~5-fold downregulation of YAP1 in both HEYA8 and OVCAR8 cells ($p < 0.001$) (Figure 13). We previously established YAP1 to be a direct downstream target of miR-509-3p [141]. There is also a ~2-fold downregulation of YAP1 with miR-508-3p treatment in OVCAR8 cells ($p = 0.003$) but no significant change in HEYA8 cells. Since Yap1 is involved in mechanosensing and regulating cytoskeletal tension [218,219], we speculate that this protein could influence the invasive behavior by dynamically regulating cell deformability and traction forces as a cell migrates through narrow gaps. However, the precise role of YAP1 in regulating the invasive potential and deformability of single cells remains to be clarified.

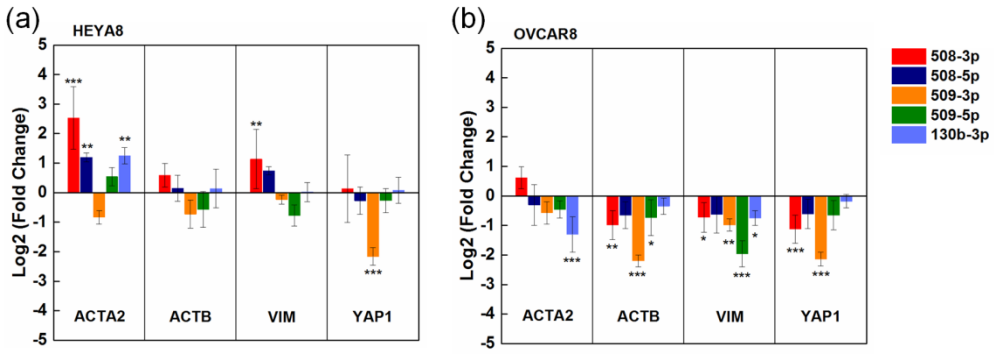

Figure 13. Expression of mechanoregulating genes is altered by overexpression of tumor-suppressor miRs.

Quantification of gene expression levels in miR-transfected (a) HEYA8 and (b) OVCAR8 cells relative to the SCR negative control, as measured by qRT-PCR using the delta delta cycle time method (ΔΔCt) with 18S ribosomal RNA as an endogenous control. Error bars show standard deviations of N=3 independent experiments.

Understanding the origins of altered deformability and invasive behavior

To further dissect the origins of the increased retention and transit times that we observe with transfection of tumor-suppressor miRs, we identify genes associated with regulation of the cytoskeleton, which is a key regulator of cell mechanotype [29,223]. The network shown in Figure 12a focuses on miRNA-mRNA and protein-protein interactions, complementing this, the relevant molecular complexes and structures that can determine cell physical properties are illustrated in the schematic shown in Figure 12b. Many of the predicted and validated targets converge on regulation of the actin cytoskeleton. Actin is a major cytoskeletal protein that has three main isoforms in mammalian cells: α-actins are a major component of the contractile apparatus, while β and γ-actins primarily regulate cell motility. These actin isoforms exist as monomers (G-actin), which can polymerize to form filaments (F-actin) that play a key role in the morphological changes and physical forces generated during migration [224,225]. The role of actin in regulating single cell mechanical properties is well established [29,82,170]. Here we experimentally

confirm the predicted changes in actin levels in the HEYA8 cells, which show a more pronounced increase in monomeric actin levels than in the OVCAR8 cells.

To quantify levels and organization of F-actin in populations of miR-treated cells, we investigate cells that are adhered to a collagen-coated substrate and labeled with phalloidin, cells also adhere to collagen during invasion (Figure 9) [148]. We find that HEYA8 cells with elevated levels of miR-508-3p, miR-509-3p, and miR-130b-3p show a 2 to 3-fold increase in F-actin levels ($p < 0.05$), whereas cells with elevated levels of miR-508-5p and miR-509-5p show a slight, albeit not statistically significant, increase in F-actin (Figure 14c).

While knowledge of actin structure in adhered cells is relevant for invasion, investigating F-actin in suspended cells is relevant to our deformability assays, which measure cells in suspension. Knowledge of subcellular architecture for suspended cells may also be relevant because cells transit and deform through vasculature during metastasis [226]. We next use imaging flow cytometry to image single cells in suspension, after being fixed and stained with phalloidin. Representative images are shown in Figure 14b. Compared to the mock and SCR controls, cells overexpressing tumor-suppressor miRs have increased F-actin (Figure 14b,d). We observe the largest increase in F-actin levels for cells that overexpress miR-508-3p, which exhibit ~8-fold higher levels of relative fluorescence intensity compared to the mock and SCR controls (Figure 14d). Cells overexpressing other tumor-suppressor miRs (miR-508-5p, miR-509-3p, miR-509-5p, miR-130b-3p) show ~2 to 4-fold higher levels of F-actin relative to the controls.

We also investigate levels of F-actin in the cortical region, as these are critical for cell deformability [61,227]. Interestingly, our results show that cells with elevated levels of miR-508-3p, miR-509-3p, or miR-130b-3p, which are less deformable, have lower levels of cortical-to-internal F-actin than the mock and SCR cells (Supplementary Material Figure 6). While lower levels of cortical F-actin are typically associated with a more deformable cortical region, as measured by methods that induce nanometer to submicron deformations [64], our PMF and transit time measurements probe cells as they transit through

pores that are roughly half their size. The relatively large deformations in our mechanotyping methods may explain why levels of cortical-to-internal F-actin do not correlate with our deformability results, these observations are in agreement with our previous report that the ratio of cortical-to-internal F-actin cannot predict retention of ovarian cancer cells during epithelial-to-mesenchymal transition (EMT) [137].

Across the miR panel, we observe a similar trend in overall F-actin levels between cells in an adhered versus suspended state, with smaller fold-changes in F-actin levels in adhered cells (Figure 14). For example, for cells overexpressing miR-508-3p, there is an 8-fold increase in F-actin in suspended cells ($p = 0.003$), and only a 3-fold increase in adhered cells ($p < 0.001$). The difference in phalloidin intensity between cells in suspended versus adhered states is consistent with how we image them: for flow cytometry imaging, we capture light that is emitted from the entire cell volume, whereas for confocal microscopy, we measure fluorescence signal from a single confocal slice. Taken together, our imaging data for both adhered and suspended cells are generally consistent with our qRT-PCR analyses, which show a significant increase in ACTA2 (1.5 to 6-fold) with overexpression of miR-508-3p, miR-508-5p, miR-509-5p, and miR-130b-3p.

Since changes in the actin cytoskeleton can induce changes in cell volume [228,229], and larger cells exhibit reduced invasion [15,152]**,** we also investigate cell size. To determine differences in cell volume with miR overexpression, we analyze our flow cytometry imaging data, the size of cells in a suspended state can be measured independently from the effects of cell spreading that occur when cells are adhered to a substrate [10,24]. We observe that cells with elevated levels of tumor-suppressor miRs are on average 5 to 20% larger than the parental cells and negative control treated cells: the median diameter of cells treated with tumor-suppressor miRs range from 23 to 25 μm, while the SCR control cells have a median diameter of 22 μm (Supplementary Material Table 1a, Supplementary Material Figure 5a). By staining cells with DRAQ5, we also obtain measurements of nuclear size. We observe that the median diameters of nuclei in miR-treated cells range from ~11 to 13 μm, this is ~10 to 26% larger than the nuclei of the

SCR control cells, which have a median diameter of 10 µm ($p < 0.001$) (Supplementary Material Table 1b, Supplementary Material Figure 5b). An increase in cell and nuclear size could contribute to increased transit time and retention, however, cell and nuclear size do not exhibit significant correlations with either transit time (cell size: $R = 0.61$, $p = 0.14$, nuclear size: $R = 0.36$, $p = 0.42$) or retention (cell size: $R = 0.82$, $p = 0.09$, nuclear size: $R = 0.66$, $p = 0.23$) (Figure 15), suggesting that these deformability measurements are not dominated by cell size.

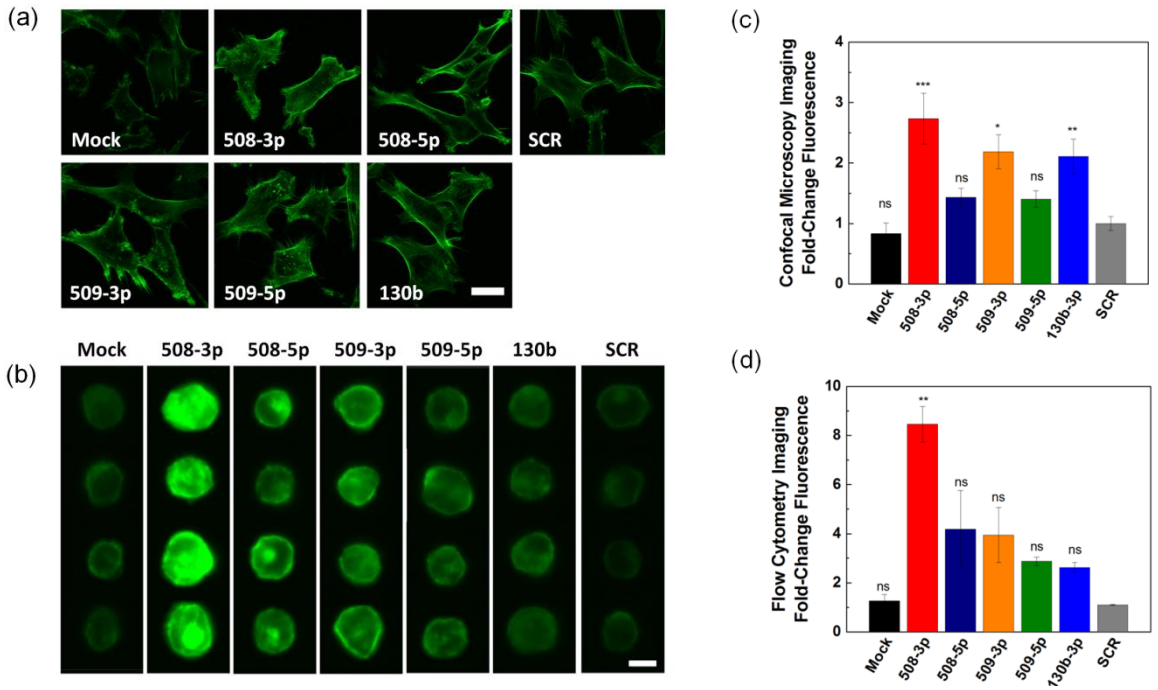

Figure 14. Subcellular structure with elevated levels of tumor-suppressor miRs.

(a) Confocal microscopy images of HEYA8 cells attached to collagen-coated glass slides. Scale, 20 µm. (b) Representative images of HEYA8 cells in suspension obtained by flow cytometry imaging. Scale, 10 µm. (c) Measurements of the integrated fluorescence intensity of single cells in the adhered state. At least 24 cells are analyzed for each sample over N=3 independent experiments. (d) Quantification of the relative fluorescence intensity of F-actin per single cell based on flow cytometry imaging. At least 3991 cells are analyzed for each sample over N=3 independent experiments. One-way ANOVA with a Tukey post hoc test, *** ($p < 0.001$), **($p < 0.01$), ns ($p > 0.05$), compared to the scrambled control treatment (SCR). Error

bars show standard error of the mean.

Determining correlations between cell physical properties and invasive behavior

To summarize the major contributions of cell physical properties to invasive behavior across the panel of tumor-suppressor miRs, we determine the strength and significance of correlations between invasion and cell size, nuclear size, deformability (retention and transit time), and F-actin levels (Figure 15).

Cell invasion is negatively correlated with cell and nuclear size. We find that across the panel of tumor-suppressor miRs, cell size negatively correlates with invasion efficiency (R = -0.85, $p < 0.05$), these results are consistent with previous observations in fibroblast (HT-1080), lung (A125), and breast cancer cells (MDA-MB- 231) [15,152]. The nucleus is typically the largest and stiffest organelle, occupying a substantial volume of the cytoplasm and rate-limiting the transit of cells through micron-scale pores [39,48], nuclear size is also associated with how effectively cells invade through collagen gels [152]. We observe a moderately strong negative correlation between invasion and nuclear size (R = -0.83, p = 0.02), reflecting how overexpression of some miRs results in increased nuclear size as well as reduced invasion, while overexpression of other miRs results in larger nuclei but no significant change in invasion efficiency. Thus, while there are strong correlations between invasive potential and cell/nuclear size, this feature alone cannot predict how an individual miR will impact cell invasive potential. Given recent observations of nuclear rupture and repair during the migration of cells through confined geometries [231], it remains to be determined how nuclear size may impact disease progression *in vivo*.

Less invasive cells tend to be stiffer. To determine the deformability of populations of single cells treated with a panel of miRs, we perform transit time measurements. We also obtain complementary data using PMF, which provides a bulk measure of the deformability of a cell suspension. Considering the panel of miRs, we observe a moderate correlation between invasive behavior and retention (R = -0.51, p = 0.38) as well as transit time (R = -0.43, p = 0.33), reflecting that less deformable cells tend to be less

invasive. Overall, the increased F-actin levels in suspended cells that overexpress tumor-suppressor miRs provides a likely explanation of their stiffer mechanotype. We observe a significant correlation between F-actin levels in suspended cells and transit time ($R = 0.92$, $p = 0.003$), reflecting that transit time measurements are sensitive to cytoskeletal organization in a suspended state, and further indicating that F-actin levels are a major contributor to transit time in cells overexpressing tumor-suppressor miRNAs. However, we also observe marked differences in the extent to which tumor-suppressor miRs impact cell deformability and invasive behavior. We find a relatively strong correlation between cell deformability and invasive potential for miR-508-3p and miR-509-3p, these observations are consistent with previous results showing that less deformable ovarian and breast cancer cells have decreased invasion efficiency [152,157,158]. However, for other miRs there is little correspondence between deformability and invasion. For example, cells overexpressing miR-508-5p show increased retention but no significant change in their invasive behavior, cells with elevated levels of miR-130b-3p are significantly less invasive but only moderately less deformable. We note that invasion is an active process during which the cell adheres to a substrate and remodels its cytoskeleton on timescales of minutes to hours, while our deformability measurements probe the passive deformability of cells in suspension on timescales of milliseconds to seconds [232].

F-actin levels for adhered cells show the strongest correlation with invasive potential. Our correlation analyses also reveal a strong negative correlation between wound closure and F-actin levels in adhered cells ($R = -0.89$, $p = 0.008$), suggesting that F-actin could be an indicator of cell invasive potential. While increased F-actin content is correlated with increased invasion and cell motility in lymphoma cells [233], other studies report that malignant cells exhibit a marked decrease in F-actin compared to normal keratinocytes [234]. Additional factors can also regulate actin structure and organization, including regulatory proteins, which are involved in the potential interaction pathways that we identify, such as DIAPH3 [235], this formin promotes the formation of actin-rich protrusions involved in cell migration and invasion. For suspended cells, we find a negative albeit not statistically significant

correlation between F-actin levels and wound closure (R = -0.44, p = 0.33), indicating that the organization of cytoskeletal actin in adhered cells is more tightly associated with invasive potential.

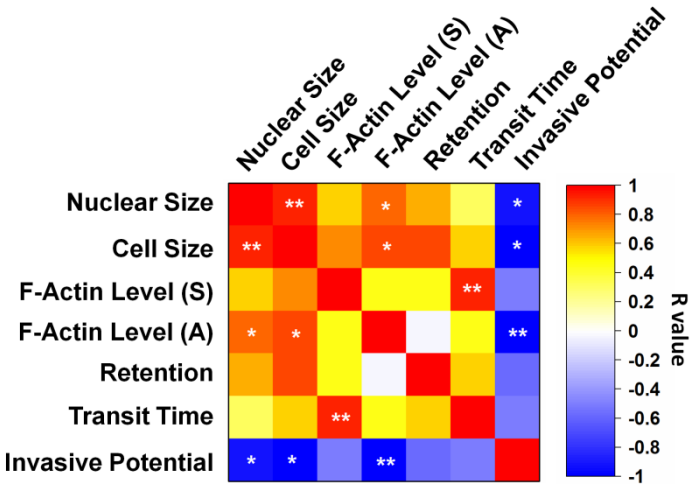

Figure 15. Correlations between invasion, cell physical properties, and F-actin levels across the panel of tumor-suppressor miRs.

Pearson correlation coefficient (R value) between nuclear size, cell size, F-actin levels in suspended (S) and adhered (A) cells, retention, transit time, and invasion of cells with elevated miR expression. *($p < 0.05$), **($p < 0.01$) indicates statistically significant correlations.

Potential mechanisms for how miRs alter cell mechanotype and invasive behavior

Here we use predicted and validated targeting relationships to associate the miRs with mRNA targets that encode structural and signaling proteins that regulate cell mechanical properties and mechanosensing. We are thereby able to identify mechanisms by which altered levels of tumor-suppressor miRs may alter regulation of cytoskeletal actin to make cancer cells less deformable and less invasive. Changes in cell mechanotype can occur due to regulation of F-actin structure and dynamics, this can be mediated by actin-associated proteins, such as crosslinkers of actin filaments [236]. Remodeling of the actin cytoskeleton is required for numerous processes in cancer invasion, including invadopodia formation and

motility [237,238]. Our work identifies several targets whose potential role in ovarian cancer progression warrants further investigation.

We focus first on dissecting the possible mechanism of the phenotype induced by miR-508-3p overexpression, which includes a strong decrease in invasion, increased transit time, and retention. Overexpression of miR-508-3p also results in the largest increase in F-actin and ACTA2 transcript levels in HEYA8 cells. A strong predicted target of miR-508-3p is leupaxin (LPXN). Leupaxin interacts with integrins and regulates the lifetime of adhesion sites [239], since actin polymerization is required for focal adhesion formation, we speculate that reduced LPXN expression may alter actin remodeling, and thereby affect cell deformability. Leupaxin is also an interaction partner of the actin-binding protein caldesmon, and thereby directly affects cytoskeletal structure and dynamics [176,177]. However, analysis of LPXN expression using the Cancer Genome Atlas database through cBioPortal reveals upregulation in only 4% of patients [240,241] (Supplementary Material Figure 7), and may therefore have limited clinical impact. Similarly, miR-508-3p overexpression in the p53-mutant OVCAR8 cells shows no significant effects on invasion.

We find that miR-509-3p overexpression results in significantly reduced invasion for both HEYA8 and OVCAR8, as well as increased transit times and retention, which reflect a trend to decreased deformability. Our results showing reduced YAP1 levels in HEYA8 and OVCAR8 with miR-509-3p overexpression are consistent with Yap1 being a validated target of miR-509-3p in ovarian cancer cells [141]. Downregulation of YAP1 by miR-509-3p could also alter cell mechanical properties by regulation of ARHGAP18, this Rho GTPase-activating protein (RhoGAP) regulates the activity of RhoC [180] and RhoA [181]. Suppression of ARHGAP18 could thus lead to accumulation of active Rho and increased F-actin polymerization, which is consistent with our imaging results for both adhered and suspended cells following overexpression of miR-509-3p. Furthermore, increased levels of miR-509-3p and decreased Yap1 levels correlate with improved overall survival, as determined by analysis of TCGA data [141].

In addition to ARHGAP18, our results reveal that ARHGAP1 and ARHGAP12 are regulators of multiple pathways. ARHGAP1 is another predicted target of miR-509-3p, ARHGAP1 and ARHGAP12 are predicted to bind to miR-130b-3p. Depletion of ARHGAPs could lead to increased activation of Rho proteins and the formation of stress fibers [181,242], this is consistent with our results showing increased F-actin and decreased cell deformability in HEYA8 cells that overexpress miR-509-3p (figures 3,4,7). Although many RhoGAPs appear to have anti-tumorigenic effects in other cancer types [242–245], ARHGAP1, ARHGAP12, and ARHGAP18 may have clinical relevance in ovarian cancer: analysis of The Cancer Genome Atlas dataset through cBioPortal [240,241] reveals that across 603 patient tumor samples, there is upregulation or amplification of ARHGAP12 in 11% of patients, of ARHGAP1 in 5% of patients, and of ARHGAP18 in 4% of patients (Supplementary Material Figure 7). These findings warrant further investigations of the role of these ARHGAPs in ovarian cancer cell invasion and disease progression.

Rho proteins are also found in other pathways of our interaction network. For example, RhoC is a predicted target of miR-509-5p. Depletion of this RhoGTPase reduces invasion in different cancer types from prostrate to breast cancer [246]. RhoC is also a validated target of miR-493 and miR-138, which reduce the migration of cancer cells [247,248]. RhoA is an effector of Diaphanous-related formin-3 or DIAPH3, which is implicated in multiple interaction pathways (Figure 12a). DIAPH3 is in the miR-509-3p/Yap1/DIAPH3/actin axis and is also a predicted target of miR-130b-3p, although overexpression of this miR results in decreased invasion in HEYA8 cells only. While the role of DIAPH3 in cell mechanical properties is poorly understood, DIAPH3 may affect cell deformability through its interactions with actin [203] and microtubules [249]: DIAPH3 remodels the cytoskeleton by nucleating and elongating nonbranched actin filaments, thereby promoting F-actin formation [250]. Indeed, the downregulation of DIAPH3 in early to late stage ovarian cancer cells is accompanied by disruption in F-actin accumulation [251]. DIAPH3 also nucleates actin via Cdc42 [200], and thereby contributes to remodeling of the actin cytoskeleton, including the formation of protrusions that are implicated in cell motility. For example,

DIAPH3 is enriched in the cellular protrusions of collagen-embedded OVCA429 spheroids, and also contributes to the invasion of ovarian cancer cells in 2D cultures [252]. Consistent with those findings, we find that overexpression of miR-130b-3p, which is predicted to target DIAPH3, results in reduced invasion of HEYA8 cells. DIAPH3 could also impact cell invasive behavior through the miR-509-3p/Yap1/DIAPH3/actin axis. Since expression of DIAPH3 correlates with levels of active Yap1 [253], and overexpression of miR-509-3p reduces Yap1 levels [141], we hypothesize that miR-509-3p overexpression could also decrease DIAPH3 levels, which could destabilize actomyosin structures and thereby cause cells to be less contractile and less invasive.

Differences between HEYA8 and OVCAR8. While we observe that miR-509-3p overexpression has a significant effect on the invasion and deformability of both HEYA8 and OVCAR8 cells, we also observe differences in the behaviors of these two cell lines. For example, we find that miR-508-3p, miR-509-3p, and miR-130b-3p all significantly reduce invasion of HEYA8 cells, but do not have a significant effect on the invasive behavior of OVCAR8 cells. The different trends that we observe between these two cell lines likely reflect their distinct genetic backgrounds: while HEYA8 is p53-wildtype, OVCAR8 is p53-mutant. Mutation of the tumor-suppressor protein p53 may impact levels of key genes in our interaction network, such as ACTA2 and NFKB1. Wildtype p53, but not mutant p53, promotes increased activity of the smooth α-actin promoter [208,254], which is consistent with the higher endogeneous levels of ACTA2 in HEYA8 cells versus OVCAR8 that we observe by qRT-PCR (Supplementary Material Figure 8a) and also by analysis of mRNA expression data from The Broad-Novartis Cancer Cell Line Encyclopedia (CCLE) [255] (Supplementary Material Figure 8b). We speculate that the higher endogenous expression of ACTA2 in HEYA8 compared to OVCAR8 cells could lead to the larger increase in ACTA2 levels with miR-508-3p overexpression. Compared to HEYA8 cells, OVCAR8 cells also have lower levels of NFKB1 and higher levels of the Rho GTPase, RHOB (Supplementary Material Figure 8b), this is consistent with the suppression of NF-κB by RhoB [256]. Since NFKB1 is a highly-scoring predicted target of miR-508-3p, overexpression of this miR may have a more significant effect on the invasion

behavior and physical properties of HEYA8 rather than OVCAR8 cells. We also observe that certain predicted miR targets are expressed at different levels in HEYA8 and OVCAR8 cells. For example, a predicted target of miR-130b-3p, ARHGAP12, has slightly lower levels in OVCAR8 than HEYA8 (Supplementary Material Figure 8a), therefore a reduction of ARHGAP12 levels by miR-130b-3p may result in more significant reduction of invasion in HEYA8 cells. In addition to the p53 mutation, OVCAR8 cells have a number of additional mutations than the HEYA8 cells, which could also result in phenotypic differences between the two cell lines [257]. Differences between HEYA8 and OVCAR8 with miR overexpression may also be related to the 10x greater fold-increase in levels of miR-508-3p and miR-130b-3p in HEYA8 than OVCAR8 cells. Both miR-508-3p and miR-130b-3p exhibit more significant effects on the invasion and mechanotype of HEYA8 cells than OVCAR8 cells. Further studies can provide deeper insight into the effects of tumor suppressor miRs on the behavior of different ovarian cancer cell types.

3.3 Conclusions

MiRs play central roles in regulating gene expression and cellular functions across a wide range of biological processes, from embryogenesis to stem cell differentiation to cancer. Here we dissect the role of single cell physical properties in cell invasive behavior following upregulation of tumor-suppressor miRs in two human ovarian cancer cell lines. We focus on a panel of five tumor-supressor miRs that are expressed at lower levels in later stages of human ovarian cancer and are more abundant in patients with improved survival [141,159,258,259]. The mechanome targets of these miRs that we have identified may be implicated in ovarian cancer progression and warrant further investigation.

Our results also deepen our understanding of how cell/nuclear size, deformability, and architecture of the actin cytoskeleton could have functional consequences in cancer invasion. For adhered cells, we find that cell invasive potential is strongly correlated with cellular and nuclear size, as well as F-actin levels. With overexpression of certain miRs, such as miR-508-3p in HEYA8 cells, our results show that cells become

less deformable and also less invasive. Thus, our findings also suggest that measurements of cell physical properties could complement existing methods to identify potential therapeutics.

Investigating other physical factors that are implicated in invasion may provide additional insights. Invasion is a complex and dynamic process in which cells remodel their local ECM by proteolytic degradation and by exerting traction forces on surrounding ECM fibers. An extensive network of structural and regulatory proteins are collectively responsible for actomyosin contractility and cell level dynamics [260]. Differences in cell contractility or the adhesive properties of cells could contribute to the differences in cell invasion that we observe in cells overexpressing tumor-suppressor miRs. Indeed, increased metastatic invasion is associated with higher traction stresses in breast, prostate, and lung cancer cells [261], and cell stiffening response is observed after contractile stimulation in airway smooth muscle cells [41]. In addition to changes in cell physical properties, the ECM also regulates invasion through its mechanical properties and density of cell adhesion binding sites [153,262–264]. Complementary analyses of cell and ECM physical parameters and/or combinations of parameters could thus provide stronger predictive power. Ultimately, knowledge of physical properties of tumor cells and their microenvironment could lead to new strategies to better target invasive cancer cells and to reduce metastatic spread.

3.4 Future investigation

Opportunities for targeted therapy of ovarian cancer

The recent wealth of genomic data obtained by molecular profiling has provided an opportunity to better match cancer treatments for specific subtypes of ovarian cancer. In addition, morphological and molecular studies reveal that ovarian cancer is not a single disease, but a collection of disease subtypes

with altering origins and significantly different clinical behaviors [265,266]. Although current clinical management of ovarian carcinoma largely neglects this heterogeneity, the four major histological subtypes of epithelial ovarian tumors (serous, endometrioid, clear cell, and mucinous) have characteristic genetic defects that deregulate specific signaling pathways in the tumor cells [267]**.** Alteration of the p53 gene has been extensively studied and is the most commonly described genetic alteration, present in about 50–70% of advanced-stage ovarian carcinomas [267,268]. However, the occurrence of p53 mutation in clear cell carcinoma is much less frequent than in other histologic subtypes [269]. Given that we have observed that cells with elevated levels of tumor-suppressor miRNAs have more pronounced effects of reduced invasion and decreased deformability in p53 wild-type HEYA8 cells compared to p53 mutant OVCAR8 cells, we suggest that the tumor-suppressor miRNAs may offer novel therapeutic opportunities in clear cell carcinoma and in patients with wild-type p53.

Delivery of functional microRNAs into cancer cells

Here we have used cell physical properties as a biomarker to validate the efficacy of miRNAs with tumor-suppressive effects. The involvement of miRNAs in the onset and progression of cancer has generated significant interest for therapeutic development. Depending on the expression status of the target miRNA, miRNA-based therapeutic approaches are separated into two classes: (1) miRNA inhibition therapy when the miRNA is overexpressed, and (2) miRNA replacement therapy to restore miRNA levels when miRNA expression and activity are repressed. In miRNA replacement therapy, oligonucleotides containing the same sequence as the mature endogenous miRNA, known as miRNA mimics, are used to supplement lowered levels of the miRNA. A miRNA mimic has the ability to enter the RNA-induced silencing complex (RISC) and affect the same target genes as the endogenous miRNA, through binding to partially complementary sequences in the 3′ untranslated regions of target mRNAs and induce their degradation or block their translation [270]; this can be achieved using a synthetic, single-stranded RNA molecule that

contains the same sequence as the mature endogenous miRNA. However, singled-stranded miRNA mimics tends to be 10^2–10^3-fold less potent compared with mimics that feature a second, passenger strand with a sequence that is complementary to the mature miRNA [271]. Therefore, double-stranded miRNA mimics are greatly preferred to single-stranded mimics.

While miRNA replacement therapy holds exciting potential, the design of appropriate carrier systems for delivery of functional miRNAs remains a critical hurdle for transition to clinical applications. Nonviral methods of miRNA delivery include lipid and polymeric nanoparticles to protect the miRNA from degradation and increase their half-life in circulation. These synthetic delivery systems have considerable advantages over viral vectors due to the control of their molecular composition, simplified manufacturing, modification and analysis, and relatively lower immunogenicity [272]. Liposomes are one of the most commonly used transfection reagents *in vitro*. However, their *in vivo* application is frequently limited by nonspecific uptake, unwanted immune response, and toxicity [273]. Polyethylenimine (PEI) is one of the most widely used polymer-based delivery systems, and both DNA and siRNA have been successfully delivered using PEI in animal models *in vivo* [272,274].

Inorganic nanoparticles represent another class of alternatives for miRNA delivery and have several advantages, including biocompatibility, controlled release of therapeutic agents, and capability of targeted drug delivery. Many types of materials for nanoparticles have been tested, including silica, calcium, magnesium, strontium, quantum dots [275]. Recently, our group has begun testing gold nanoparticles for the delivery of functional miRNAs into ovarian cancer cells. Gold nanoparticles (AuNPs) have received attention as model drug delivery platforms due to their amphiphilicity, biocompatibility, and advantageous surface characteristics that allow easy functionalization with chemical and biological molecules [276–278]. Nanoparticles can be used for various routes of administration including local injection, topical skin application, intravenous administration [279].

The complexity and heterogeneity of signaling pathways involved in many diseases contributes to the difficulty of developing effective medicine for cancer treatment. MiRNAs are currently being explored as potential drug therapeutics because of their ability to regulate a broad network of genes involved in different signaling pathways. At the same time however, the broad functionality of miRNAs and potential off-target effects can be a liability. Moreover, addition of artificial miRNAs brings the risk of saturation of RNA processing machinery and could cause unwanted side effects [280,281]. Most importantly, the expression level and function of miRNAs varies between disease stages [159,258,282]. This aspect of miRNA therapeutics is challenging because it requires both temporal and spatial control over the biodistribution of the miRNA.

Complementary methods to assess the efficacy of miRNA treatments at the single cell level could provide stronger predictive power. Exploiting the benefits of microfluidic techniques and MEMS devices for label-free assessment of cells could therefore facilitate high-throughput approaches for screening potential new cancer therapeutics. A more detailed understanding of the biological activity of miRNAs will be key to translation of this promising therapeutic class of molecules.

3.5 Supplementary material

Supplementary Note

While both PMF and transit time assays require cells to deform through a ~10 μm pore when driven by an external applied pressure, we observe only a moderate correlation (R = 0.61, p = 0.28) between retention and transit time. This modest correlation between such similar techniques could reflect differences in the readouts for the bulk versus single cell deformability assays. In the microfluidic transit time assay we probe the deformation of single cells through constricted channels over < 1 sec, while in PMF we measure how a population of cells deform through a porous membrane over tens of seconds. The modest correlation may also stem from differences in the interactions of cells with the polycarbonate membrane

filters of our PMF device and the PDMS walls of the microfluidic channels [78,113,137]. Despite these technical differences between mechanotyping methods, the results of both assays show good agreement.

(a)

Treatment	Median Cell Size	Coefficient of Variation	Kurtosis
SCR	20.6	0.2	-2.5
130b-3p	23.2	0.2	-2.8
509-5p	22.7	0.2	-3.0
509-3p	24.4	0.2	-2.9
508-5p	22.3	0.2	-3.2
508-3p	23.9	0.2	-3.3
Mock	21.7	0.2	-2.7

(b)

Treatment	Median Nuclear Size	Coefficient of Variation	Kurtosis
SCR	10.0	0.2	8.6
130b-3p	11.1	0.2	2.9
509-5p	11.1	0.2	2.3
509-3p	12.7	0.3	7.4
508-5p	11.1	0.2	10.9
508-3p	11.6	0.2	2.5
Mock	10.0	0.2	15.0

Supplementary Material Table 1. Cell and nuclear size after miRNA transfection.

(a) Summary of median cell size, (b) median nuclear size, coefficient of variation, and kurtosis for miR-treated HEYA8 cells, measured by flow cytometry imaging.

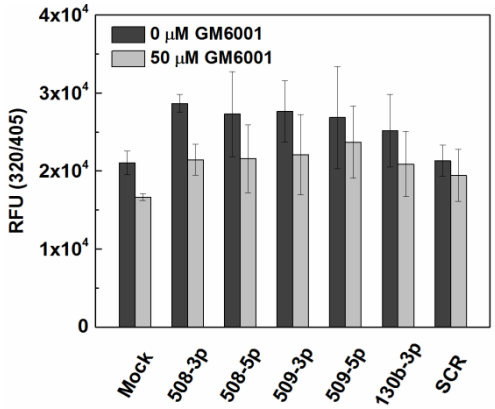

Supplementary Material Figure 1. Effect on protease activity after miRNA overexpression and treatment with the matrix

metalloproteinase inhibitor GM6001.

Quantification of protease activity in cell culture conditioned media measured using a fluorogenic peptide substrate (N=2). Relative fluorescence units (RFU) are obtained at 320 nm excitation and 405 nm emission. The background fluorescence is subtracted prior to quantification. Error bars represent standard deviations.

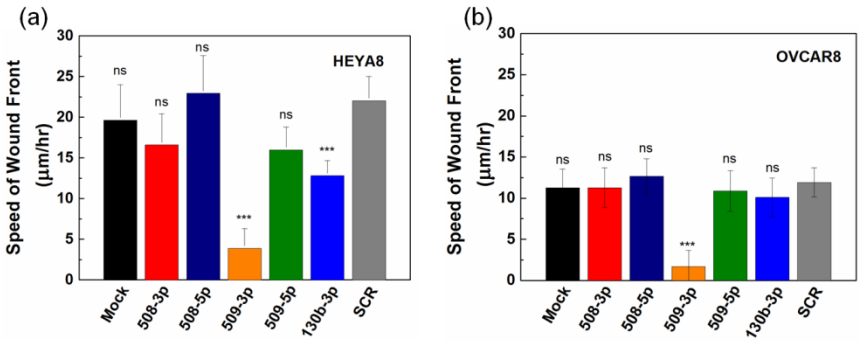

Supplementary Material Figure 2. Effect of miRNA overexpression on cell invasion speed through a collagen matrix.

Speed of the wound front (μm/hr) for HEYA8 and OVCAR8 cells, 10 hours after initiation of the scratch wound. The rate of invasion of the ovarian cancer cell lines HEYA8 (~20 μm/hr) and OVCAR8 (~10 μm/hr) is comparable to that of breast cancer cells. In a cell-derived matrix, MDA-MB-231 breast cancer cell migrate through 3D microenvironments at ~0.6 μm/min (~36 μm/hr) [283]. In Matrigel matrices, MDA-MB-231 breast cancer cells migrate at a velocity of ~20 μm/hr [284]. One-way ANOVA with a Tukey post hoc test, *** ($p < 0.001$), ns ($p > 0.05$), compared to the scrambled control treatment (SCR). Error bars show standard deviations from N=3 independent experiments.

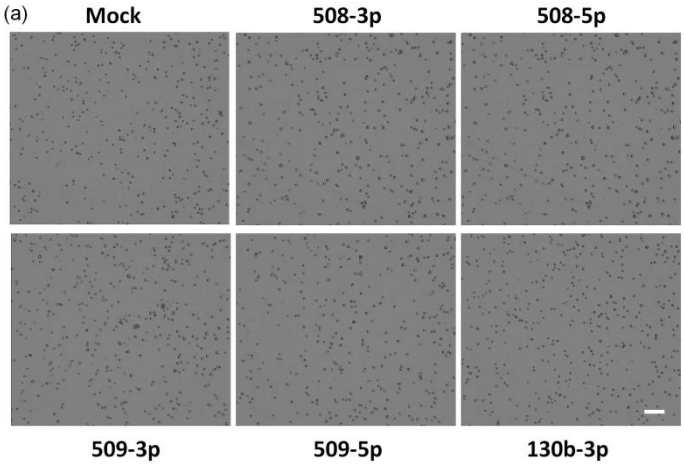

(b)

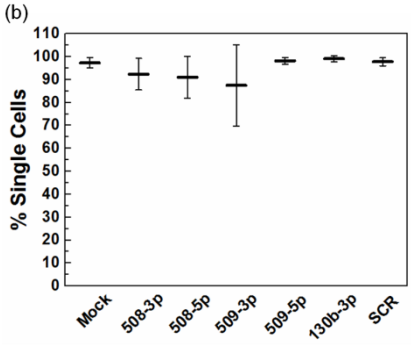

Treatment	% Single Cells
Mock	97.3 ± 2.2
miR-508-3p	92.4 ± 6.9
miR-508-5p	91.0 ± 9.1
miR-509-3p	87.5 ± 17.7
miR-509-5p	98.2 ± 1.4
miR-130b-3p	99.1 ± 1.3
SCR	97.8 ± 1.8

Supplementary Material Figure 3. Percentage of single HEYA8 cells in parallel microfiltration samples.

(a) Images of cell suspensions prior to loading samples into the parallel microfiltration device. Scale, 100 μm. (b) Percentage of single HEYA8 cells in parallel microfiltration samples. Here we identify single cells by manual inspection of the images. Error bars represent standard deviations (N=2).

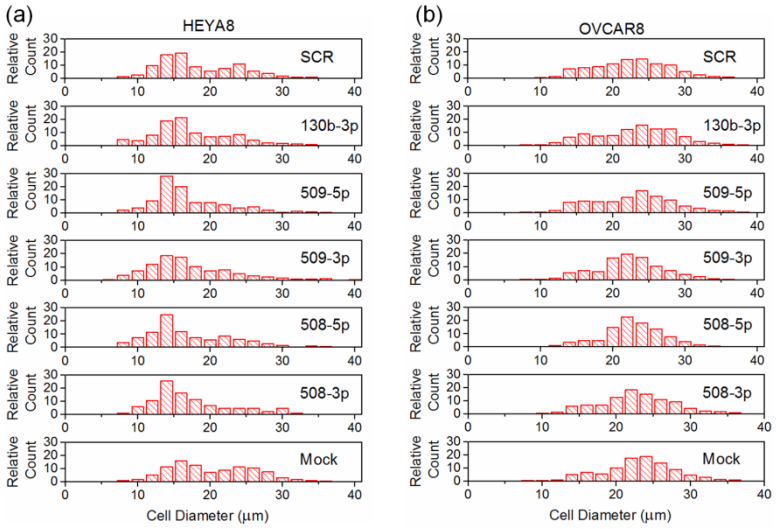

Supplementary Material Figure 4. Cell size after miR transfection.

Distribution of cell size for (a) HEYA8 and (b) OVCAR8 cells measured in a microfluidic device prior to entry into the first constriction. As upstream filters can retain cells of larger size, cells imaged in the microfluidic device may appear smaller than those imaged by flow cytometry. Data for 20 to 197 single cells over N=2 independent experiments.

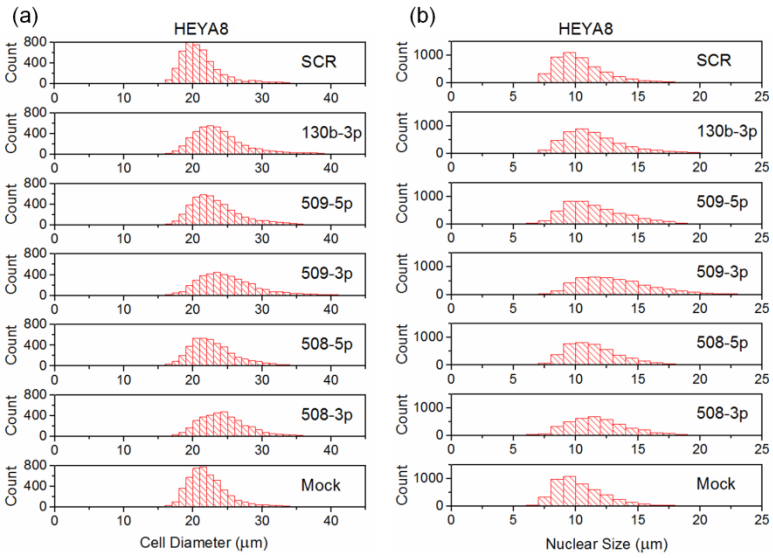

Supplementary Material Figure 5. Cell and nuclear size for HEYA8 after miR transfection.

Distribution of (a) cell size and (b) nuclear size measured by flow cytometry imaging. Data for at least 3991 single cells over N=3 independent experiments.

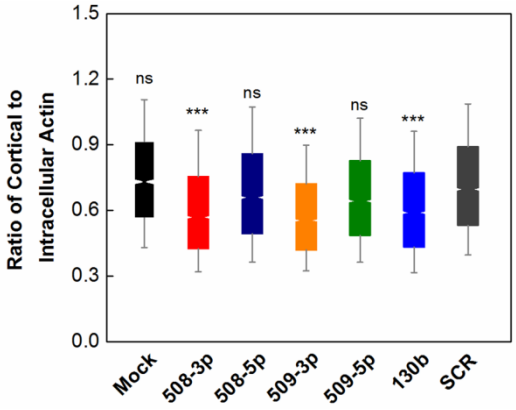

Supplementary Material Figure 6. Subcellular structures of cells in suspension as analyzed by flow cytometer imaging.

Quantification of the fluorescence intensity of cortical-to-intracellular F-actin. Data represents n>3991 single cells over N=3 independent experiments. Boxes denote the 25th and 75th percentiles, and whiskers denote the 10th and 90th percentiles. Notches represent the 95% confidence interval about the median. Mann-Whitney test, ns (not significant), *** ($p < 0.001$) compared to the SCR treatment.

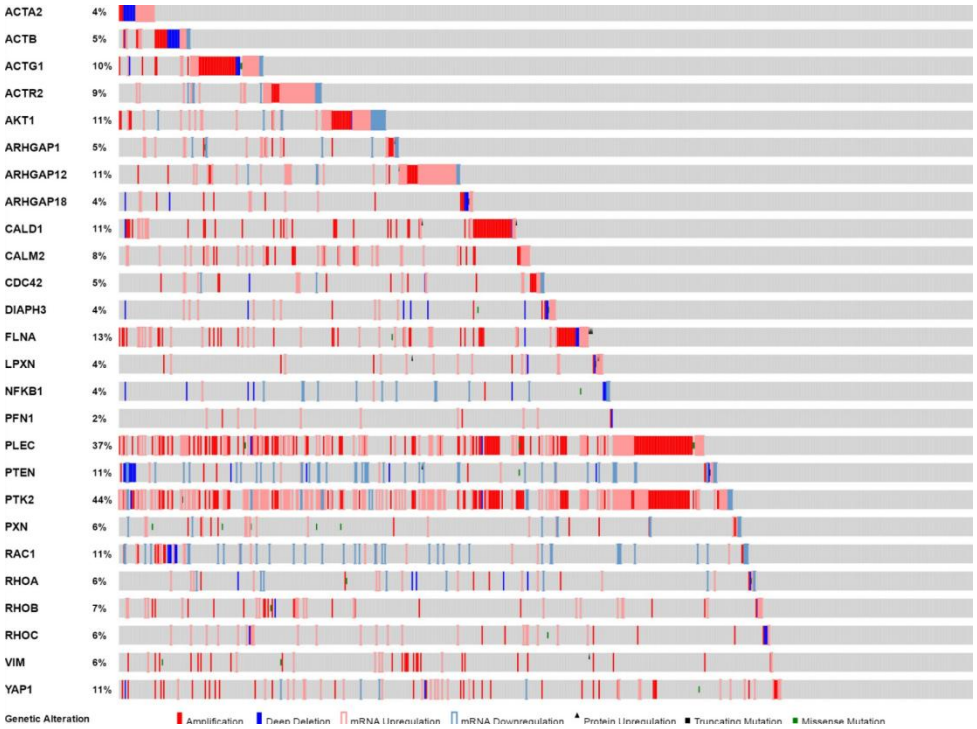

Supplementary Material Figure 7. Analysis of mechanome genes in TCGA ovarian cancer data using cBioPortal.

Graphical summary of genomic alterations in mechanome genes across a set of 603 tumor samples (Ovarian serious cystadenocarcinoma, TCGA Provisional, RNA Seq V2 RSEM) [240,241]. Rows represent genes, and columns represent samples. The legend below the graphic indicates the types of alterations.

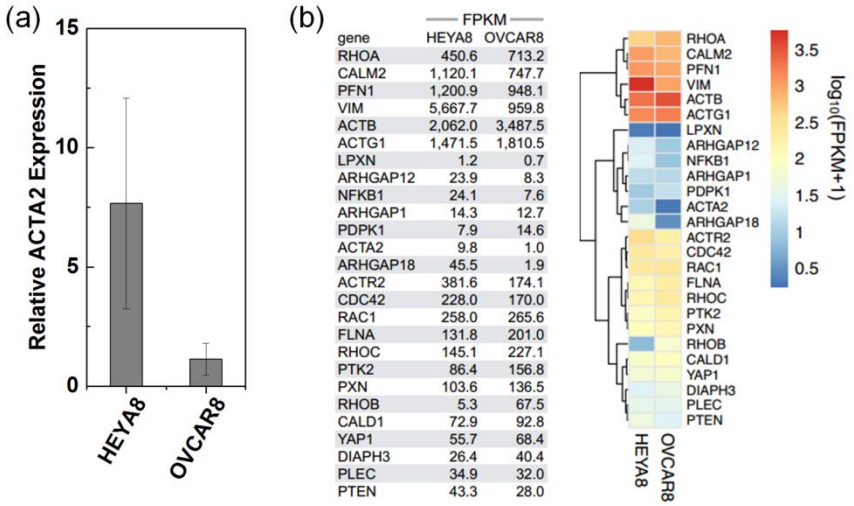

Supplementary Material Figure 8. Analysis of expression of mechanoregulating genes in OVCAR8 and HEYA8 cell lines.

(a) Quantification of relative expression as measured by qRT-PCR using the delta delta cycle time method (ΔΔCt) with 18S ribosomal RNA as an endogenous control. Error bars show standard deviations of N=3 independent experiments. (b) Comparison of mRNA levels using RNA-seq data from The Broad-Novartis Cancer Cell Line Encyclopedia (CCLE).

References

1. Sahai, E. 2007 Illuminating the metastatic process. *Nat. Rev. Cancer* **7**, 737–749. (doi:10.1038/nrc2229)

2. Kessenbrock, K., Plaks, V. & Werb, Z. 2010 Matrix Metalloproteinases: Regulators of the Tumor Microenvironment. *Cell* **141**, 52–67. (doi:10.1016/j.cell.2010.03.015)

3. Hanahan, D. & Weinberg, R. A. 2011 Hallmarks of cancer: The next generation. *Cell* **144**, 646–674. (doi:10.1016/j.cell.2011.02.013)

4. Larue, L. & Bellacosa, A. 2005 Epithelial-mesenchymal transition in development and cancer: role of phosphatidylinositol 3[prime] kinase//AKT pathways. *Oncogene* **24**, 7443–7454. (doi:1209091 [pii]10.1038/sj.onc.1209091)

5. Yilmaz, M. & Christofori, G. 2009 EMT , the cytoskeleton , and cancer cell invasion. , 15–33. (doi:10.1007/s10555-008-9169-0)

6. Creighton, C. J., Gibbons, D. L. & Kurie, J. M. 2013 The role of epithelial-mesenchymal transition programming in invasion and metastasis: A clinical perspective. *Cancer Manag. Res.* **5**, 187–195. (doi:10.2147/CMAR.S35171)

7. Kalluri, R. & Weinberg, R. a 2009 The basics of epithelial-mesenchymal transition. *J. Clin. Invest.* **119**, 1420–1428. (doi:10.1172/JCI39104.1420)

8. Lin, G. G. & Scott, J. G. 2013 A Brief Review of the Biophysical Hallmarks of Metastatic Cancer Cells. *Cancer Hallm.* **1**, 59–66. (doi:10.1016/j.pestbp.2011.02.012.Investigations)

9. Kumar, S., Maxwell, I. Z., Heisterkamp, A., Polte, T. R., Lele, T. P., Salanga, M., Mazur, E. & Ingber, D. E. 2006 Viscoelastic retraction of single living stress fibers and its impact on cell shape, cytoskeletal organization, and extracellular matrix mechanics. *Biophys. J.* **90**, 3762–3773. (doi:10.1529/biophysj.105.071506)

10. Reinhart-King, C. A., Dembo, M. & Hammer, D. A. 2005 The dynamics and mechanics of endothelial cell spreading. *Biophys. J.* **89**, 676–689. (doi:10.1529/biophysj.104.054320)

11. Fletcher, D. A. & Mullins, R. D. 2010 Cell mechanics and the cytoskeleton. *Nature* **463**, 485–492. (doi:10.1038/nature08908.Cell)

12. Even-Ram, S. & Yamada, K. M. 2005 Cell migration in 3D matrix. *Curr. Opin. Cell Biol.* **17**, 524–532. (doi:10.1016/j.ceb.2005.08.015)

13. Page-McCaw, A., Ewald, A. J. & Werb, Z. 2007 Matrix metalloproteinases and the regulation of tissue. *Nat Rev Mol Cell Biol.* **8**, 221–233. (doi:10.1038/nrm2125.Matrix)

14. Aung, A., Seo, Y. N., Lu, S., Wang, Y., Jamora, C., Del Álamo, J. C. & Varghese, S. 2014 3D Traction Stresses Activate Protease-Dependent Invasion of Cancer Cells. *Biophys. J.* **107**, 2528–2537. (doi:10.1016/j.bpj.2014.07.078)

15. Wolf, K. et al. 2013 Physical limits of cell migration: control by ECM space and nuclear deformation and tuning by proteolysis and traction force. *J. Cell Biol.* **201**, 1069–1084. (doi:10.1083/jcb.201210152)

16. Munevar, S., Wang, Y. L. & Dembo, M. 2001 Distinct roles of frontal and rear cell-substrate adhesions in fibroblast migration. *Mol. Biol. Cell* **12**, 3947–3954. (doi:11739792)

17. Dembo, M. & Wang, Y.-L. 1999 Stresses at the Cell-to-Substrate Interface during Locomotion of Fibroblasts. *Biophys. J.* **76**, 2307–2316. (doi:10.1016/S0006-3495(99)77386-8)

18. Rape, A., Guo, W. G. & Wang, Y. 2011 The Regulation of Traction Force in Relation to Cell Shape and Focal Adhesions. *Biomaterials* **32**, 2043–2051. (doi:10.1016/j.biomaterials.2010.11.044.The)

19. Balaban, N. Q. et al. 2001 Force and focal adhesion assembly: a close relationship studied using elastic micropatterned substrates. *Nat. Cell Biol.* **3**, 466–472. (doi:10.1038/35074532\n35074532 [pii])

20. Koch, T. M., Munster, S., Bonakdar, N., Butler, J. P. & Fabry, B. 2012 3D Traction Forces in Cancer Cell Invasion. *PLoS One* **7**, e33476. (doi:10.1371/Citation)

21. Friedl, P., Zanker, K. S. & Bröcker, E.-B. 1998 Cell Migration Strategies in 3D Extracellular Matrix: Differences in Morohology, Cell Matrix Interactions and Integrin Function. *Microsc. Res. Tech.* **43**, 369–378. (doi:10.1002/(SICI)1097-0029(19981201)43:5<369::AID-JEMT3>3.0.CO;2-6)

22. Lo, C.-M. et al. 2000 Cell Movement Is Guided by the Rigidity of the Substrate. *Biophys. J.* **79**, 144–152. (doi:10.1016/S0006-3495(00)76279-5)

23. Ghibaudo, M., Saez, A., Trichet, L., Xayaphoummine, A., Browaeys, J., Silberzan, P., Buguin, A. & Ladoux, B. 2008 Traction forces and rigidity sensing regulate cell functions. *Soft Matter* **4**, 1836. (doi:10.1039/b804103b)

24. Califano, J. P. & Reinhart-King, C. A. 2010 Substrate stiffness and cell area predict cellular traction stresses in single cells and cells in contact. *Cell. Mol. Bioeng.* **3**, 68–75. (doi:10.1007/s12195-010-0102-6)

25. Yamaguchi, H., Wyckoff, J. & Condeelis, J. 2005 Cell migration in tumors. *Curr. Opin. Cell Biol.* **17**, 559–564. (doi:10.1016/j.ceb.2005.08.002)

26. Sahai, E. 2005 Mechanisms of cancer cell invasion. *Curr. Opin. Genet. Dev.* **15**, 87–96. (doi:10.1016/j.gde.2004.12.002)

27. Friedl, P. & Wolf, K. 2003 Tumour-cell invasion and migration: diversity and escape mechanisms. *Nat. Rev. Cancer* **3**, 362–74. (doi:10.1038/nrc1075)

28. Kumar, S. & Weaver, V. M. 2009 Mechanics, malignancy, and metastasis: The force journey of a tumor cell. *Cancer Metastasis Rev.* **28**, 113–127. (doi:10.1007/s10555-008-9173-4.Mechanics)

29. Suresh, S. 2007 Biomechanics and biophysics of cancer cells. *Acta Biomater.* **3**, 413–38. (doi:10.1016/j.actbio.2007.04.002)

30. Xu, J., Tseng, Y. & Wirtz, D. 2000 Strain hardening of actin filament networks: Regulation by the dynamic cross-linking protein α-actinin. *J. Biol. Chem.* **275**, 35886–35892. (doi:10.1074/jbc.M002377200)

31. Mitchison, T. J. & Cramer, L. P. 1996 Actin-based cell motility and cell locomotion. *Cell* **84**, 371–379. (doi:10.1016/S0092-8674(00)81281-7)

32. Ridley, A. J., Schwartz, M. A., Burridge, K., Firtel, R. A., Ginsberg, M. H., Borisy, G., Parsons, J. T. & Horwitz, A. R. 2003 Cell migration: integrating signals from front to back. *Science* **302**, 1704–1709. (doi:10.1126/science.1092053)

33. Gardel, M. L., Shin, J. H., MacKintosh, F. C., Mahadevan, L., Matsudaira, P. & Weitz, D. A. 2004 Elastic Behavior of Cross-Linked and Bundled Actin Networks. *Science (80-.).* **304**, 1301–1305. (doi:10.1126/science.1095087)

34. Kasza, K. E., Koenderink, G. H., Lin, Y. C., Broedersz, C. P., Messner, W., Nakamura, F., Stossel, T. P., MacKintosh, F. C. & Weitz, D. A. 2009 Nonlinear elasticity of stiff biopolymers connected by flexible linkers. *Phys. Rev. E - Stat. Nonlinear, Soft Matter Phys.* **79**, 1–5. (doi:10.1103/PhysRevE.79.041928)

35. Murrell, M., Oakes, P. W., Lenz, M. & Gardel, M. L. 2015 Forcing cells into shape: the mechanics of actomyosin contractility. *Nat. Rev. Mol. Cell Biol.* **16**, 486–498. (doi:10.1038/nrm4012)

36. Bendix, P. M., Koenderink, G. H., Cuvelier, D., Dogic, Z., Koeleman, B. N., Brieher, W. M., Field, C. M., Mahadevan, L. & Weitz, D. A. 2008 A Quantitative Analysis of Contractility in Active Cytoskeletal Protein Networks. *Biophys. J.* **94**, 3126–3136. (doi:10.1529/biophysj.107.117960)

37. Reymann, A.-C., Boujemaa-Paterski, R., Martiel, J.-L., Guérin, C., Cao, W., Chin, H. F., Cruz, E. M. D. La, Théry, M. & Blanchoin, L. 2012 Actin Network Architecture Can Determine Myosin Motor Activity. *Science (80-.).* **336**, 1310–1314. (doi:10.1126/science.1221708)

38. Mader, C. C., Hinchcliffe, E. H. & Wang, Y. 2007 Probing cell shape regulation with patterned substratum: requirement of myosin II-mediated contractility. *Soft Matter* **3**, 357–363. (doi:10.1039/B606590B)

39. Hoffman, B. D., Massiera, G., Van Citters, K. M. & Crocker, J. C. 2006 The consensus mechanics of cultured mammalian cells. *Proc. Natl. Acad. Sci. U. S. A.* **103**, 10259–64. (doi:10.1073/pnas.0510348103)

40. Fabry, B., Maksym, G. N., Butler, J. P., Glogauer, M., Navajas, D. & Fredberg, J. J. 2001 Scaling the microrheology of living cells. *Phys. Rev. Lett.* **87**, 1–4. (doi:10.1103/PhysRevLett.87.148102)

41. Smith, B. A., Tolloczko, B., Martin, J. G. & Grütter, P. 2005 Probing the Viscoelastic Behavior of Cultured Airway Smooth Muscle Cells with Atomic Force Microscopy : Stiffening Induced by Contractile Agonist. **88**, 2994–3007. (doi:10.1529/biophysj.104.046649)

42. Van Citters, K. M., Hoffman, B. D., Massiera, G. & Crocker, J. C. 2006 The role of F-actin and myosin in epithelial cell rheology. *Biophys. J.* **91**, 3946–56. (doi:10.1529/biophysj.106.091264)

43. Laudadio, R. E., Millet, E. J., Fabry, B., An, S. S., Butler, J. P. & Fredberg, J. J. 2005 Rat airway smooth muscle cell during actin modulation: rheology and glassy dynamics. *Am. J. Physiol. Cell*

Physiol. **289**, C1388-1395. (doi:10.1152/ajpcell.00060.2005)

44. RE, S. & Edds, K. 1976 Microtubules: Structure, Chemistry, and Function. *Physiol. Rev.* **56**, 709–777.

45. Gittes, F., Mickey, B., Nettleton, J. & Howard, J. 1993 Flexural rigidity of microtubules and actin filaments measured from thermal fluctuations in shape. *J. Cell Biol.* **120**, 923–934. (doi:10.1083/jcb.120.4.923)

46. Kis, A., Kasas, S., Babić, B., Kulik, A. J., Benoît, W., Briggs, G. A. D., Schönenberger, C., Catsicas, S. & Forró, L. 2002 Nanomechanics of Microtubules. *Phys. Rev. Lett.* **89**, 248101. (doi:10.1103/PhysRevLett.89.248101)

47. Kurachi, M., Hoshi, M. & Tashiro, H. 1995 Buckling of a single microtubule by optical trapping forces: Direct measurement of microtubule rigidity. *Cell Motil. Cytoskeleton* **30**, 221–228. (doi:10.1002/cm.970300306)

48. Schaap, I. a T., Carrasco, C., de Pablo, P. J., MacKintosh, F. C. & Schmidt, C. F. 2006 Elastic response, buckling, and instability of microtubules under radial indentation. *Biophys. J.* **91**, 1521–1531. (doi:10.1529/biophysj.105.077826)

49. Venier, P., Maggs, A. C., Carlier, M. F. & Pantaloni, D. 1994 Analysis of microtubule rigidity using hydrodynamic flow and thermal fluctuations. *J. Biol. Chem.* **269**, 13353–13360.

50. Pampaloni, F., Lattanzi, G., Jonás, A., Surrey, T., Frey, E. & Florin, E.-L. 2006 Thermal fluctuations of grafted microtubules provide evidence of a length-dependent persistence length. *Proc. Natl. Acad. Sci. U. S. A.* **103**, 10248–10253. (doi:10.1073/pnas.0603931103)

51. Brown, R. A., Talas, G., Porter, R. A., McGrouther, D. A. & Eastwood, M. 1996 Balanced mechanical forces and microtubule contribution to fibroblast contraction. *J. Cell. Physiol.* **169**, 439–447. (doi:10.1002/(SICI)1097-4652(199612)169:3<439::AID-JCP4>3.0.CO;2-P)

52. Dogterom, M. & Bernard, Y. 1997 Measurement of the Force-Velocity Relation for Growing Microtubules. *Science (80-.).* **278**, 856–860. (doi:10.1126/science.278.5339.856)

53. Heidemann, S. R., Kaech, S., Buxbaum, R. E. & Matus, A. 1999 Direct Observations of the Mechanical Behaviors of the Cytoskeleton in Living Fibroblasts. *Cell* **145**, 109–122.

54. Mickey, B. & Howard, J. 1995 Rigidity of microtubules is increased by stabilizing agents. *J. Cell Biol.* **130**, 909–917. (doi:10.1083/jcb.130.4.909)

55. Ivaska, J., Pallari, H. M., Nevo, J. & Eriksson, J. E. 2007 Novel functions of vimentin in cell adhesion, migration, and signaling. *Exp. Cell Res.* **313**, 2050–2062. (doi:10.1016/j.yexcr.2007.03.040)

56. Sullivan, T., Escalante-Alcalde, D., Bhatt, H., Anver, M., Bhat, N., Nagashima, K., Stewart, C. L. & Burke, B. 1999 Loss of A-type lamin expression compromises nuclear envelope integrity leading to muscular dystrophy. *J. Cell Biol.* **147**, 913–20.

57. Dahl, K. N., Ribeiro, A. J. S. & Lammerding, J. 2008 Nuclear shape, mechanics, and mechanotransduction. *Circ. Res.* **102**, 1307–1318. (doi:10.1161/CIRCRESAHA.108.173989)

58. Chamcheu, J. C., Siddiqui, I. A., Syed, D. N., Adhami, V. M., Liovic, M. & Mukhtar, H. 2011 Keratin gene mutations in disorders of human skin and its appendages. *Arch. Biochem. Biophys.* **508**, 123–137. (doi:10.1016/j.abb.2010.12.019)

59. Méndez-López, I. & Worman, H. J. 2012 Inner nuclear membrane proteins: impact on human disease. *Chromosoma* **121**, 153–67. (doi:10.1007/s00412-012-0360-2)

60. Janmey, P. A., Euteneuer, U., Traub, P. & Schliwa, M. 1991 Viscoelastic properties of vimentin compared with other filamentous biopolymer networks. *J. Cell Biol.* **113**, 155–60.

61. Hochmuth, R. M. 2000 Micropipette aspiration of living cells. *J. Biomech.* **33**, 15–22.

62. Theret, D. P., Levesque, M. J., Sato, M., Nerem, R. M. & Wheeler, L. T. 1988 The application of a homogeneous half-space model in the analysis of endothelial cell micropipette measurements. *J. Biomech. Eng.* **110**, 190–199. (doi:10.1115/1.3108430)

63. Chien, S., Sung, K. L., Skalak, R., Usami, S. & Tözeren, A. 1978 Theoretical and experimental studies on viscoelastic properties of erythrocyte membrane. *Biophys. J.* **24**, 463–487. (doi:10.1016/S0006-3495(78)85395-8)

64. Dong, C., Skalak, R., Sung, K.-L. P., Schmid-Schönbein, G. W. & Chien, S. 1988 Passive Deformation Analysis of Human Leukocytes. *J. Biomech. Eng.* **110**, 27–36. (doi:10.1115/1.3108402)

65. Nash, G. B., O'Brien, E., Gordon-Smith, E. C. & Dormandy, J. A. 1989 Abnormalities in the mechanical properties of red blood cells caused by plasmodium falciparum. **74**, 855–861.

66. Ohashi, T., Ishii, Y., Ishikawa, Y., Matsumoto, T. & Sato, M. 2002 Experimental and numerical analyses of local mechanical properties measured by atomic force microscopy for sheared endothelial cells. *Biomed. Mater. Eng.* **12**, 319–327.

67. Domke, J., Dannöhl, S., Parak, W. J., Müller, O., Aicher, W. K. & Radmacher, M. 2000 Substrate dependent differences in morphology and elasticity of living osteoblasts investigated by atomic force microscopy. *Colloids Surfaces B Biointerfaces* **19**, 367–379. (doi:10.1016/S0927-7765(00)00145-4)

68. Collinsworth, A. M. Y. M., Zhang, S., Kraus, W. E., Truskey, G. A., Amy, M., Zhang, S., William, E. & Truskey, G. A. 2002 Apparent elastic modulus and hysteresis of skeletal muscle cells throughout differentiation. *Am. J. Physiol. Cell Physiol.* **281**, 1219–1227.

69. Jan H. Hoh, Jason P. Cleveland, Craig B. Prater, Jean-Paul Revel, and P. K. H. 1992 Quantized Adhesion Detected with the Atomic Force Microscope. *Society* , 4917–4918. (doi:10.1021/ja00038a075)

70. Heinz, W. F. & Hoh, J. H. 1999 Spatially resolved force spectroscopy of biological surfaces using the atomic force microscope. *Trends Biotechnol.* **17**, 143–150. (doi:10.1016/S0167-7799(99)01304-9)

71. Zhang, H. & Liu, K.-K. 2008 Optical tweezers for single cells. *J. R. Soc. Interface* **5**, 671–690. (doi:10.1098/rsif.2008.0052)

72. Guck, J., Ananthakrishnan, R., Mahmood, H., Moon, T. J., Cunningham, C. C. & Käs, J. 2001 The optical stretcher: a novel laser tool to micromanipulate cells. *Biophys. J.* **81**, 767–784. (doi:10.1016/S0006-3495(01)75740-2)

73. Roth, K. B., Neeves, K. B., Squier, J. & Marr, D. W. M. 2016 High-throughput linear optical stretcher for mechanical characterization of blood cells. *Cytom. Part A* **89**, 391–397. (doi:10.1002/cyto.a.22794)

74. Lautenschlager, F., Paschke, S., Schinkinger, S., Bruel, A., Beil, M. & Guck, J. 2009 The regulatory role of cell mechanics for migration of differentiating myeloid cells. *Proc Natl Acad Sci U S A* **106**, 15696–15701. (doi:10.1073/pnas.0811261106)

75. Remmerbach, T. W., Wottawah, F., Dietrich, J., Lincoln, B., Wittekind, C. & Guck, J. 2009 Oral cancer diagnosis by mechanical phenotyping. *Cancer Res.* **69**, 1728–32. (doi:10.1158/0008-5472.CAN-08-4073)

76. Guck, J. et al. 2005 Optical deformability as an inherent cell marker for testing malignant transformation and metastatic competence. *Biophys. J.* **88**, 3689–3698. (doi:10.1529/biophysj.104.045476)

77. Herricks, T., Antia, M. & Rathod, P. K. 2009 Deformability limits of Plasmodium falciparum-infected red blood cells. *Cell. Microbiol.* **11**, 1340–1353. (doi:10.1111/j.1462-5822.2009.01334.x)

78. Hou, H. W., Li, Q. S., Lee, G. Y. H., Kumar, A. P., Ong, C. N. & Lim, C. T. 2009 Deformability study of breast cancer cells using microfluidics. *Biomed. Microdevices* **11**, 557–564. (doi:10.1007/s10544-008-9262-8)

79. Bow, H., Pivkin, I. V, Diez-Silva, M., Goldfless, S. J., Dao, M., Niles, J. C., Suresh, S. & Han, J. 2011 A microfabricated deformability-based flow cytometer with application to malaria. *Lab Chip* **11**, 1065–1073. (doi:10.1039/c0lc00472c)

80. Gabriele, S., Versaevel, M., Preira, P. & Théodoly, O. 2010 A simple microfluidic method to select, isolate, and manipulate single-cells in mechanical and biochemical assays. *Lab Chip* **10**, 1459–1467. (doi:10.1039/c002257h)

81. Rowat, A. C. et al. 2013 Nuclear envelope composition determines the ability of neutrophil-type cells to passage through micron-scale constrictions. *J. Biol. Chem.* **288**, 8610–8618. (doi:10.1074/jbc.M112.441535)

82. Adamo, A., Sharei, A., Adamo, L., Lee, B., Mao, S. & Jensen, K. F. 2012 Microfluidics-based assessment of cell deformability. *Anal. Chem.* **84**, 6438–6443. (doi:10.1021/ac300264v)

83. Nyberg, K. D., Scott, M. B., Bruce, S. L., Gopinath, A. B., Bikos, D., Mason, T. G., Kim, J. W., Choi, H. S. & Rowat, A. C. 2016 The physical origins of transit time measurements for rapid, single cell mechanotyping. *Lab Chip* **16**, 3330–3339. (doi:10.1039/C6LC00169F)

84. Handayani, S., Chiu, D. T., Tjitra, E., Kuo, J. S. & Lampah, D. 2015 High Deformability of Plasmodium vivax – Infected Red Blood Cells under Microfluidic Conditions. *J. Infect. Dis.* **199**, 445–450. (doi:10.1086/596048.High)

85. Lee, S. S., Yim, Y., Ahn, K. H. & Lee, S. J. 2009 Extensional flow-based assessment of red blood

cell deformability using hyperbolic converging microchannel. *Biomed. Microdevices* **11**, 1021–1027. (doi:10.1007/s10544-009-9319-3)

86. Gossett, D. R., Tse, H. T. K., Lee, S. a, Ying, Y., Lindgren, A. G., Yang, O. O., Rao, J., Clark, A. T. & Di Carlo, D. 2012 Hydrodynamic stretching of single cells for large population mechanical phenotyping. *Proc. Natl. Acad. Sci. U. S. A.* **109**, 7630–5. (doi:10.1073/pnas.1200107109)

87. Agus, D. B. et al. 2013 A physical sciences network characterization of non-tumorigenic and metastatic cells. *Sci. Rep.* **3**, 1–12. (doi:10.1038/srep01449)

88. Tse, H. T. K. et al. 2013 Quantitative diagnosis of malignant pleural effusions by single-cell mechanophenotyping. *Sci. Transl. Med.* **5**, 212ra163. (doi:10.1126/scitranslmed.3006559)

89. Guolla, L., Bertrand, M., Haase, K. & Pelling, a. E. 2012 Force transduction and strain dynamics in actin stress fibres in response to nanonewton forces. *J. Cell Sci.* **125**, 603–613. (doi:10.1242/jcs.088302)

90. Haase, K. & Pelling, A. E. 2013 Resiliency of the plasma membrane and actin cortex to large-scale deformation. *Cytoskeleton* **70**, 494–514. (doi:10.1002/cm.21129)

91. Li, Q. S., Lee, G. Y. H., Ong, C. N. & Lim, C. T. 2008 AFM indentation study of breast cancer cells. *Biochem. Biophys. Res. Commun.* **374**, 609–13. (doi:10.1016/j.bbrc.2008.07.078)

92. Rotsch, C. & Radmacher, M. 2000 Drug-induced changes of cytoskeletal structure and mechanics in fibroblasts: an atomic force microscopy study. *Biophys. J.* **78**, 520–535. (doi:10.1016/S0006-3495(00)76614-8)

93. Nawaz, S., Sánchez, P., Bodensiek, K., Li, S., Simons, M. & Schaap, I. a T. 2012 Cell Visco-Elasticity Measured with AFM and Optical Trapping at Sub-Micrometer Deformations. *PLoS One* **7**, e45297. (doi:10.1371/journal.pone.0045297)

94. Ribeiro, A. J. S., Khanna, P., Sukumar, A., Dong, C. & Dahl, K. N. 2014 Nuclear Stiffening Inhibits Migration of Invasive Melanoma Cells. *Cell. Mol. Bioeng.* **7**, 544–551. (doi:10.1007/s12195-014-0358-3)

95. Davidson, P. M., Denais, C., Bakshi, M. C. & Lammerding, J. 2014 Nuclear Deformability Constitutes a Rate-Limiting Step During Cell Migration in 3-D Environments. *Cell. Mol. Bioeng.* **7**, 293–306. (doi:10.1007/s12195-014-0342-y)

96. Munevar, S., Wang, Y. & Dembo, M. 2001 Traction force microscopy of migrating normal and H-ras transformed 3T3 fibroblasts. *Biophys. J.* **80**, 1744–57. (doi:10.1016/S0006-3495(01)76145-0)

97. Sabass, B., Gardel, M. L., Waterman, C. M. & Schwarz, U. S. 2008 High resolution traction force microscopy based on experimental and computational advances. *Biophys. J.* **94**, 207–20. (doi:10.1529/biophysj.107.113670)

98. Li, B., Lin, M., Tang, Y., Wang, B. & Wang, J. H.-C. 2008 A novel functional assessment of the differentiation of micropatterned muscle cells. *J. Biomech.* **41**, 3349–3353. (doi:10.1016/j.jbiomech.2008.09.025.A)

99. Beningo, K. A., Dembo, M., Kaverina, I., Small, J. V. & Wang, Y. L. 2001 Nascent focal

adhesions are responsible for the generation of strong propulsive forces in migrating fibroblasts. *J. Cell Biol.* **153**, 881–887. (doi:10.1083/jcb.153.4.881)

100. Labouesse, C., Verkhovsky, A. B., Meister, J.-J., Gabella, C. & Vianay, B. 2015 Cell Shape Dynamics Reveal Balance of Elasticity and Contractility in Peripheral Arcs. *Biophys. J.* **108**, 2437–2447. (doi:10.1016/j.bpj.2015.04.005)

101. Lemmon, C. A., Sniadecki, N. J., Ruiz, S. A., Tan, J. L., Romer, L. H. & Chen, C. S. 2005 Shear force at the cell-matrix interface: enhanced analysis for microfabricated post array detectors. *Mech. Chem. Biosyst.* **2**, 1–16. (doi:10.1016/j.bbi.2008.05.010)

102. du Roure, O., Saez, A., Buguin, A., Austin, R. H., Chavrier, P., Silberzan, P. & Ladoux, B. 2005 Force mapping in epithelial cell migration. *Proc. Natl. Acad. Sci. U. S. A.* **102**, 2390–2395. (doi:10.1073/pnas.0408482102)

103. Jordan, M. A. & Wilson, L. 1998 Microtubules and actin filaments: Dynamic targets for cancer chemotherapy. *Curr. Opin. Cell Biol.* **10**, 123–130. (doi:10.1016/S0955-0674(98)80095-1)

104. Kavallaris, M. 2010 Microtubules and resistance to tubulin-binding agents. *Nat. Rev. Cancer* **10**, 194–204. (doi:10.1038/nrc2803)

105. Zhou, J. & Giannakakou, P. 2005 Targeting Microtubules for Cancer Chemotherapy. *Curr. Med. Chem. -Anti-Cancer Agents* **5**, 65–71. (doi:10.2174/1568011053352569)

106. Lam, W. a, Rosenbluth, M. J. & Fletcher, D. a 2007 Chemotherapy exposure increases leukemia cell stiffness. *Blood* **109**, 3505–8. (doi:10.1182/blood-2006-08-043570)

107. Jowhar, D., Wright, G., Samson, P. C., Wikswo, J. P. & Janetopoulos, C. 2010 Open access microfluidic device for the study of cell migration during chemotaxis. *Integr. Biol.* **2**, 648–658. (doi:10.1039/c0ib00110d)

108. Byun, S. et al. In press. Characterizing deformability and surface friction of cancer cells Submission PDF. **I**.

109. Rosenbluth, M. J., Lam, W. A. & Fletcher, D. A. 2008 Analyzing cell mechanics in hematologic diseases with microfluidic biophysical flow cytometry. *Lab Chip* **8**, 1062–1070. (doi:10.1039/b802931h)

110. Chen, J. et al. 2011 Classification of cell types using a microfluidic device for mechanical and electrical measurement on single cells. *Lab Chip* **11**, 3174–81. (doi:10.1039/c1lc20473d)

111. Hogg, J. C. 1987 Neutrophil kinetics and lung injury. *Physiol. Rev.* **67**, 1249–1295.

112. Yap, B. & Kamm, R. D. 2005 Cytoskeletal remodeling and cellular activation during deformation of neutrophils into narrow channels. *J. Appl. Physiol.* **99**, 2323–2330. (doi:10.1152/japplphysiol.00503.2005)

113. Byun, S., Son, S., Amodei, D., Cermak, N., Shaw, J., Ho, J. & Hecht, V. C. 2013 Characterizing deformability and surface friction of cancer cells. *Proc. Natl. Acad. Sci.* **110**, 7580–7585. (doi:10.1073/pnas.1218806110)

114. Qi, D., Hoelzle, D. & Rowat, A. 2012 Probing single cells using flow in microfluidic devices. *Eur. Phys. J. Spec. Top.* **204**, 85–101. (doi:10.1140/epjst/e2012-01554-x)

115. Dolla, J. C., Nahidb, H., Klejwab, N., Kwona, R., Coultharda, S. M., Petzolda, B., Goodmanc, M. B. & Pruitt, B. L. 2011 SU-8 force sensing pillar arrays for biological measurements. *Lab Chip* **4**, 1–14. (doi:10.1126/scisignal.2001449.Engineering)

116. Yang, S. & Saif, M. T. A. 2007 MEMS based force sensors for the study of indentation response of single living cells. *Sensors Actuators, A Phys.* **135**, 16–22. (doi:10.1016/j.sna.2006.05.019)

117. Gnerlich, M., Perry, S. F. & Tatic-Lucic, S. 2012 A submersible piezoresistive MEMS lateral force sensor for a diagnostic biomechanics platform. *Sensors Actuators A Phys.* **188**, 111–119. (doi:10.1016/j.sna.2012.05.033)

118. Marelli, M., Gadhari, N., Boero, G., Chiquet, M. & Brugger, J. 2014 Cell force measurements in 3D microfabricated environments based on compliant cantilevers. *Lab Chip* **14**, 286–93. (doi:10.1039/c3lc51021b)

119. Burg, T. P., Godin, M., Knudsen, S. M., Shen, W., Carlson, G., Foster, J. S., Babcock, K. & Manalis, S. R. 2007 Weighing of biomolecules, single cells and single nanoparticles in fluid. *Nature* **446**, 1066–1069. (doi:10.1038/nature05741)

120. Mukundan, V., Nelson, W. J. & Pruitt, B. L. 2013 Microactuator device for integrated measurement of epithelium mechanics. *Biomed. Microdevices* **15**, 117–23. (doi:10.1007/s10544-012-9693-0)

121. Dong, J. & Ferreira, P. M. 2009 Electrostatically actuated cantilever with SOI-MEMS parallel kinematic XY stage. *J. Microelectromechanical Syst.* **18**, 641–651. (doi:10.1109/JMEMS.2009.2020371)

122. Hoelzle, D. J., Chan, C. K., Scott, M. B., Lake, M. A. & Rowat, A. C. 2015 A large displacement, high frequency, underwater microelectromechanical systems actuator. *J. Appl. Phys.* **117**, 1–7. (doi:10.1063/1.4905385)

123. Abbas, A., Supiot, P., Mille, V., Guillochon, D. & Bocquet, B. 2009 Capillary microchannel fabrication using plasma polymerized TMDS for fluidic MEMS technology. *J. Micromechanics Microengineering* **19**, 45022. (doi:10.1088/0960-1317/19/4/045022)

124. Czaplewski, D. A., Ilic, B. R., Zalalutdinov, M., Olbricht, W. L., Zehnder, A. T., Craighead, H. G. & Michalske, T. A. 2004 A micromechanical flow sensor for microfluidic applications. *J. Microelectromechanical Syst.* **13**, 576–585. (doi:10.1109/JMEMS.2004.832179)

125. Knechtel, R. 2005 Glass frit bonding: An universal technology for wafer level encapsulation and packaging. *Microsyst. Technol.* **12**, 63–68. (doi:10.1007/s00542-005-0022-x)

126. Unger, M. A. 2000 Monolithic Microfabricated Valves and Pumps by Multilayer Soft Lithography. *Science (80-.).* **288**, 113–116. (doi:10.1126/science.288.5463.113)

127. Wu, H., Odom, T. W., Chiu, D. T. & Whitesides, G. M. 2003 Fabrication of complex three-dimensional microchannel systems in PDMS. *J. Am. Chem. Soc.* **125**, 554–559. (doi:10.1021/ja021045y)

128. Haubert, K. et al. 2006 PDMS bonding by means of a portable, low-cost corona system. *Lab Chip* **6**, 1548. (doi:10.1039/b610567j)

129. Berdichevsky, Y., Khandurina, J., Guttman, A. & Lo, Y. H. 2004 UV/ozone modification of poly(dimethylsiloxane) microfluidic channels. *Sensors Actuators, B Chem.* **97**, 402–408. (doi:10.1016/j.snb.2003.09.022)

130. Y, X. & Whitesides, G. M. 2015 Soft Lithography. *Annu. Rev. Mater. Sci.* , 1–33. (doi:10.1146/annurev.matsci.28.1.153)

131. Lee, J. N., Park, C. & Whitesides, G. M. 2003 Solvent Compatibility of Poly(dimethylsiloxane)-Based Microfluidic Devices. *Anal. Chem.* **75**, 6544–6554. (doi:10.1021/ac0346712)

132. Merkel, T. C., Bondar, V. I., Nagai, K., Freeman, B. D. & Pinnau, I. 2000 Gas sorption, diffusion, and permeation in poly(dimethylsiloxane). *J. Polym. Sci. Part B Polym. Phys.* **38**, 415–434. (doi:10.1002/(SICI)1099-0488(20000201)38:3<415::AID-POLB8>3.0.CO;2-Z)

133. Palchesko, R. N., Zhang, L., Sun, Y. & Feinberg, A. W. 2012 Development of Polydimethylsiloxane Substrates with Tunable Elastic Modulus to Study Cell Mechanobiology in Muscle and Nerve. *PLoS One* **7**. (doi:10.1371/journal.pone.0051499)

134. Wong, I. & Ho, C.-M. 2009 Surface molecular property modifications for poly(dimethylsiloxane) (PDMS) based microfluidic devices. *Microfluid. Nanofluidics* **7**, 291–306. (doi:10.1007/s10404-009-0443-4)

135. Anderson, R. R. et al. 2011 Transient deflection response in microcantilever array integrated with polydimethylsiloxane (PDMS) microfluidics. *Lab Chip* **11**, 2088–96. (doi:10.1039/c1lc20025a)

136. Hopcroft, M. A., Nix, W. D. & Kenny, T. W. 2010 What is the Young's modulus of silicon? *J. Microelectromechanical Syst.* **19**, 229–238. (doi:10.1109/JMEMS.2009.2039697)

137. Qi, D., Kaur Gill, N., Santiskulvong, C., Sifuentes, J., Dorigo, O., Rao, J., Taylor-Harding, B., Ruprecht Wiedemeyer, W. & Rowat, A. C. 2015 Screening cell mechanotype by parallel microfiltration. *Sci. Rep.* **5**, 17595. (doi:10.1038/srep17595)

138. Hoelzle, D. J., Varghese, B. A., Chan, C. K. & Rowat, A. C. 2014 A Microfluidic Technique to Probe Cell Deformability. *J. Vis. Exp.* **91**, e51474. (doi:10.3791/51474)

139. Siegel, R., Ma, J., Zou, Z. & Jemal, A. 2014 Cancer Statistics. **64**, 9–29. (doi:10.3322/caac.21208)

140. TCGA 2011 Integrated genomic analyses of ovarian carcinoma. *Nature* **474**, 609–615. (doi:10.1038/nature10166)

141. Pan, Y. et al. 2016 miR-509-3p is clinically significant and strongly attenuates cellular migration and multi-cellular spheroids in ovarian cancer. *Oncotarget* **7**, 25930–25948. (doi:10.18632/oncotarget.8412)

142. Yang, C., Cai, J., Wang, Q., Tang, H., Cao, J., Wu, L. & Wang, Z. 2012 Epigenetic silencing of miR-130b in ovarian cancer promotes the development of multidrug resistance by targeting colony-stimulating factor 1. *Gynecol. Oncol.* **124**, 325–334. (doi:10.1016/j.ygyno.2011.10.013)

143. Zhai, Q., Zhou, L., Zhao, C., Wan, J., Yu, Z., Guo, X., Qin, J., Chen, J. & Lu, R. 2012 Identification of miR-508-3p and miR-509-3p that are associated with cell invasiona and migration and involved in apoptosis of renal cell carcinoma. *Biochem. Biophys. Res. Commun.* **419**, 621–626. (doi:10.1016/j.bbrc.2012.02.060)

144. Yoon, S., Han, E., Choi, Y.-C., Kee, H., Jeong, Y., Yoon, J. & Baek, K. 2014 Inhibition of cell proliferation and migration by miR-509-3p that targets CDK2, Rac1, and PIK3C2A. *Mol. Cells* **37**, 314–321. (doi:10.14348/molcells.2014.2360)

145. Mierke, C. T. 2013 The role of focal adhesion kinase in the regulation of cellular mechanical properties. *Phys. Biol.* **10**, 1–21. (doi:10.1088/1478-3975/10/6/065005)

146. Lee, G. Y. H. & Lim, C. T. 2007 Biomechanics approaches to studying human diseases. *Trends Biotechnol.* **25**, 111–118. (doi:10.1016/j.tibtech.2007.01.005)

147. Mierke, C. T. 2013 Physical break-down of the classical view on cancer cell invasion and metastasis. *Eur. J. Cell Biol.* **92**, 89–104. (doi:10.1016/j.ejcb.2012.12.002)

148. Frantz, C., Stewart, K. M. & Weaver, V. M. 2010 The extracellular matrix at a glance. *J. Cell Sci.* **123**, 4195–4200. (doi:10.1242/jcs.023820)

149. Wolf, K. & Friedl, P. 2011 Extracellular matrix determinants of proteolytic and non-proteolytic cell migration. *Trends Cell Biol.* **21**, 736–744. (doi:10.1016/j.tcb.2011.09.006)

150. Weigelin, B., Bakker, G. & Friedl, P. 2012 Intravital third harmonic generation microscopy of collective melanoma cell invasion. *IntraVital* **1**, 32–43. (doi:10.4161/intv.21223)

151. Yurchenco, P. D. & Ruben, G. C. 1987 Basement-Membrane Structure Insitu - Evidence for Lateral Associations in the Type-Iv Collagen Network. *J. Cell Biol.* **105**, 2559–2568. (doi:10.1083/jcb.105.6.2559)

152. Lautscham, L. et al. 2015 Migration in Confined 3D Environments Is Determined by a Combination of Adhesiveness, Nuclear Volume, Contractility, and Cell Stiffness. **109**, 1–14. (doi:10.1016/j.bpj.2015.07.025)

153. Zaman, M. H. et al. 2006 Migration of tumor cells in 3D matrices is governed by matrix stiffness along with cell-matrix adhesion and proteolysis. *Proc. Natl. Acad. Sci. U. S. A.* **103**, 10889–10894. (doi:10.1073/pnas.0604460103)

154. Wolf, K., Mazo, I., Leung, H., Engelke, K., von Andrian, U. H., Deryugina, E. I., Strongin, A. Y., Bröcker, E.-B. & Friedl, P. 2003 Compensation mechanism in tumor cell migration: mesenchymal-amoeboid transition after blocking of pericellular proteolysis. *J. Cell Biol.* **160**, 267–77. (doi:10.1083/jcb.200209006)

155. Wolf, K., Wu, Y. I., Liu, Y., Geiger, J., Tam, E., Overall, C., Stack, M. S. & Friedl, P. 2007 Multi-step pericellular proteolysis controls the transition from individual to collective cancer cell invasion. *Nat. Cell Biol.* **9**, 893–904. (doi:10.1038/ncb1616)

156. Cross, S. E., Jin, Y.-S., Rao, J. & Gimzewski, J. K. 2007 Nanomechanical analysis of cells from cancer patients. *Nat. Nanotechnol.* **2**, 780–783. (doi:10.1038/nnano.2007.388)

157. Xu, W., Mezencev, R., Kim, B., Wang, L., McDonald, J. & Sulchek, T. 2012 Cell Stiffness Is a Biomarker of the Metastatic Potential of Ovarian Cancer Cells. *PLoS One* **7**, e46609. (doi:10.1371/journal.pone.0046609)

158. Swaminathan, V., Mythreye, K., O'Brien, E. T., Berchuck, A., Blobe, G. C. & Superfine, R. 2011 Mechanical stiffness grades metastatic potential in patient tumor cells and in cancer cell lines. *Cancer Res.* **71**, 5075–5080. (doi:10.1158/0008-5472.CAN-11-0247)

159. Yu, X. et al. 2013 MiRNA expression signature for potentially predicting the prognosis of ovarian serous carcinoma. *Tumour Biol.* **34**, 3501–3508. (doi:10.1007/s13277-013-0928-3)

160. Vang, S. et al. 2013 Identification of Ovarian Cancer Metastatic miRNAs. *PLoS One* **8**, e58226. (doi:10.1371/journal.pone.0058226)

161. Cho, A., Howell, V. M. & Colvin, E. K. 2015 The Extracellular Matrix in Epithelial Ovarian Cancer – A Piece of a Puzzle. *Front. Oncol.* **5**, 1–16. (doi:10.3389/fonc.2015.00245)

162. Hu, X., Li, D., Zhang, W., Zhou, J., Tang, B. & Li, L. 2012 Matrix metalloproteinase-9 expression correlates with prognosis and involved in ovarian cancer cell invasion. *Arch. Gynecol. Obstet.* **286**, 1537–1543. (doi:10.1007/s00404-012-2456-6)

163. Davidson, B., Goldberg, I., Gotlieb, W. H., Kopolovic, J., Ben-Baruch, G., Nesland, J. M., Berner, A., Bryne, M. & Reich, R. 1999 High levels of MMP-2, MMP-9, MT1-MMP and TIMP-2 mRNA correlate with poor survival in ovarian carcinoma. *Clin. Exp. Metastasis* **17**, 799–808.

164. Huang, S., Van Arsdall, M., Tedjarati, S., McCarty, M., Wu, W., Langley, R. & Fidler, I. J. 2002 Contributions of stromal metalloproteinase-9 to angiogenesis and growth of human ovarian carcinoma in mice. *J. Natl. Cancer Inst.* **94**, 1134–1142. (doi:10.1093/jnci/94.15.1134)

165. Sodek, K. L., Brown, T. J. & Ringuette, M. J. 2008 Collagen I but not Matrigel matrices provide an MMP-dependent barrier to ovarian cancer cell penetration. *BMC Cancer* **8**, 1–11. (doi:10.1186/1471-2407-8-223)

166. Miow, Q. H., Tan, T. Z., Ye, J., Lau, J. a, Yokomizo, T., Thiery, J. & Mori, S. 2015 Epithelial-mesenchymal status renders differential responses to cisplatin in ovarian cancer. *Oncogene* **34**, 1899–1907. (doi:10.1038/onc.2014.136)

167. Huang, T. et al. 2016 miR-508-3p concordantly silences NFKB1 and RELA to inactivate canonical NF-κB signaling in gastric carcinogenesis. *Mol. Cancer* **15**, 1–15. (doi:10.1186/s12943-016-0493-7)

168. Zhao, G. et al. 2013 MiR-130b is a prognostic marker and inhibits cell proliferation and invasion in pancreatic cancer through targeting STAT3. *PLoS One* **8**, e73803. (doi:10.1371/journal.pone.0073803)

169. Chan, C. J., Ekpenyong, A. E., Golfier, S., Li, W., Chalut, K. J., Otto, O., Elgeti, J., Guck, J. & Lautenschläger, F. 2015 Myosin II Activity Softens Cells in Suspension. *Biophys. J.* **108**, 1856–1869. (doi:10.1016/j.bpj.2015.03.009)

170. Lange, J. R., Steinwachs, J., Kolb, T., Lautscham, L. A., Harder, I., Whyte, G. & Fabry, B. 2015 Microconstriction Arrays for High-Throughput Quantitative Measurements of Cell Mechanical

Properties. *Biophys. J.* **109**, 26–34. (doi:10.1016/j.bpj.2015.05.029)

171. Wang, G., Mao, W., Byler, R., Patel, K., Henegar, C., Alexeev, A. & Sulchek, T. 2013 Stiffness Dependent Separation of Cells in a Microfluidic Device. *PLoS One* **8**, e75901. (doi:10.1371/journal.pone.0075901)

172. Fan, X. & Kurgan, L. 2014 Comprehensive overview and assessment of computational prediction of microRNA targets in animals. *Brief. Bioinform.* **16**, 780–794. (doi:10.1093/bib/bbu044)

173. Kustermans, G., El Mjiyad, N., Horion, J., Jacobs, N., Piette, J. & Legrand-Poels, S. 2008 Actin cytoskeleton differentially modulates NF-KB-mediated IL-8 expression in myelomonocytic cells. *Biochem. Pharmacol.* **76**, 1214–1228. (doi:10.1016/j.bcp.2008.08.017)

174. Nemeth, Z. H., Deitch, E. A., Davidson, M. T., Szabo, C., Vizi, E. S. & Hasko, G. 2004 Disruption of the actin cytoskeleton results in nuclear factor-kB activation and inflammatory mediator production in cultured human intestinal epithelial cells. *J. Cell. Physiol.* **200**, 71–81. (doi:10.1002/jcp.10477)

175. Becker-Weimann, S., Xiong, G., Furuta, S., Han, J., Kuhn, I., Akavia, U.-D., Pe'er, D., Bissell, M. J. & Xu, R. 2013 NFkB disrupts tissue polarity in 3D by preventing integration of microenvironmental signals. *Oncotarget* **4**, 2010–2020.

176. Dierks, S., Hardenberg, S. Von, Schmidt, T., Bremmer, F., Burfeind, P. & Kaulfuß, S. 2015 Leupaxin stimulates adhesion and migration of prostate cancer cells through modulation of the phosphorylation status of the actin-binding protein caldesmon. *Oncotarget* **6**, 13591–13606.

177. Chen, P. W. & Kroog, G. S. 2010 Leupaxin is similar to paxillin in focal adhesion targeting and tyrosine phosphorylation but has distinct roles in cell adhesion and spreading. *Cell Adhes. Migr.* **4**, 527–540. (doi:10.4161/cam.4.4.12399)

178. Pollard, T. D. 2007 Regulation of actin filament assembly by Arp2/3 complex and formins. *Annu. Rev. Biophys. Biomol. Struct.* **36**, 451–477. (doi:10.1146/annurev.biophys.35.040405.101936)

179. Porazinski, S., Wang, H., Asaoka, Y., Behrndt, M., Miyamoto, T. & Al., E. 2015 YAP is essential for tissue tension to ensure vertebrate 3D body shape. *Nature* **521**, 217–221. (doi:10.1530/ERC-14-0411.Persistent)

180. Chang, G. H. K., Lay, A. J., Ting, K. K. & Gamble, J. R. 2014 ARHGAP18: an endogenous inhibitor of angiogenesis, limiting tip formation and stabilizing junctions. *Small GTPases* **5**, e975002. (doi:10.4161/21541248.2014.975002)

181. Maeda, M. et al. 2011 ARHGAP18, a GTPase-activating protein for RhoA, controls cell shape, spreading, and motility. *Mol. Biol. Cell* **22**, 3840–3852. (doi:10.1091/mbc.E11-04-0364)

182. Sit, S.-T. & Manser, E. 2011 Rho GTPases and their role in organizing the actin cytoskeleton. *J. Cell Sci.* **124**, 679–683. (doi:10.1242/jcs.064964)

183. Vial, E., Sahai, E. & Marshall, C. J. 2003 ERK-MAPK signaling coordinately regulates activity of Rac1 and RhoA for tumor cell motility. *Cancer Cell* **4**, 67–79. (doi:10.1016/S1535-6108(03)00162-4)

184. Ridley, A. J. 2001 Rho GTPases and cell migration. *J Cell Sci* **114**, 2713–2722. (doi:10.1083/jcb.150.4.807)

185. Mack, N. A., Whalley, H. J., Castillo-Lluva, S. & Malliri, A. 2011 The diverse roles of Rac signaling in tumorigenesis. *Cell Cycle* **10**, 1571–1581. (doi:10.4161/cc.10.10.15612)

186. Ahn, Y. et al. 2012 ZEB1 drives prometastatic actin cytoskeletal remodeling by downregulating miR-34a expression. *J. Clin. Invest.* **122**, 3170–3183. (doi:10.1172/JCI63608DS1)

187. Mendez, M., Kojima, S. & Goldman, R. D. 2010 Vimentin induces changes in cell shape, motility, and adhesion during the epithelial to mesenchymal transition. *FASEB J.* **24**, 1838–1851. (doi:10.1096/fj.09-151639)

188. Liu, C., Lin, H., Tang, M. & Wang, Y. 2015 Vimentin contributes to epithelial-mesenchymal transition cancer cell mechanics by mediating cytoskeletal organization and focal adhesion maturation. *Oncotarget* **6**, 15966–15983. (doi:10.18632/oncotarget.3862)

189. Wang, N. & Stamenović, D. 2000 Contribution of intermediate filaments to cell stiffness, stiffening, and growth. *Am. J. Physiol. Cell Physiol.* **279**, C188–C194. (doi:10.1109/IEMBS.1999.802102)

190. Eckes, B. et al. 1998 Impaired mechanical stability, migration and contractile capacity in vimentin-deficient fibroblasts. *J. Cell Sci.* **111**, 1897–1907.

191. Wheeler, A. P. & Ridley, A. J. 2004 Why three Rho proteins? RhoA, RhoB, RhoC, and cell motility. *Exp. Cell Res.* **301**, 43–49. (doi:10.1016/j.yexcr.2004.08.012)

192. Ridley, A. J. 2013 RhoA, RhoB and RhoC have different roles in cancer cell migration. *J. Microsc.* **251**, 242–249. (doi:10.1111/jmi.12025)

193. Karlsson, R., Pedersen, E. D., Wang, Z. & Brakebusch, C. 2009 Rho GTPase function in tumorigenesis. *Biochim. Biophys. Acta* **1796**, 91–98. (doi:10.1016/j.bbcan.2009.03.003)

194. Wu, M., Wu, Z. F., Kumar-Sinha, C., Chinnaiyan, A. & Merajver, S. D. 2004 RhoC induces differential expression of genes involved in invasion and metastasis in MCF10A breast cells. *Breast Cancer Res. Treat.* **84**, 3–12. (doi:10.1023/B:BREA.0000018426.76893.21)

195. Yu, T., Cao, R., Li, S., Fu, M., Ren, L., Chen, W., Zhu, H., Zhan, Q. & Shi, R. 2015 MiR-130b plays an oncogenic role by repressing PTEN expression in esophageal squamous cell carcinoma cells. *BMC Cancer* **15**, 1–9. (doi:10.1186/s12885-015-1031-5)

196. Truong, L. D., Dryer, S. E., Hu, Z. & Xu, J. 2015 Loss of PTEN promotes podocyte cytoskeletal rearrangement, aggravating diabetic nephropathy Jamie. *J. Pathol.* **236**, 30–40. (doi:10.1002/path.4508.Loss)

197. Liliental, J., Moon, S. Y., Lesche, R., Mamillapalli, R., Li, D., Zheng, Y., Sun, H. & Wu, H. 2000 Genetic deletion of the Pten tumor suppressor gene promotes cell motility by activation of Rac1 and Cdc42 GTPases. *Curr. Biol.* **10**, 401–404. (doi:10.1016/S0960-9822(00)00417-6)

198. Romero, S., Le Clainche, C., Didry, D., Egile, C., Pantaloni, D. & Carlier, M. F. 2004 Formin is a processive motor that requires profilin to accelerate actin assembly and associated ATP hydrolysis.

Cell **119**, 419–429. (doi:10.1016/j.cell.2004.09.039)

199. Kovar, D. R., Harris, E. S., Mahaffy, R., Higgs, H. N. & Pollard, T. D. 2006 Control of the assembly of ATP- and ADP-actin by formins and profilin. *Cell* **124**, 423–435. (doi:10.1016/j.cell.2005.11.038)

200. Peng, J., Wallar, B. J., Flanders, A., Swiatek, P. J. & Alberts, A. S. 2003 Disruption of the Diaphanous-Related Formin Drf1 Gene Encoding mDia1 Reveals a Role for Drf3 as an Effector for Cdc42. *Curr. Biol.* **13**, 534–545. (doi:10.1016/S)

201. Stastna, J., Pan, X., Wang, H., Kollmannsperger, A., Kutscheidt, S., Lohmann, V., Grosse, R. & Fackler, O. T. 2012 Differing and isoform-specific roles for the formin DIAPH3 in plasma membrane blebbing and filopodia formation. *Cell Res.* **22**, 728–45. (doi:10.1038/cr.2011.202)

202. Campellone, K. G. & Welch, M. D. 2010 A Nucleator Arms Race: Cellular Control of Actin Assembly. *Nat. Rev. Mol. Cell Biol.* **11**, 237–251. (doi:10.1038/nrm2867.A)

203. Kühn, S. & Geyer, M. 2014 Formins as effector proteins of Rho GTPases. *Small GTPases* **5**, e29513. (doi:10.4161/sgtp.29513)

204. Nakamura, F., Hartwig, J. H., Stossel, T. P. & Szymanski, P. T. 2005 Ca2+ and calmodulin regulate the binding of filamin A to actin filaments. *J. Biol. Chem.* **280**, 32426–32433. (doi:10.1074/jbc.M502203200)

205. Ridley, A. J. & Hall, A. 1992 The small GTP-binding protein rho regulates the assembly of focal adhesions and actin stress fibers in response to growth factors. *Cell* **70**, 389–399. (doi:10.1016/0092-8674(92)90163-7)

206. Amano, M., Chihara, K., Kimura, K., Fukata, Y., Nakamura, N., Matsuura, Y. & Kaibuchi, K. 1997 Formation of Actin Stress Fibers and Focal Adhesions Enhanced by Rho-Kinase Formation of Actin Stress Fibers and Focal Adhesions Enhanced by Rho-Kinase. *Science* **275**, 1308–1311. (doi:10.1126/science.275.5304.1308)

207. Prendergast, G. C. 2001 Actin' up: RhoB in cancer and apoptosis. *Nat. Rev. Cancer* **1**, 162–168. (doi:10.1038/35101096)

208. Comer, K. A., Dennis, P. A., Armstrong, L., Catino, J. J., Kastan, M. B. & Kumar, C. C. 1998 Human smooth muscle alpha-actin gene is a transcriptional target of the p53 tumor suppressor protein. *Oncogene* **16**, 1299–1308. (doi:10.1038/sj.onc.1201645)

209. Rønnov-Jessen, L. & Petersen, O. W. 1996 A function for filamentous α-smooth muscle actin: Retardation of motility in fibroblasts. *J. Cell Biol.* **134**, 67–80. (doi:10.1083/jcb.134.1.67)

210. Sarrió, D., Rodriguez-Pinilla, S. M., Hardisson, D., Cano, A., Moreno-Bueno, G. & Palacios, J. 2008 Epithelial-mesenchymal transition in breast cancer relates to the basal-like phenotype. *Cancer Res.* **68**, 989–997. (doi:10.1158/0008-5472.CAN-07-2017)

211. Lee, H. W. et al. 2013 Alpha-smooth muscle actin (ACTA2) is required for metastatic potential of human lung adenocarcinoma. *Clin. Cancer Res.* **19**, 5879–5889. (doi:10.1158/1078-0432.CCR-13-1181)

212. Peckham, M., Miller, G., Wells, C., Zicha, D. & Dunn, G. A. 2001 Specific changes to the mechanism of cell locomotion induced by overexpression of (β)-actin. *J. Cell Sci.* **114**, 1367–1377.

213. Dugina, V., Zwaenepoel, I., Gabbiani, G., Clément, S. & Chaponnier, C. 2009 Beta and gamma-cytoplasmic actins display distinct distribution and functional diversity. *J. Cell Sci.* **122**, 2980–2988. (doi:10.1242/jcs.041970)

214. Guo, M., Ehrlicher, A. J., Mahammad, S., Fabich, H., Jensen, M. H., Moore, J. R., Fredberg, J. J., Goldman, R. D. & Weitz, D. A. 2013 The role of vimentin intermediate filaments in cortical and cytoplasmic mechanics. *Biophys. J.* **105**, 1562–1568. (doi:10.1016/j.bpj.2013.08.037)

215. Wiche, G. & Winter, L. 2011 Plectin isoforms as organizers of intermediate filament cytoarchitecture. *Bioarchitecture* **1**, 14–20. (doi:10.4161/bioa.1.1.14630)

216. Wiche, G. 1998 Role of plectin in cytoskeleton organization and dynamics. *J. Cell Sci.* **111**, 2477–2486. (doi:10.1096/fj.08-124453)

217. Svitkina, T. M., Verkhovsky, A. B. & Borisy, G. G. 1996 Plectin sidearms mediate interaction of intermediate filaments with microtubules and other components of the cytoskeleton. *J. Cell Biol.* **135**, 991–1007. (doi:10.1083/jcb.135.4.991)

218. Aragona, M., Panciera, T., Manfrin, A., Giulitti, S., Michielin, F., Elvassore, N., Dupont, S. & Piccolo, S. 2013 A mechanical checkpoint controls multicellular growth through YAP/TAZ regulation by actin-processing factors. *Cell* **154**, 1047–1059. (doi:10.1016/j.cell.2013.07.042)

219. Wada, K.-I., Itoga, K., Okano, T., Yonemura, S. & Sasaki, H. 2011 Hippo pathway regulation by cell morphology and stress fibers. *Development* **138**, 3907–3914. (doi:10.1242/dev.070987)

220. Dupont, S. et al. 2011 Role of YAP/TAZ in mechanotransduction. *Nature* **474**, 179–185. (doi:10.1038/nature10137)

221. Piccolo, S., Dupont, S. & Cordenonsi, M. 2014 The Biology of YAP/TAZ: Hippo Signaling and Beyond. *Physiol. Rev.* **94**, 1287–1312. (doi:10.1152/physrev.00005.2014)

222. Driscoll, T. P., Cosgrove, B. D., Heo, S.-J., Shurden, Z. E. & Mauck, R. L. 2015 Cytoskeletal to Nuclear Strain Transfer Regulates YAP Signaling in Mesenchymal Stem Cells. *Biophys. J.* **108**, 2783–2793. (doi:10.1016/j.bpj.2015.05.010)

223. Ketene, A. N., Roberts, P. C., Shea, A. A., Schmelz, E. M. & Agah, M. 2012 Actin filaments play a primary role for structural integrity and viscoelastic response in cells. *Integr. Biol.* **4**, 540–549. (doi:10.1039/c2ib00168c)

224. Perrin, B. J. & Ervasti, J. M. 2010 The actin gene family: Function follows isoform. *Cytoskeleton* **67**, 630–634. (doi:10.1002/cm.20475)

225. Gardel, M. L., Schneider, I. C., Aratyn-Schaus, Y. & Waterman, C. M. 2010 Mechanical integration of actin and adhesion dynamics in cell migration. *Annu. Rev. Cell Dev. Biol.* **26**, 315–333. (doi:10.1146/annurev.cellbio.011209.122036)

226. Wirtz, D., Konstantopoulos, K. & Searson, P. P. C. 2011 The physics of cancer: the role of physical interactions and mechanical forces in metastasis. *Nat. Rev. Cancer* **11**, 512–522.

(doi:10.1038/nrc3080.The)

227. Tsai, M. A., Waugh, R. E. & Keng, P. C. 1998 Passive mechanical behavior of human neutrophils: effects of colchicine and paclitaxel. *Biophys. J.* **74**, 3282–3291. (doi:10.1016/S0006-3495(98)78035-X)

228. Pedersen, S. ., Hoffmann, E. . & Mills, J. . 2001 The cytoskeleton and cell volume regulation. *Comp. Biochem. Physiol. Part A* **130**, 385–399. (doi:10.1016/S1095-6433(01)00429-9)

229. Papakonstanti, E. A., Vardaki, E. A. & Stournaras, C. 2000 Actin Cytoskeleton : A Signaling Sensor in Cell Volume Regulation. *Cell. Physiol. Biochem.* **10**, 257–264. (doi:16366)

230. Fu, Y., Chin, L. K., Bourouina, T., Liu, A. Q. & VanDongen, A. M. J. 2012 Nuclear deformation during breast cancer cell transmigration. *Lab Chip* **12**, 3774–3778. (doi:10.1039/c2lc40477j)

231. Denais, C. M., Gilbert, R. M., Isermann, Philipp McGregor, Alexandra L. Lindert, M. te, Weigelin, B., Davidson, P., Friedl, P., Wolf, K. & Lammerding, J. 2016 Nuclear envelope rupture and repair during cancer cell migration. *Science* **352**, 353–358. (doi:10.1126/science.aad7297)

232. Icard-Arcizet, D., Cardoso, O., Richert, A. & Hénon, S. 2008 Cell stiffening in response to external stress is correlated to actin recruitment. *Biophys. J.* **94**, 2906–2913. (doi:10.1529/biophysj.107.118265)

233. Verschueren, H., Van der Taelen, I., Dewit, J., De Braekeleer, J. & De Baetselier, P. 1994 Metastatic competence of BW5147 T-lymphoma cell lines is correlated with in vitro invasiveness, motility and F-actin content. *J. Leukoc. Biol.* **55**, 552–556.

234. Katsantonis, J., Tosca, A., Koukouritaki, S. B., Theodoropoulos, P. A., Gravanis, A. & Stournaras, C. 1994 Differences in the G/total actin ratio and microfilament stability between normal and malignant human keratinocytes. *Cell Biochem. Funct.* **12**, 267–274. (doi:10.1002/cbf.290120407)

235. Nürnberg, A., Kitzing, T. & Grosse, R. 2011 Nucleating actin for invasion. *Nat. Rev. Cancer* **11**, 177–187. (doi:10.1038/nrc3003)

236. Reichl, E. M. et al. 2008 Interactions between Myosin and Actin Crosslinkers Control Cytokinesis Contractility Dynamics and Mechanics. *Curr. Biol.* **18**, 471–480. (doi:10.1016/j.cub.2008.02.056)

237. Parsons, J. T., Horwitz, A. R. & Schwartz, M. A. 2010 Cell adhesion: integrating cytoskeletal dynamics and cellular tension. *Nat. Rev. Mol. Cell Biol.* **11**, 633–643. (doi:10.1038/nrm2957)

238. Yamaguchi, H. & Condeelis, J. 2007 Regulation of the actin cytoskeleton in cancer cell migration and invasion. *Biochim. Biophys. Acta* **1773**, 642–652. (doi:10.1016/j.bbamcr.2006.07.001)

239. Petropoulos, C. et al. 2016 Roles of paxillin family members in adhesion and ECM degradation coupling at invadosomes. *J. Cell Biol.* **213**, 585–599. (doi:10.1083/jcb.201510036)

240. Gao, J. et al. 2010 Integrative Analysis of Complex Cancer Genomics and Clinical Profiles Using the cBioPortal. *Sci. Signal.* **6**, pl1. (doi:10.1097/MPG.0b013e3181a15ae8.Screening)

241. Cerami, E. et al. 2012 The cBio Cancer Genomics Portal: An open platform for exploring multidimensional cancer genomics data. *Cancer Discov.* **2**, 401–404. (doi:10.1158/2159-8290.CD-

12-0095)

242. Gen, Y. et al. 2009 A novel amplification target, ARHGAP5, promotes cell spreading and migration by negatively regulating RhoA in Huh-7 hepatocellular carcinoma cells. *Cancer Lett.* **275**, 27–34. (doi:10.1016/j.canlet.2008.09.036)

243. Wong, C., Yam, J. W., Ching, Y., Yau, T., Leung, T. H., Jin, D. & Ng, I. O. 2005 Rho GTPase-Activating Protein Deleted in Liver Cancer Suppresses Cell Proliferation and Invasion in Hepatocellular Carcinoma. *Cancer Res.* **65**, 8861–8868. (doi:10.1158/0008-5472.CAN-05-1318)

244. Wang, J. et al. 2014 ArhGAP30 promotes p53 acetylation and function in colorectal cancer. *Nat. Commun.* **5**, 4735. (doi:10.1038/ncomms5735)

245. Luo, N., Guo, J., Chen, L., Yang, W., Qu, X. & Cheng, Z. 2016 ARHGAP10, downregulated in ovarian cancer, suppresses tumorigenicity of ovarian cancer cells. *Cell Death Dis.* **7**, e2157. (doi:10.1038/cddis.2015.401)

246. Fingleton, B. 2007 Molecular targets in metastasis: Lessons from genomic approaches. *Cancer Genomics and Proteomics* **4**, 211–222.

247. Ueno, K., Hirata, H., Majid, S., Yamamura, S., Shahryari, V., Tabatabai, Z. L., Hinoda, Y. & Dahiya, R. 2012 Tumor suppressor microRNA-493 decreases cell motility and migration ability in human bladder cancer cells by downregulating RhoC and FZD4. *Mol. Cancer Ther.* **11**, 244–253. (doi:10.1158/1535-7163.MCT-11-0592)

248. Jiang, L., Liu, X., Kolokythas, A., Yu, J., Wang, A., Heidbreder, C. E., Shi, F. & Zhou, X. 2010 Down-regulation of the Rho GTPase signaling pathway is involved in the microRNA-138 mediated inhibition of cell migration and invasion in tongue squamous cell carcinoma. *Int. J. cancer* **127**, 505–512. (doi:10.1002/ijc.25320.Down-regulation)

249. Morley, S. et al. 2015 Regulation of microtubule dynamics by DIAPH3 influences amoeboid tumor cell mechanics and sensitivity to taxanes. *Sci. Rep.* **5**, 1–16. (doi:10.1038/srep12136)

250. DeWard, A. D. & Alberts, A. S. 2009 Ubiquitin-mediated degradation of the formin mDia2 upon completion of cell division. *J. Biol. Chem.* **284**, 20061–20069. (doi:10.1074/jbc.M109.000885)

251. Creekmore, A. L., Silkworth, W. T., Cimini, D., Jensen, R. V, Roberts, P. C. & Schmelz, E. M. 2011 Changes in gene expression and cellular architecture in an ovarian cancer progression model. *PLoS One* **6**, e17676. (doi:10.1371/journal.pone.0017676)

252. Pettee, K. M., Dvorak, K. M., Nestor-Kalinoski, A. L. & Eisenmann, K. M. 2014 An mDia2/ROCK signaling axis regulates invasive egress from epithelial ovarian cancer spheroids. *PLoS One* **9**. (doi:10.1371/journal.pone.0090371)

253. Calvo, F. et al. 2013 Mechanotransduction and YAP-dependent matrix remodelling is required for the generation and maintenance of cancer-associated fibroblasts. *Nat Cell Biol* **15**, 637–646. (doi:10.1038/ncb2756)

254. Secchiero, P., Rimondi, E., di Iasio, M. G., Voltan, R., Gonelli, A. & Zauli, G. 2012 Activation of the p53 pathway induces α-smooth muscle actin expression in both myeloid leukemic cells and normal macrophages. *J. Cell. Physiol.* **227**, 1829–1837. (doi:10.1002/jcp.22910)

255. Barretina, J. et al. 2012 The Cancer Cell Line Encyclopedia enables predictive modelling of anticancer drug sensitivity. *Nature* **483**, 603–607. (doi:10.1038/nature11003)

256. Fritz, G. & Kaina, B. 2001 Ras-related GTPase RhoB Represses NF-kB Signaling. *J. Biol. Chem.* **276**, 3115–3122. (doi:10.1074/jbc.M005058200)

257. Domcke, S., Sinha, R., Levine, D. a, Sander, C. & Schultz, N. 2013 Evaluating cell lines as tumour models by comparison of genomic profiles. *Nat. Commun.* **4**, 1–10. (doi:10.1038/ncomms3126)

258. Eitan, R. et al. 2009 Tumor microRNA expression patterns associated with resistance to platinum based chemotherapy and survival in ovarian cancer patients. *Gynecol. Oncol.* **114**, 253–259. (doi:10.1016/j.ygyno.2009.04.024)

259. Vilming Elgaaen, B., Olstad, O. K., Haug, K. B. F., Brusletto, B., Sandvik, L., Staff, A. C., Gautvik, K. M. & Davidson, B. 2014 Global miRNA expression analysis of serous and clear cell ovarian carcinomas identifies differentially expressed miRNAs including miR-200c-3p as a prognostic marker. *BMC Cancer* **14**, 80. (doi:10.1186/1471-2407-14-80)

260. Zaidel-Bar, R., Zhenhuan, G. & Luxenburg, C. 2015 The contractome - a systems view of actomyosin contractility in non-muscle cells. *J. Cell Sci.* **128**, 1–9. (doi:10.1242/jcs.170068)

261. Kraning-Rush, C. M., Califano, J. P. & Reinhart-King, C. a 2012 Cellular traction stresses increase with increasing metastatic potential. *PLoS One* **7**, e32572. (doi:10.1371/journal.pone.0032572)

262. Chaudhuri, O., Koshy, S. T., Branco da Cunha, C., Shin, J., Verbeke, C. S., Allison, K. H. & Mooney, D. J. 2014 Extracellular matrix stiffness and composition jointly regulate the induction of malignant phenotypes in mammary epithelium. *Nat. Mater.* **13**, 1–35. (doi:10.1038/nmat4009)

263. Gu, Z., Liu, F., Tonkova, E. A., Lee, S. Y., Tschumperlin, D. J. & Brenner, M. B. 2014 Soft matrix is a natural stimulator for cellular invasiveness. *Mol. Biol. Cell* **25**, 457–469. (doi:10.1091/mbc.E13-05-0260)

264. Guzman, A., Ziperstein, M. J. & Kaufman, L. J. 2014 The effect of fibrillar matrix architecture on tumor cell invasion of physically challenging environments. *Biomaterials* **35**, 6954–6963. (doi:10.1016/j.biomaterials.2014.04.086)

265. Ricciardelli, C. & Oehler, M. K. 2009 Diverse molecular pathways in ovarian cancer and their clinical significance. *Maturitas* **62**, 270–275. (doi:10.1016/j.maturitas.2009.01.001)

266. Kurman, R. & Shih, I. 2010 The Origin and pathogenesis of epithelial ovarian cancer-a proposed unifying theory. *Am. J. Surg. Pathol.* **34**, 433–443. (doi:10.1097/PAS.0b013e3181cf3d79.The)

267. Cho, K. & Shih, L. 2009 Ovarian Cancer. *Annu Rev Pathol* **1**, 287–313. (doi:10.1146/annurev.pathol.4.110807.092246.OVARIAN)

268. Kupryjańczyk, J., Thor, a D., Beauchamp, R., Merritt, V., Edgerton, S. M., Bell, D. a & Yandell, D. W. 1993 P53 Gene Mutations and Protein Accumulation in Human Ovarian Cancer. *Proc. Natl. Acad. Sci. U. S. A.* **90**, 4961–4965. (doi:10.1073/pnas.90.11.4961)

269. Ho, E. S., Lai, C. R., Hsieh, Y. T., Chen, J. T., Lin, a J., Hung, M. H. & Liu, F. S. 2001 P53

Mutation Is Infrequent in Clear Cell Carcinoma of the Ovary. *Gynecol. Oncol.* **80**, 189–93. (doi:10.1006/gyno.2000.6025)

270. Carthew, Richard W. and Sontheimer, E. J. 2009 Origins and Mechanisms of miRNAs and siRNAs. *Cell* **136**, 642–655. (doi:10.1016/j.cell.2009.01.035.Origins)

271. Bader, A. G., Brown, D. & Winkler, M. 2010 The promise of microRNA replacement therapy. *Cancer Res.* **70**, 7027–30. (doi:10.1158/0008-5472.CAN-10-2010)

272. Park, T. G., Jeong, J. H. & Kim, S. W. 2006 Current status of polymeric gene delivery systems. *Adv. Drug Deliv. Rev.* **58**, 467–486. (doi:10.1016/j.addr.2006.03.007)

273. Lv, H., Zhang, S., Wang, B., Cui, S. & Yan, J. 2006 Toxicity of cationic lipids and cationic polymers in gene delivery. *J. Control. Release* **114**, 100–109. (doi:10.1016/j.jconrel.2006.04.014)

274. Ibrahim, A. F., Weirauch, U., Thomas, M., Gruñweller, A., Hartmann, R. K. & Aigner, A. 2011 MicroRNA replacement therapy for miR-145 and miR-33a is efficacious in a model of colon carcinoma. *Cancer Res.* **71**, 5214–5224. (doi:10.1158/0008-5472.CAN-10-4645)

275. Sokolova, V. & Epple, M. 2008 Inorganic nanoparticles as carriers of nucleic acids into cells. *Angew. Chemie - Int. Ed.* **47**, 1382–1395. (doi:10.1002/anie.200703039)

276. Shukla, R., Bansal, V., Chaudhary, M., Basu, A., Bhonde, R. R. & Sastry, M. 2005 Biocompatibility of gold nanoparticles and their endocytotic fate inside the cellular compartment: A microscopic overview. *Langmuir* **21**, 10644–10654. (doi:10.1021/la0513712)

277. Papasani, M. R., Wang, G. & Hill, R. A. 2012 Gold nanoparticles: The importance of physiological principles to devise strategies for targeted drug delivery. *Nanomedicine Nanotechnology, Biol. Med.* **8**, 804–814. (doi:10.1016/j.nano.2012.01.008)

278. Ghosh, R., Singh, L. C., Shohet, J. M. & Gunaratne, P. H. 2012 A gold nanoparticle platform for the delivery of functional microRNAs into cancer cells. *Biomaterials* **34**, 807–816. (doi:10.1016/j.biomaterials.2012.10.023)

279. Cheng, C. J., Tietjen, G. T., Saucier-Sawyer, J. K. & Saltzman, W. M. 2015 A holistic approach to targeting disease with polymeric nanoparticles. *Nat. Rev. Drug Discov.* **14**, 239–47. (doi:10.1038/nrd4503)

280. Grimm, D., Streetz, K. L., Jopling, C. L., Storm, T. A., Pandey, K., Davis, C. R., Marion, P., Salazar, F. & Kay, M. A. 2006 Fatality in mice due to oversaturation of cellular microRNA/short hairpin RNA pathways. *Nature* **441**, 537–541. (doi:nature04791 [pii]10.1038/nature04791 [doi])

281. Khan, A. a, Betel, D., Miller, M. L., Sander, C., Leslie, C. S. & Marks, D. S. 2009 Transfection of small RNAs globally perturbs gene regulation by endogenous microRNAs. *Nat. Biotechnol.* **27**, 549–55. (doi:10.1038/nbt.1543)

282. Murakami, Y. et al. 2011 The progression of liver fibrosis is related with overexpression of the miR-199 and 200 families. *PLoS One* **6**, 2–9. (doi:10.1371/journal.pone.0016081)

283. Deakin, N. O. & Turner, C. E. 2011 Distinct roles for paxillin and Hic-5 in regulating breast cancer cell morphology, invasion, and metastasis. *Mol. Biol. Cell* **22**, 327–341.

(doi:10.1091/mbc.E10-09-0790)

284. von Thun, A., Birtwistle, M., Kalna, G., Grindlay, J., Strachan, D., Kolch, W., von Kriegsheim, A. & Norman, J. C. 2012 ERK2 drives tumour cell migration in three-dimensional microenvironments by suppressing expression of Rab17 and liprin-β2. *J. Cell Sci.* **125**, 1465–1477. (doi:10.1242/jcs.092916)